EXPERIMENTAL AND THEORETICAL INVESTIGATION OF UNSTEADY SUPERCAVITATING HYDROFOILS OF FINITE SPAN

by

CHEN-WEN JIANG

and

PATRICK LEEHEY

Department of Ocean Engineering
Massachusetts Institute of Technology
Cambridge, Massachusetts 02139
Massachusetts Institute of Technology
Cambridge, Massachusetts 02139

EXPERIMENTAL AND THEORETICAL INVESTIGATION OF

UNSTEADY SUPERCAVITATING HYDROFOILS OF

FINITE SPAN

by

CHEN-WEN JIANG
and
PATRICK LEEHEY

Report No 83481-4

September 1977

Department of Ocean Engineering
Massachusetts Institute of Technology
Cambridge, Massachusetts 02139

EXPERIMENTAL AND THEORETICAL INVESTIGATION

OF UNSTEADY SUPERCAVITATING HYDROFOILS OF FINITE SPAN

by

Chen-Wen Jiang &
Patrick Leehey

ABSTRACT

Measurements of the forces, moment, and cavity pressure
on aspect ratio 3 and 5 supercavitating hydrofoils of
elliptical planform oscillating in pitch have been obtained
at frequencies from 5 to 20 Hz. A region of resonant
behavior was found, which corresponds to a natural frequency
of the cavity. A thermodynamic analysis of the cavity was
performed under the assumptions of a spherical cavity and
uniform cavity interior properties. The calculated damped
natural frequencies were compared with the results taken
from peak oscillatory lift experiments. The damping ratio
of the cavity depends upon the partial pressure of air,
temperature and cavity size. A numerical method was
developed for a supercavitating hydrofoil. Discrete
vortices and sources are used to formulate the equations.
The cavity length was iterated to get the desired cavitation
number over the cavitated planform. The numerical results
of an unsteady two-dimensional finite cavity were compared
with zero cavitation number theory. The problem of
supercavitating hydrofoils of finite span in steady flow
was solved numerically and compared with analytical solutions
and with experiments. Results of these calculations
indicate that this method gave a more accurate prediction of
lift and moment coefficients than existing asymptotic
theories. The numerical solutions of unsteady hydrofoils
of finite span were also compared with experiments. The
amplitude of the forces was in good agreement, but the
phase differences between theory and experiment was large.
The effect of cavity pressure variation should be investi-
gated further.

REPORT DOCUMENTATION PAGE	READ INSTRUCTIONS. BEFORE COMPLETING FORM

1. REPORT NUMBER 83481-4	2. GOVT ACCESSION NO.	3. RECIPIENT'S CATALOG NUMBER

4. TITLE (and Subtitle)	5. TYPE OF REPORT & PERIOD COVERED
Experimental and Theoretical Investigation of Unsteady Supercavitating Hydrofoils of Finite Span.	Final, October 1976 through September 1977
	6. PERFORMING ORG. REPORT NUMBER

7. AUTHOR(s)	8. CONTRACT OR GRANT NUMBER(s)
Chen-Wen Jiang Patrick Leehey	N00014-76-C-0358

9. PERFORMING ORGANIZATION NAME AND ADDRESS	10. PROGRAM ELEMENT, PROJECT, TASK AREA & WORK UNIT NUMBERS
Massachusetts Institute of Technology Cambridge, Massachusetts 02139	SR 009 01 01 no PE

11. CONTROLLING OFFICE NAME AND ADDRESS	12. REPORT DATE
David W. Taylor Naval Ship Research and Development Center Bethesda, Md 20084	Sept 77
	13. NUMBER OF PAGES 134 p.

14. MONITORING AGENCY NAME & ADDRESS(if different from Controlling Office)	15. SECURITY CLASS. (of this report)
	Unclassified
	15a. DECLASSIFICATION/DOWNGRADING SCHEDULE

16. DISTRIBUTION STATEMENT (of this Report)

Approved for public release; distribution unlimited

17. DISTRIBUTION STATEMENT (of the abstract entered in Block 20, if different from Report)

DDC
JAN 12 1978
RECEIVED
F

18. SUPPLEMENTARY NOTES
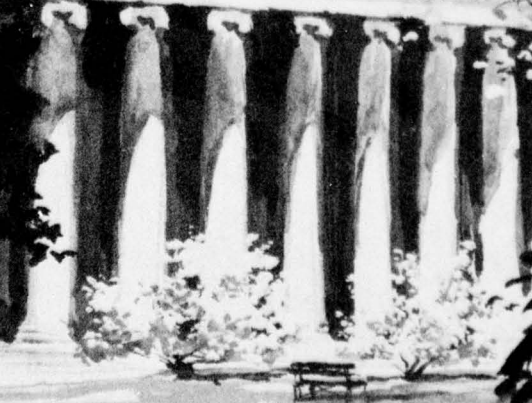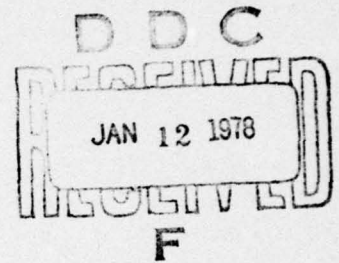
Prepared under Naval Sea Systems Command General Hydromechanics Research Program administered by the David W. Taylor Naval Ship Research and Development Center, Bethesda, Md 20084

19. KEY WORDS (Continue on reverse side if necessary and identify by block number)

Cavity Flow
Hydrofoils

20. ABSTRACT (Continue on reverse side if necessary and identify by block number)

Measurements of the forces, moment and cavity pressure on aspect ratio 3 and 5 supercavitating hydrofoils of elliptical planform oscillating in pitch have been obtained at frequencies from 5 to 20 Hz. A region of resonant behavior was found, which corresponds to a natural frequency of the cavity. A thermodynamic analysis of the cavity was performed under the assumptions of a spherical cavity and uniform cavity interior properties. The calculated

406856

20

damped natural frequencies were compared with the results taken from peak oscillatory lift experiments. The damping ratio of the cavity depends upon the partial pressure of air, temperature and cavity size. A numerical method was developed for a supercavitating hydrofoil. Discrete vortices and sources are used to formulate the equations. The cavity length was iterated to get the desired cavitation number over the cavitated planform. The numerical results of an unsteady two-dimensional finite cavity were compared with zero cavitation number theory. The problem of supercavitating hydrofoils of finite span in steady flow was solved numerically and compared with analytical solutions and with experiments. Results of these calculations indicate that this method gave a more accurate prediction of lift and moment coefficients than existing asymptotic theories. The numerical solutions of unsteady hydrofoils of finite span were also compared with experiments. The amplitude of the forces was in good agreement, but the phase differences between theory and experiment was large. The effect of cavity pressure variation should be investigated further.

ACKNOWLEDGEMENTS

-4-

TABLE OF CONTENTS

TABLE OF CONTENTS (CONTINUED)

LIST OF FIGURES

LIST OF FIGURES (CONTINUED)

LIST OF FIGURES (CONTINUED)

NOMENCLATURE

a	$\dot{a} = 1 + t^2$
$\mathbb{R}$	aspect ratio
$C_L, \Delta C_L$	lift and oscillatory lift coefficients, respectively
$C_D, \Delta C_D$	drag and oscillatory drag coefficients, respectively
$C_M, \Delta C_M$	moment and oscillatory moment coefficients, respectively
C_o	foil root chord
c	damping coefficient
C_v	specific heat at constant volume
D	thermal diffusivity of water
d	$d \equiv x - x_1 + tz_1 - tz$
F	applied force
g	y-coordinate of cavity foil combination
h	instantenous y-coordinate of the wetted surface
Δh	heaving amplitude
J	moment of inertia of the dynamometer system
k	stiffness of the dynamometer system; $k \equiv \omega C_o / U_\infty$
L	latent head; steady state cavity length at centroid of foil
$\bar{\ell}$	mean cavity length measured from foil leading edge at the mean chord
$\ell(z,t)$	cavity lengths
m	mass of the dynamometer system
M	applied moment

NOMENCLATURE (CONTINUED)

p_∞	upstream static pressure at the spanwise position of the foil centroid
p	static pressure
R	equivalent radius of the cavity
$\mathcal{R}$	universal gas constant
r	radius; distance
S	foil semispan
T	temperature
T_c	critical temperature of water
t	time
U_∞	free stream velocity
u,v,w	pertubation velocity along x,y,z direction
V	cavity volume; velocity
x	displacement of the dynamometer; T_c-T
$x,y,z,$	coordinate system
$x_\ell(z)$	chordwise coordinate of leading edge
ρ	density
σ	cavitation number
α	angle of attack; geometric angle
$\Delta\alpha$	pitching amplitude
β	geometric angle
ω	frequency of oscillation; natural frequency
ϕ	phase angle; geometric angle
ψ	angular displacement
λ	coefficient of thermal conductivity

NOMENCLATURE (CONTINUED)

φ velocity potential

γ, δ spanwise and chordwise vortex strength, respectively

q   source strength

ξ, ζ, η dummy variables in the x,y,z, directions

Subscripts

v   vapor

a   gas

o   mean properties

c   cavity

CHAPTER I INTRODUCTION

Considerable theoretical and experimental work has been done on three-dimensional supercavitating hydrofoils, but the agreement between the theory and experiments is not fully satisfactory.

Unsteady two-dimensional linearized theories for zero cavitation number have been developed by Parkin (1957) and Woods (1957). Leone (1968) developed a two dimensional unsteady theory based on the method of matched asymptotic expansions, and measured oscillating lift for two-dimensional supercavitating hydrofoils. A recent review of supercavitating flows around lifting hydrofoils if that of Hsu (1975). Leehey and Stellinger (1975) obtained theoretical predictions of steady state forces and moments for hydrofoils of finite span which compared well with experimental data. Widnall (1966), Tsen and Guilband (1973) and Unruh and Bass (1974) studied linearized three-dimensional cavitating hydrofoils using numerical lifting surface theory. The steady cavity length in these studies is assumed to be relatively long so that the variation of cavity length due to unsteady motion can be neglected in the analysis. Unsteady force characteristics were measured by Wetzel and Foerster (1967) for naturally ventilated foils undergoing either a sinusoidal heaving motion or a harmonic oscillation of a trailing edge flap. Klose and Acosta (1969) carried out unsteady force

measurements and flow observation on superventilated hydro-
foils in heaving motion. Their unsteady lift measurements
showed appreciable variation with changes in cavity length.

The present experimental work is concerned with non-
steady motion of cavitating hydrofoils under pitch oscilla-
tion. A region of resonant behavior near the reduced
frequency $\omega\bar{\ell}/U_\infty \simeq 2$ was found, where $\bar{\ell}$ is the mean cavity
length measured from the leading edge of the foil. For a
fixed oscillation frequency, the amplitude of the oscillating
lift coefficient peaks sharply at a critical cavity length
(or volume). Microphone measurements of cavity pressure
show that it is not constant during the pitch oscillation.

The resonance of the air-vapor cavity has been studied
asssuming incompressible flow, uniform cavity interior proper-
ties and a spherical cavity. The liquid phase inside the
cavity, viscosity and gas diffusion have been neglected in
this analysis. A damped natural frequency was found. The
oscillating amplitude depends on the damping ratio.

For long cavities, the oscillatory forces are away
from the region of resonant behavior. The unsteady forces
are compared with numerical results, obtained from a lifting
surface theory. The discrete vortexes and source method
is adopted to formulate the equations. An iteration scheme
is used to alter the cavity length until the desired cavitation

number is reached over the cavitated platform. The numerical amplitude of the oscillatory lift compares well with the experiment. However, the phase difference between theory and experiment cannot be neglected.

Numerical results for lift and moment coefficients on steady supercavitating hydrofoils are in good agreement with steady flow experiments of Leehey & Stellinger (1975) and Maixner (1977). The results show that the improvement has been made after considering the lifting surface effects.

CHAPTER II EXPERIMENTAL STUDY

2.1 Experimental Apparatus

A) Variable Pressure Water Tunnel

The experimental work was conducted in the Recirculating Variable Pressure Water Tunnel of the Department of Ocean Engineering, Massachusetts Institute of Technology. Test section velocity is variable between 0 and 30 feet per second, static pressure is variable between atmospheric pressure and 3 inch Hg. The test section is 20 inches by 20 inches and 4.5 feet long. In order to get high oscillating forces and small cavitation numbers, the tunnel velocity was run as high as practical ($\simeq$ 30 ft/sec). The velocity is indicated on a manometer which gives the differential static head between two locations in the contraction section. This reading was calibrated by using a pitot tube in the test section. Figure 2.1 presents an overall view of the working section. The dynamometer is mounted in the top window of the test section. For these tests, two force and one moment component were measured.

B) Models and Shafts

The foils used in this test were flat plate sections with elliptic plan forms, the same used by Leehey and Stellinger (1975), with dimensions as shown in Figure 2.2. Each foil and shaft were constructed of Type 304 stainless steel and joined together by two pins.

C) Dynamometer

The modified dynamometer was designed by Riva (1974) to permit measurements of forces and moments on hydrofoils oscillating in pitch. The pictures of this system are shown in Figures 2.1 and 2.3.

The shaft is supported horizontally and vertically by two Fafnir self-aligning bearings. These bearings are mounted in a cylindrical-spherical housing attached to the floating part of the dynamometer, which can be adjusted to correct misalignment of the foil relative to the top window.

The clamping and stopping system are constructed on the cylindrical-spherical bearing housing. The clamping system permits the use of the dynamometer in steady experiments while the second one prevents the foil from going to too large an attack angle in case of failure during unsteady tests.

The torque transducer was designed as an extension of the shaft. It was mounted on the top of the shaft and with set screws. The transducer is operated with two foil strain gages BLH-FAED-06-12-S6.

The oscillatory movement of the foil is produced by two arms set orthoganally on an imaginary horizontal plane, and articulated by Fafnir rod-ends.

To provide lift and drag measurements without interference of one with the other, the oscillatory arms can have

their positions changed, relative to the center line of the
tunnel, which is coincident with the center line of the
dynamometer.

D) Drive Syetem

The pitching apparatus consists of a crank arm which
is oscillated sinusoidally by means of an eccentric pin
arrangement driven by an electric motor. The motor speed
is controlled by a potentiometer.

A two level steel frame attached to the flange and
side window of the tunnel provides the necessary support
for the pulleys, eccentric wheel and motor. The eccentric
and two pulleys that drive the crank arm are mounted on the
upper level of this frame.

The pulleys have speed ratio 2 and 3 relative to the
motor. The motor is a Master DC motor with 1/2 HP Output
at 2000 RPM. The eccentric is designed to provide in the
following amplitudes of dynamic angle of attack of the foil:
1.5^O, 2.0^O, 2.5^O, 3.0^O, 3.5^O, and 4.0^O.

2.2 Hydrofoil Test Procedure

Dynamic calibration of the force gages were carried
out with the aspect ratio 5 foil. The dynamometer, installed
in the water tunnel, was subjected to a sinusoidally oscilla-
ting force, generated by the B & K shaker. The force signals
from the force gages and the shaker were analyzed with the
Spectral Dynamics Analyzer, a heterodyning filter with 5 Hz

bandwidth. The measurements covered the frequency range from 5 Hz up to 20 Hz. The force ratio and phase difference between the load cells and shaker show that the natural frequency of the dynamometer is above the test range. It is reasonable to represent the real system by the model with mass-spring-dashpot. Damping is small in this mechanical system so that the exact value is unimportant. Details of this calibration are shown in Appendix A.

A piezoelectric pressure transducer was mounted at the tunnel top window about 5" from midchord to measure the dynamic pressure inside the cavity. The diaphgram of the pressure transducer is at 1" below the root of the foil. An accelerometer was mounted on the crank arm at 7" from the foil shaft to count the frequency and to provide phase difference relative to force, moment and cavity pressure. Signals output of transducers were amplified and then analyzed by the Spectral Dynamics Analyzer. A general arrangement of the readout system is shown in Figure 2.4.

The dynamometer was aligned at the flow direction to read lift and drag directly. Geometrical angle of attack was set by aligning the flat side of each foil with a wedge which against the test section side wall. Amplitude of oscillation can be set by selecting the wheel eccentricity. Oscillation frequency was adjustable from 5 Hz to 20 Hz by changing the resistance in the field windings of the DC drive motor.

Static pressure in the test section was read from a mercury manometer connected to taps in the tunnel wall at the beginning and end of the test section, on the center line, and corrected for hydrostatic head to give static pressure at hydrofoil centroid. Static pressure in the cavity was read from a mercury manometer connected to a tap on the suction side of the foil. Test section static pressure was variable between 3" Hg and 9.5" Hg absolute pressure.

Measurements have been made for the forces and moments on aspect ratio 3 and 5 hydrofoils oscillating in pitch. Readings were taken of lift, drag, moment, static pressure, cavity pressure, frequency, oscillatory forces, phase differ-ence, water temperature and velocity. At each oscillation frequency, the static pressure of the test section was reduced in increments of 0.6" Hg in the supercavitating case. Cavity length was photographed and confirmed with Leehey & Stellinger (1975), and then the mean cavity length is taken and used as the parameter in the reduced frequency.

The cavitation number, σ_c, is defined as

$$\sigma_c \equiv \frac{P_\infty - P_c}{\frac{1}{2}\rho U_\infty^2}, \qquad (2-1)$$

where P_∞ is the pressure for upstream at the elevation of the foil centroid, P_c is the cavity pressure. The cavitation

number, σ_v , based on vapor pressure is defined as

$$\sigma_v \equiv \frac{P_\infty - P_v}{\frac{1}{2} \rho U_\infty^2} . \qquad (2-2)$$

The vapor pressure, P_v , was calculated as a function of
water temperature according to the formulae of Smith, Keyes
and Gerry (1934).

In this experiment, the cavity pressure is taken from
the pressure tap on the foil.

2.3 Experimantal Results & Discussions

The comparisons of measured lift and moment for unsteady
fully wetted flow with analytic solutions are shown in Figures
2.5 and 2.6. The foils used in the analytic solutions are
flat plates which differ from the foils we used in our test.
However, the agreement in both phase and amplitude is good
for lift. The torsional stiffness of the dynamometer was
changed when the tunnel pressure was reduced. In particular,
the stiffness of the rubber seal which clamps the shaft
depends upon the pressure difference between the atmosphere
and tunnel pressure. Therefore, the properties of the rubber
seal have been measured for different pressure differences
across it, permitting the data reduction to obtain the moment
coefficient based on the calibration of the torque transducer
under operational tunnel pressures.

Figures 2.7 and 2.8 present the oscillating lift force

and the phase difference between the force and displacement.
There is evidence of a cavity resonance at reduced frequency
$\omega \bar{l}/U_\infty \simeq 2$. Resonance frequency decreases as the cavity
length increases. For longer cavities, the effect of this
kind of resonance is weak, because the damping of cavity
oscillation is greater for long cavities. An analysis of
this phenomena appears in the following chapter. From the
observation of high-speed motion pictures it appears that
the cavity length changed a lot at the resonance frequency.
The variation of cavity length depends on the oscillating
frequency and flow velocity. The phase difference between
lift force and angular displacement tends to decrease as
the oscillation approaches the resonance.

Figures 2.9 through 2.12 show the moment coefficients, drag
coefficients and phase differences. The oscillatory coeffi-
cients depend on the cavity length. The peak variations
occur near the resonant frequency.

Measurements of cavity pressure show that the cavity
pressure is not constant during the pitch oscillation. The
amplitude of cavity pressure oscillation depends on the
cavity length and oscillation frequency, being greatest at
high frequencies and short cavity lengths. The relationship
between unsteady cavity pressure and oscillatory lift cieffi-
cient at two different reduced frequencies for each foil is

-22-

shown in Figures 2.13 and 2.14.   The oscillating cavity
pressure has been non-dimentionalized by the dynamic head
so that a direct comparison can be made with the oscillatory
lift coefficient.   Evidently the unsteady lift coefficient
is significantly affected by the oscillation in the cavity
pressure for short cavity lengths.

CHAPTER III ANALYSIS OF BUBBLE RESONANCE

As mentioned in Chapter II, there is evidence of a cavity resonance near the reduced frequency at 2. Determination of the natural frequency of the cavity flow system is very complicated matters. For incompressible flow, the complexity of the problem is greatly reduced by the assumptions of spherical symmetry and uniform cavity properties. The viscosity is neglected in the following discussion. Several cases of the bubble dynamics have been discussed by Hsieh (1965). Evaporation is an important process in cavity oscillation. The variation of cavity pressure in time can not be neglected as it is in the growth of small cavities. The thermodynamic effects are essential in the cavity oscillation. The simplified linear governing equations of the cavity oscillation about the mean quantities are

$$\frac{d\tilde{V}}{dr} + \frac{2\tilde{V}}{r} = 0 ,$$

$$\frac{d\tilde{V}}{dt} = -\frac{1}{\rho_{\circ}} \frac{d\tilde{P}}{dr} ,$$

$$\frac{d\tilde{T}}{dr} = \frac{\lambda}{\rho_{\circ}C_{v}} \left(\frac{d^{2}\tilde{T}}{dr^{2}} + \frac{2}{r} \frac{d\tilde{T}}{dr} \right). \qquad (3-1)$$

The interfacial boundary conditions (r = R) are

$$\tilde{T} = T',$$

$$\tilde{V} = \dot{R},$$

$$\tilde{p} = p',$$

(3-2)

and

$$\lambda \frac{d\tilde{T}}{dr} = \frac{L}{3}\left(R_o \frac{dp'}{dt} + 3p'_o \frac{dR}{dt}\right) + \frac{1}{3}p'_o R_o C'_v \frac{dT'}{dt} + p'_o \frac{dR}{dt}.$$

(3-3)

In the foregoing set of equations, V is velocity, p is pressure, T is temperature, p is density, C_v is specific heat at constant volume, λ is the coefficient of thermal conductivity. Primed symbols with subscript for perturbation quantities, and with subscript (o) for the equalibrium quantities within the cavity, curled symbol for perturbation quantities outside the bubble, subscript (o) for equilibrium values. In the last boundary condition equation we neglect the heat conduction through the liquid phase within the cavity.

When the cavity is undergoing harmonic oscillation, the solutions of Eq. (3-1) subject to the boundary condition Eq. (3-2) will be

$$\tilde{V} = \frac{\dot{R} R_o^2}{r^2},$$

$$\tilde{p} = \frac{j\omega p_o R_o^2 \dot{R}}{r},$$

(3-4)

$$\tilde{T} = T'\left(\frac{r}{R_o}\right)^{1/2} \frac{K_{1/2}\left(\sqrt{\frac{\omega}{D}}\, r\, e^{j\pi/4}\right)}{K_{1/2}\left(\sqrt{\frac{\omega}{D}}\, R_o\, e^{j\pi/4}\right)},$$

where K is the modified Bessel function and D ($\equiv \lambda / \rho_o C_v$) is the thermal diffusivity of water. The velocity and temperature gradient at the cavity boundary are

$$\dot{R} = - \frac{j P'}{\rho_o R_o \omega} \ ,$$

$$\frac{d\tilde{T}}{dr} = -T'(\frac{\omega}{D})^{1/2} e^{j\pi/4} \frac{K_{3/2}(\sqrt{\frac{\omega}{D}} R_o e^{j\pi/4})}{K_{1/2}(\sqrt{\frac{\omega}{D}} R_o e^{j\pi/4})} \ . \qquad (3-6)$$

Since D is a small number ($\simeq 1.6 \times 10^{-6} ft^2/sec$) the argument of the Bessel function is large. The temperature gradient is approximately

$$\frac{d\tilde{T}}{dr}\bigg|_{r=R_o} = -T'(\frac{\omega}{D})^{1/2} e^{j\pi/4} \ . \qquad (3-7)$$

Substituting (3-5), (3-7) into (3-3), we get the condition

$$-\frac{1}{\rho_o \omega R_o} (\rho'_o L + P'_o) P' + (\frac{1}{3} \rho_o R_o C'_v \omega - j\lambda (\frac{\omega}{D})^{1/2} e^{j\pi/4}) T'$$

$$+ \frac{L R_o \omega}{3} \rho' = 0 \ . \qquad (3-8)$$

If the gases within the cavity satisfy the ideal gas equation $P v = \mathcal{R} T$ and we neglect the diffusion of gases (i.e. $m_a = $ constant),

$$P_a = \rho_a \mathcal{R}_a T \ .$$

After a simple calculation, and using (3-5), one can get the variation of pressure P'_a

$$P'_a = \rho_a \mathcal{R}_a T' + \frac{3 P_{a_o}}{\rho_o R_o^2 \omega^2} P' \qquad (3-9)$$

We assume that the density of the vapor corresponds to its temperature at the given pressure according to the equation of state.

$$P_v = \rho_v R_v T$$

The variation of vapor pressure is

$$P_v' = \rho_v R_v T' + R_v T \rho_v'. \tag{3-10}$$

We assume the mass of gases inside the cavity is constant

$$\rho_a V = \text{Constant}.$$

From this equation and Eq. (3.5) we get

$$\rho_a' = \frac{3 \rho_{a_0}'}{\rho_o R_o^2 \omega^2} P',$$

then

$$\rho_v' = \rho' - \rho_a' = \rho' - \frac{3 \rho_{a_0}'}{\rho_o R_o^2 \omega^2} P'.$$

Substitute the last equation into Eq. (3-10)

$$P_v' = \rho_v R_v T' + R_v T \left(\rho' - \frac{3 \rho_{a_0}'}{\rho_o R_o^2 \omega^2} \right) P'.$$

The total variation of cavity pressure is the summation of the variation of partial pressures.

$$P' = P_v' + P_a',$$

or

$$\left(\frac{1}{P_o'} - \frac{3\rho_{ao}'}{P_o'\rho_o R_o^2 \omega^2} + \frac{3\rho_{ao}' R_v T}{\rho_o R_o^2 \omega^2 P_o'}\right) p'$$

$$- \frac{1}{T_o'}T' - \frac{R_v}{\rho_o' R} \rho' = 0, \qquad (3\text{-}11)$$

where

$$P_o' \equiv \rho_o' R T,$$

$$\rho_o' R \equiv \rho_{v_o}' R_v + \rho_{ao}' R_a.$$

The vapor within the cavity is not a superheated vapor. A relationship between vapor pressure and temperature was taken from the paper by Smith, Keyes and Gerry (1934)

$$\log_{10} \frac{P_c}{P_v} = \frac{x}{T}\left[\frac{a' + b'x + c'x^3}{1 + d'x}\right],$$

where

$$x = T_c - T,$$

P_v = vapor pressure in int. atm.,

$P_c = 218.167$ int. atm.,

$T = t°F + 255.38,$

$T_c = 647.27,$

$a' = 3.2437814,$

$b' = 5.868 \times 10^{-3},$

$c' = 1.1702379 \times 10^{-8},$

$d = 2.1878462 \times 10^{-3}.$

We can get the equation of variation of pressure and temperature by taking the derivative of pressure with respect to temperature

$$P_v' - C_1(P_v, T)T' = 0,$$ (3-12)

where

$$C_1 = \left(\frac{9}{5}\ln 10\right) P_v \left\{ \frac{a' + 2b'x + 4c'x^3}{T_c + (d'T_c - 1)x - x^2} - \frac{(a'x + b'x^2 + c'x^4)(d'T_c - 1 - 2x)}{[T_c + (d'T_c - 1)x - x^2]^2} \right\}.$$

Combine Eqs. (3-9) and (3-12)

$$\left(1 - \frac{3P_{ao}'}{P_o R_o^2 \omega^2}\right) P' - (P_{ao}' R_a + C_1) T' = 0.$$ (3-13)

Equations (3-8), (3-11) and (3-13) constitute the eigenvalue problem. The natural frequency of the system is determined by

$$\begin{vmatrix} -\frac{1}{P_o \omega R_o}(P_o'L + P_o') & \frac{1}{3}P_o R_o C_v'\omega - j\lambda\left(\frac{\omega}{D}\right)^{\frac{1}{2}}e^{j\frac{\pi}{4}} & \frac{\angle R_o \omega}{3} \\ \left(\frac{1}{P_o'} - \frac{3P_{ao}'}{P_o'P_o R_o^2\omega^2} - \frac{3P_{ao}'R_v T}{P_o R_o^2\omega^2 P_o'}\right) & -\frac{1}{T_o'} & -\frac{R_v}{R}\frac{1}{P_o'} \\ \left(1 - \frac{3P_{ao}'}{P_o R_o^2\omega^2}\right) & -(P_{ao}'R_a + C_1) & 0 \end{vmatrix}$$

$$= 0,$$

or

$$A\omega^2 - B = j e^{j\pi/4} G \left(\frac{H}{\omega^2} - 1 \right) \omega^{3/2}, \qquad (3\text{-}14)$$

where

$$A = \frac{L R_o C}{3 P_o'} - \frac{R_v}{R} \frac{R_o C_v'}{3} - \frac{L R_o}{3 T_o'},$$

$$B = \frac{L C (P_{ao}' - P_{ao}' R_v T)}{P_o' P_o R_o} + \frac{R_v}{R} \frac{P_{ao} C_v'}{P_o R_o}$$

$$+ \frac{R_v C}{R P_o'} \frac{P_o' L + P_o'}{P_o R_o} - \frac{L P_{ao}}{T_o' P_o R_o},$$

$$G = \frac{P_o}{P_o'} D^{1/2} C_v,$$

$$H = \frac{3 P_{ao}'}{P_o R_o^2},$$

$$C = P_{ao}' R_a + C_1.$$

The typical natural frequencies for a given T, P_{ao}', R_o, are shown in Figure 3.1. We assume the gases in the cavity are air. A damped natural frequency was found. At a fixed P_{ao}', the natural frequency decreases when the cavity volume increases. The air content not only increases the natural frequency but also reduces the damping ratio. For the damped, single-degree of freedom case, the ratio of damping to critical damping is equal to the ratio of ω_i to ω_n, where ω_i is the imaginary part of natural frequency, and ω_n is the undamped natural frequency. The ratio of ω_i to ω_n will give some idea of the damping for different cavities as shown

in Figure 3.2. This analysis will not only tell us the
natural frequency but will explain the qualitativety oscil-
lating amplitude of lift coefficient shown in Figures 2.7
and 2.8. The cavity pressure is always higher than the
vapor pressure. This result is to be expected as the gases
from the water contribute to the pressure within the cavity.
The discrepancy between cavity pressure and vapor pressure
decreases with decreasing cavitation number. Experimental
results of cavity pressure measurement are shown in figure
4.10. Further discussions appear in the next chapter.
Since the short cavaties have a higher partial pressure due
to non-water-vapor gases, damping ratio (damping/critical
damping) is small in short cavities. The stiffness of cavity
increases with increasing air pressure inside the cavity, so
we expect that they have higher natural frequencies and less
damping ratio. However, the reason for shorter cavities having a
higher gas content is not clear.

The cavity volumes are calculated from the numerical
lifting surface method. Under the assumption of spherical
volume and neglecting the surface tension effect, the
natural frequency of the cavity calculated from Equation (3-14),
and the resonance frequency under test are shown in Figure
(3.2). In the present experiment, only a few points can be
plotted in the graph. The "loop" trajectories in Klose &
Acosta (1969) seems also associated with the natural frequency
of the cavity.

CHAPTER IV NUMERICAL ANALYSIS

4.1 Linearized Theory for Three-Dimensional Supercavitating Hydrofoils

The linearized problem for a cavitating hydrofoil of finite span in unsteady flow can be represented by a set of coupled integral equations. The derivation proceeds either from Green's theorem or from the solution for the velocity field induced by a distribution of vortices and sources. This distribution must be chosen to satisfy the relevant boundary conditions. The numerical model we are about to describe is shown in Figure 4.1

The source distribution, q $(x,z,t$), represents the slope difference between the upper cavity surface and the mean camber line of the foil or the lower cavity surface at the point (x,o,z). The vortex distributions (γ (x,z,t), $\delta(x,z,t$)) create the perturbation velocity differences in the x and z components between the upper and lower surfaces at the point (x,o,z). This leads to the result

$$q(x,\mathfrak{z},t) \equiv \frac{1}{U_\infty} \left(\mathcal{V}(x,+0,\mathfrak{z},t) - \mathcal{V}(x,-0,\mathfrak{z},t) \right),$$

$$\gamma(x,\mathfrak{z},t) = \frac{1}{U_\infty} \left(u(x,-0,\mathfrak{z},t) - u(x,+0,\mathfrak{z},t) \right), \qquad (4-1)$$

$$\delta(x,\mathfrak{z},t) \equiv \frac{1}{U_\infty} \left(w(x,+0,\mathfrak{z},t) - w(x,-0,\mathfrak{z},t) \right).$$

The boundary conditions specified are the normal velocity on the wetted surface of the foil, a constant pressure in the cavity, and closure of the cavity.

$$V(x, -0, z) = \frac{\partial}{\partial t} h(x, z, t) + U_0 \frac{\partial}{\partial x} h(x, z, t),$$

$$P_c = P(x, +0, z, t),$$ (4-2)

$$0 = \iint\limits_{S_c} g(\xi, \varsigma, t) d\xi d\varsigma,$$

where h(x,z,t) is the instantaneous y-ordinate of the wetted surface. S_c is the surface of the cavity as projected onto the x-z plane. σ is the cavitation number. P_∞ and P_c are free-stream pressure and cavity pressure, respectively. Geurst (1961) proved that for two-dimensional steady flow, the re-entrant jet and Riabouchinsky models for cavity term-ination reduce upon linearization to a statement that the cavity is closed at its end. The requirement that the source strength be zero beyond the cavity trailing edge and the sum of sources is zero are necessary to meet this condition.

Based on the boundary conditions, the integral equations for three-dimensional unsteady flow can be written as (The details of this derivation are shown in Appendix B)

$$\mathcal{V}(x,-0,z,t) = -\frac{1}{2}\gamma(x,z,t)$$

$$+\frac{1}{4\pi}\iint_{S_a} \frac{\gamma_a(\xi,\varsigma,t)[x-\xi] + \delta_a(\xi,\varsigma,t)[z-\varsigma]}{\left[(x-\xi)^2 + (z-\varsigma)^2\right]^{3/2}} d\xi d\varsigma$$

$$+\frac{1}{4\pi}\iint_{S_w} \frac{\gamma_w(\xi,\varsigma,t)[x-\xi] + \delta_w(\xi,\varsigma,t)[z-\varsigma]}{\left[(x-\xi)^2 + (z-\varsigma)^2\right]^{3/2}} d\xi d\varsigma, \quad (4\text{-}3)$$

$$O = -\gamma_a(x,z,t) - \frac{1}{U_\infty}\frac{\partial}{\partial t}\int_{-\infty}^{x}\gamma_a(\xi,z,t)d\xi$$

$$+\frac{1}{2\pi}\iint_{S_c}\left\{-\frac{1}{U_\infty}\frac{\partial}{\partial t}\gamma(\xi,\varsigma,t)\frac{1}{\left[(x-\xi)^2+(z-\varsigma)^2\right]^{3/2}}\right.$$

$$\left.+\frac{(x-\xi)\gamma(\xi,\varsigma,t)}{\left[(x-\xi)^2+(z-\varsigma)^2\right]^{3/2}}\right\}d\xi d\varsigma, \quad (4\text{-}4)$$

$$0 = \iint_{S_c}\gamma(\xi,\varsigma,t)d\xi d\varsigma, \quad (4\text{-}5)$$

where S_a is the projection of the foil surface on to the x-z
plane and S_w is the projection of the wake region on to the
same plane. Note that the projected cavity area, S_c, is
also time dependent. The unknowns are the source strength,
vortex strength and cavity surface location.

For steady flow at a given cavitation number, this set
of equations simplifies to

$$\mathcal{V}(x,-0,z) = -\frac{1}{2}\gamma(x,z)$$

$$+\frac{1}{4\pi}\iint_{S_a}\frac{\gamma_a(\xi,\varsigma)[x-\xi]+\delta_a(\xi,\varsigma)[z-\varsigma]}{\left[(x-\xi)^2+(z-\varsigma)^2\right]^{3/2}}d\xi d\varsigma$$

$$+\frac{1}{4\pi}\iint_{S_w}\frac{\delta_w(\xi,\varsigma)[z-\varsigma]}{\left[(x-\xi)^2+(z-\varsigma)^2\right]^{3/2}}d\xi d\varsigma, \quad (4\text{-}6)$$

$$O = -\gamma_a(x,\partial)$$

$$+ \frac{1}{2\pi} \iint\limits_{S_c} \frac{(x-\xi)\, g(\xi,\vartheta)}{\left[(x-\xi)^2 + (\partial - S^2)\right]^{3/2}} \, d\xi \, d\vartheta, \tag{4-7}$$

$$O = \iint\limits_{S_c} g(\xi,\vartheta)\, d\xi \, d\vartheta. \tag{4-8}$$

The solution of these integral equations will represent the linearized, supercavatating hydrofoil of finite span in steady flow. The forces and moments can be calculated using the Bernoulli equation.

4.2 Linearized Theory for Two-Dimensional Supercavatating Hydrofoils

In the two-dimensional theoretical model, with an incompressible fluid, infinite pressures are necessary at $\Gamma \to \infty$ to generate a volume change in the cavity. However, Benjamin (1964) pointed out that any real flow is necessarily three-dimensional 'in the large'; thus the pressure singularity is an artifact of the two-dimensional case. Based on his discussion, the changing cavity volume of two-dimensional foil is introduced by the three-dimensional outer solutions. The overall solution can be obtained by matching the inner and outer solutions. Theoretically, the two-dimensional unsteady cavity can be treated as the inner solution of the three dimensional case. This inner solution does not match the boundary condition at infinity. The numerical method

for unsteady flow appears in this section only for the inner flow field.

The development of this problem proceeds from the velocity or pressure field induced by a two-dimensional distribution of vortices and sources. This velocity or pressure field will satisfy the boundary conditions which require a given normal velocity on the wetted surface, constant cavity pressure and closure of the cavity.

The derivation of these integral equations is the same as for three-dimensional cavity flow, except two-dimensional sources and vortices are used. The potential due to two-dimensional source distributed over the cavity region is

$$\varphi_s(x, y, t) = \frac{1}{4\pi} \int_0^\ell g(\xi, t) \ln\left[(x-\xi)^2 + y^2\right] d\xi. \qquad (4-9)$$

The two-dimensional vortex potential will be

$$\varphi_v(x, y, t) = \frac{1}{2\pi} \int_0^a \gamma_a(\xi, t) \tan^{-1}\left(\frac{y}{x-\xi}\right) d\xi. \qquad (4-10)$$

The integral equations which satisfy the boundary conditions are converted to

$$U(x, -0, t) = -\frac{1}{2} g(x, t) + \frac{1}{2\pi} \int_0^\ell \frac{\gamma_a(\xi, t)}{x-\xi} d\xi$$
$$+ \frac{1}{2\pi} \int_\ell^0 \frac{\gamma_w(\xi, t)}{x-\xi} d\xi, \qquad (4-11)$$

$$0 = -\gamma_a(x,t) - \frac{\partial}{\partial t}\int_0^x \gamma_a(\xi,t)\,dt + \frac{1}{\pi}\int_0^{\ell(t)}\frac{q(\xi,t)}{x-\xi}\,d\xi$$

$$+ \frac{1}{\pi}\frac{\partial}{\partial t}\int_0^{\ell(t)} q(\xi,t)\cdot\ln|x-\xi|\,d\xi, \tag{4-12}$$

$$0 = \int_0^{\ell(t)} q(\xi,t)\,d\xi. \tag{4-13}$$

These equations are sufficient to obtain the cavity length, the source distribution and the vortex distribution.

4.3 Numerical Method

The solution of the problem is obtained by reducing the coupled integral equations to a set of simultaneous algebraic equations. Since the method used in two-dimensional flow and three-dimensional steady flow is a simplification of the three-dimensional unsteady problem, the approach for the latter case will be discussed here.

The surface is divided into small elements. The element used in this model is one obtained by dividing the foil and cavity semispan into strips with cosine spacing, while the chord is divided into strips of constant spacing on the foil and on the cavity behind the foil. In order to increase the rate of convergence for the number of elements used, the first two elements of each chordwise strip, near the leading edge, have only one-half the chord spacing of the rest of

the elements on the foil.

The model uses discrete vortices and sources to represent the foil and cavity. Each element contains a bound line vortex, a trailing vortex and a line source. The quarter-chord line of each element contains the bound vortex, and the induced velocities are calculated for all elements at their midspan, three-quarter chord positions. James (1972) showed that for the best efficiency the vortex and control points should be arranged according to the Pistolesi approximation, i.e., at the quarter and three-quarter chord points on each element. The concentrated line source is taken to be a constant distribution across each element at its three-quarter chord position. Since the source distribution is singular at the cavity leading edge and termination point, these control points should be placed away from the singularities. Therefore, the first control point is located at the three-quarter chord and the source is located at the quarter chord. The local vortex or source strength divided by the element width.

Since the cavity length is unknown, the global closure condition is not used in the calculation. If it is, the variation of cavity length along the span cannot be iterated. This difficulty is overcome by applying the closure condition to individual spanwise strips. This approximation is exact for a symmetric foil. The source integration along a strip between $z = -\zeta$ and $z = \zeta$ is

the elements on the foil.

The model uses discrete vortices and sources to represent the foil and cavity. Each element contains a bound line vortex, a trailing vortex and a line source. The quarter-chord line of each element contains the bound vortex, and the induced velocities are calculated for all elements at their midspan, three-quarter chord positions. James (1972) showed that for the best efficiency the vortex and control points should be arranged according to the Pistolesi approximation, i.e., at the quarter and three-quarter chord points on each element. The concentrated line source is taken to be a constant distribution across each element at its three-quarter chord position. Since the source distribution is singular at the cavity leading edge and termination point, these control points should be placed away from the singularities. Therefore, the first control point is located at the three-quarter chord and the source is located at the quarter chord. The local vortex or source strength is given by the discrete vortex or source strength divided by the element width.

Since the cavity length is unknown, a closure condition is applied to individual spanwise strips in the calculation. Otherwise, the iteration technique does not converge. This condition satisfies the overall global condition. It also allows the variation of cavity length along the span to vary. This method is exact for a symmetric foil. The source integration along a strip between $z = -z_1$ and $z = z_1$ is

$$\int_{-\mathit{S}}^{\mathit{S}}\int_{\chi_{\ell}(\mathit{S})}^{\ell(\mathit{S},t)} \mathit{f}(\xi,\mathit{S},t)\, d\xi d\mathit{S}, \tag{4-14}$$

where $\chi_{\ell}(\zeta)$ and $\ell(\zeta,t)$ are the spanwise profiles of the leading edge and cavity termination points, respectively. Let $g_{\pm}(x,z,t)$ represent the profile of the cavity-foil combination. Then the stripwise integration becomes

$$\int_{-\mathit{S}}^{\mathit{S}}\int_{\chi_{\ell}(\mathit{S})}^{\ell(\mathit{S},t)} \left(\frac{\partial g_{+}}{\partial \xi} + \frac{\partial g_{+}}{\partial \mathit{S}} - \frac{\partial g_{-}}{\partial \xi} - \frac{\partial g_{-}}{\partial \mathit{S}}\right) d\xi d\mathit{S}$$

$$= \int_{-\mathit{S}}^{\mathit{S}} \left.(g_{+}(\mathit{S},\mathit{S}) - g_{-}(\xi,\mathit{S}))\right|_{\chi_{\ell}(\mathit{S})}^{\ell(\mathit{S},t)} d\mathit{S} + \int_{\chi_{\ell}(0)}^{\ell(0,t)} \left.(g_{+}(\xi,\mathit{S}) - g_{-}(\xi,\mathit{S}))\right|_{-\mathit{S}(\xi)}^{\mathit{S}(\xi)} d\xi$$

$$= 0. \tag{4-15}$$

The first integral is zero if the cavity is closed both at its leading edge and trailing edge. The second integral is zero due to the symmetry of the cavity. This integral therefore represents the stripwise closure condition.

The effect of all singularities must be calculated at each control points (Appendices C and D). The Biot-Savart's law is used to calculate the induced velocity at a control point due to a constant strength discrete vortex segment. The Kirchhoff's law and Kelvin's theorem must be satisfied for the vortex distribution. Consider the vortex segment

(x_1, o, z_1) to (x_2, o, z_2) with strength γ per unit length. Defining (ξ, ζ) as the coordinates of a general point on the vortex, and (x, z) as the coordinates of a control point, the induced velocity at (x, z) due to the bound vorticity, γ_a, is

$$\frac{4\pi \upsilon(x,0,\xi,t)}{\gamma_a} = \frac{a^{1/2}}{d}(\cos\beta + \cos\alpha), \qquad (4\text{-}16)$$

where

$$a \equiv 1 + t^2,$$

$$t \equiv (x_2 - x_1)/(\xi_2 - \xi_1),$$

$$d \equiv x - x_1 + t\xi_1 - t\xi,$$

$$\alpha \equiv Arg\left((x,0,\xi)-(x_1,0,\xi_1),\ (x_1,0,\xi_1)-(x_2,0,\xi_2)\right),$$

$$\beta \equiv Arg\left((x,0,\xi)-(x_2,0,\xi_2),\ (x_1,0,\xi_1)-(x_2,0,\xi_2)\right).$$

$$(4\text{-}17)$$

The induced velocity due to the trailing vortex (x, o, z_1) to (x_3, o, z_3) with strength δ_a is

$$\frac{4\pi \upsilon(x,0,\xi,t)}{\delta_a} = \frac{x-\xi}{\xi-\xi_1}\ \frac{1}{\left[(x-\xi)^2 + (\xi-\xi_1)^2\right]^{1/2}}\Bigg|_{\xi=x_1}^{\xi=x_3} \qquad (4\text{-}18)$$

The total velocity induced by a vortex distribution is the sum of the influence of all the spanwise and chord-wise vortices.

According to the Bernoulli equation, the pressure induced by the source component contains two terms: the space derivative and the time derivative.

$$P_s = -2 \left(\frac{\partial \varphi_s}{\partial x} + \frac{1}{U_\infty} \frac{\partial \varphi_s}{\partial t} \right). \tag{4-19}$$

The P_s due to the line source $((x_1, o, z_1) - (x_2, o, z_2))$ can be calculated by line integration

$$P_s = \frac{1}{2\pi} \int \left\{ \frac{1}{U_\infty} \frac{\partial}{\partial t} g(\xi, \varsigma, t) \frac{1}{[(x-\xi)^2 + (\varsigma-\varsigma)^2]^{1/2}} \right.$$

$$\left. - \frac{(x-\xi) g(\xi, \varsigma, t)}{[(x-\xi)^2 + (\varsigma-\varsigma)^2]^{3/2}} \right\} d\xi d\varsigma$$

$$= \frac{1}{2\pi U_\infty} \frac{\partial}{\partial t} g(\varsigma, \varsigma, t) \ln \frac{\tan(\frac{\pi}{4} + \phi_2)}{\tan(\frac{\pi}{4} + \phi_1)}$$

$$- \frac{1}{2\pi d} g(\xi, \varsigma, t) \left[(\cos\beta + \cos\alpha) \pm t (\sin\beta - \sin\alpha) \right], \tag{4-20}$$

$$\begin{array}{l} + \text{ for } d > 0 \\ - \text{ for } d < 0. \end{array}$$

where a, d, t, γ, and β are defined the same as in Eq. (4-17). ϕ_1, and ϕ_2 are the angles shown in Figure 4.2.

Equations (4-16) and (4-20) are not suitable for numerical computation if $d/\sqrt{a}$ becomes small. Approximate formulas are used for this special case.

An iteration is used to alter the cavity length until the desired cavitation number is reached over the cavitated planform. The steady flow solution is determined first, then the unsteady problem is solved by a step-by-step

procedure. Since the variation of the cavity length is unknown, the use of the frequency domain is not suitable. At each time step, a cavity length is assumed and the matrix coefficients are calculated. Solving the matrix with appropiate boundary conditions, we can get the distribution of vortices and sources, and the cavitation number on each strip. Then a new cavity length is chosen using the calculated cavitation number. The length is initially adjusted by one percent of the steady state cavity length. Then either extrapolation or Muller's iteration scheme (Kristiansen 1963) is used to calculate cavity length.

The linear algebraic equations which satisfy the boundary conditions are solved by using Gaussin elimination with equilibration and partial pivoting (e.g. Isaacson and Keller (1966)). The convergence test, both in space and time, has been made. Table 4.1 gives the number of elements chosen in the numerical calculation.

4.4 Comparison Between Theory and Experiment

Present numerical results for two-dimensional super-cavitating flow are compared with Geurst's analytic solution (1960) and Golden's numerical scheme (1975). Golden used a uniform distribution of the singularity in each element and the best choice of control points. Figure 4.3 simply confirms that these methods of solution lead to identical results.

The lift and moment calculation for supercavitating hydrofoils of elliptic planform was performed and compared with analytic solutions by Leehey (1973), experiments by Leehey and Stellinger (1975) and experiments by Maixner (1977). Leehey utilized the method of matched asymptotic-expansions. The theory is valid to first order in angle of attack and second order in the reciprocal of aspect ratio. The experiments of Leehey and Stellinger measured forces, moments and cavity length for aspect ratio 3 and 5 super-cavitating hydrofoils of elliptic planform. Maixner investigated the water tunnel wall effects on supercavitating hydrofoils of finite span by using a geometrically similar family of three hydrofoils (AR = 5). He showed that the previous tests by Leehey and Stellinger were reliable. The standard wind tunnel wall correction is adequate when the foil span is equal to or less than half of the tunnel depth. It should be noted that the data of Leehey and Stellinger was based on the cavitation number calculated by using the vapor pressure rather than the measured cavity pressure. In the comparison with present results, for the aspect ratio 5 foil, experimental data for the medium foil is taken from Maixner's results where measured cavity pressure were used.

Figures 4.4 and 4.5 show the lift coefficient, C_L/α. versus σ/α for the aspect ratio 5 and 3 hydrofoils, respectively. The agreement between theory and experiment is good.

For small values of σ/α, there is much better agreement with the present numerical theory than with Leehey's asymptotic theory. The foil and cavity combination is no longer of large aspect ratio at small σ/α , so the asymptotic theory is not valid.

The moment coefficient is taken about the mid-chord, consistent with the right hand rule. Figures 4.6 and 4.7 show the moment coefficient for the aspect ratio 5 and 3 hydrofoils. Since Leehey's matched asymptotic expansion theory neglects the lifting surface effect, it is expected that the present numerical lifting surface theory would show better agreement with experiments.

The nondimensional cavity length versus the ratio of cavitation number to angle of attack is shown in Figures 4.8 and 4.9. The cavity length is measured from the leading edge at the spanwise location of the centroid of the foil area. Generally speaking, the agreement between the theory and experiments is very good.

In Maixner's experiment, the cavity pressure was measured with a foil surface pressure tap. A noticeable "hook" was found in the lift and moment data at higher angles of attack (Figures 4.4 & 4.6). Ram effects on the cavity pressure measurement, due to the dynamic pressure, were further investigated on the large foil used in Maixner's test. The cavity pressure readings are taken both inside the cavity, using a total-head tube, and on the foil surface. The

L-shaped total head tube protuded downwards into the cavity from the upper tunnel wall so that it was parallel to the foil surface and pointed towards the leading edge, away from the impinging re-entrant jet. Figure 4.10 shows that the readings from the foil surface pressure tap are consistently higher than the measured cavity pressure, especially at higher angles of attack and shorter cavity lengths. If the correct cavity pressure readings were taken in the experiments of Maixner, the discrepancy from theory at higher angles of attack and shorter cavities would probably have been smaller.

The numerical results for an unsteady two-dimensional hydrofoil with a finite cavity are shown in Figures 4.11 to 4.14. Lift and moment coefficients in heave and pitch about the leading edge are compared with the results predicted by Woods (1957). The cavitation number was zero in Wood's calculation. At zero cavitation number, the cavity length change was neglected, as was the cavity volume. However, present two-dimensional solutions are the inner solution of the three-dimensional case. The following definitions are used for the unsteady force coefficients.

$$C_{L_{hr}} + j\, C_{L_{hi}} = \frac{\text{Lift due to heave about LE}}{\frac{1}{2}\rho U_\infty^2 C\, j\, \frac{k}{2}\, \Delta h}\ ,$$

$$C_{L\alpha r} + j C_{L\alpha i} = \frac{\text{Lift due to pitch about LE}}{\frac{1}{2}\rho U_\infty^2 C \alpha},$$

$$C_{Mhr} + j C_{Mhi} = \frac{\text{Moment about LE due to heave}}{\frac{1}{2}\rho U_\infty^2 C^2 j \frac{k}{2} \Delta h},$$

$$C_{M\alpha r} + j C_{M\alpha i} = \frac{\text{Moment about LE due to pitch}}{\frac{1}{2}\rho U_\infty^2 C^2 \alpha}.$$

The phase angles are defined as the arc tangent of the imaginary part to the real part in the last equations.

The effect of finite cavities tends to reduce the amplitude of the oscillating force and moment coefficients. The diversity of phase angles between finite cavity and infinite cavity increases with decreasing reduced frequency $(\omega C/U_\infty)$. One can expect this happens due to the variation of cavity length, it increases as reduced frequency decreases.

At large cavity lengths (low cavitation numbers), the oscillating lift force was away from the region of resonant behavior. Experimental data and theoretical values are compared with present numerical results in Figures 4.15-4.18. The theoretical values for cavitating flow over rectangular foils of aspect ratio 1 and 6 were taken from Widnall (1966), by forming a linear comvination of heave and pitch about the leading edge, resulting in pure pitch about

the midchord. The maximum chord of the semi-eliptic foil was taken as the chord of the rectangular foil. The moment coefficient was based upon planform area and mean chord. Figures 4.15 and 4.16 show the lift coefficient versus reduced frequency $(\omega C_o/U_\bullet)$ for the aspect ratio 5 and 3 hydrofoils, respectively. The same conditions as in experiments were used in the calculations. The agreement between numerical values and experimental results is good for lift amplitude. However, the phase angle predicted by theory is consistently higher than experiment. This may be in part due to the variation of cavity pressure, which is sensitive to the phase angle. Although the cavity pressure variations were small at long cavities, the cavity length is very sensitive to the cavitation number (Figures 4.8 and 4.9). However, the explanation of phase angle discrepancy is not fully satisfactory at this moment. The difference of unsteady lift measurements between these two hydrofoils is negligible. The finite span effect is not noticable for the frequency range of the tests. Figures 4.17 and 4.18 show the oscillatory moment coefficient. for the aspect ratio 5 and 3 hydrofoils. At high reduced frequencies, the present theory predicts larger moment coefficients that found by experiment. The difference of phase angles between theory and experiment is large. One possible reason is that the oscillatory moment of supervacitating flow is a small quantity, which has the same order of magnitude as the moment produced by the inertia force and spring force in the mechanical system. The torsional system of the dynamo-

meter used in measuring the moments was not calibrated at
the conditions that the unsteady measurements were made. The
comparison between the present numerical method for a rectang-
ular hydrofoil and Widnall's results is shown in Appendix E.

Present numerical calculation also gives the variation
of cavity length and cavity volume. Figures 4.19 and 4.20
ahow these two variations decrease with reduced frequency
increases. The amplitude of the oscillatory cavity volume is
about 40% of the mean cavity volume when $\Delta\alpha/\alpha$ = .167. If the
variations of cavity pressure were considered, the phase lag
should enlarge due to the heat transfer process.

Chapter V.   CONCLUSIONS AND RECOMMENDATIONS

Measurements were made of forces and moments for aspect ratio 3 and 5 supercavitating hydrofoils of elliptical planform oscillating in pitch. For short cavities, the natural frequency of the cavity plays an important role in the oscillating forces. A pressure transducer was used to measure the variation of cavity pressure. It showed that the cavity pressure is not constant during the pitch oscillation. The amplitude of cavity pressure oscillation depends on the cavity length and oscillation frequency.

The thermodynamic analysis of the cavity was performed by assuming spherical symmetry and uniform cavity interior properties. Eigenvalues were calculated subject to the given boundary conditions. The natural frequency decreases when the cavity volume increases, which confirmed the experimental results. The stiffness of the cavity results from the air content inside the cavity. The calculated ratio of imaginary part of the natural frequency to the undamped natural frequency indicated that more air content decreases the damping ratio. The temperature gradient inside the cavity was neglected in the analysis. The model used only describes general features of the process. The entire unsteady analysis must be redone to account for cavity pressure variations.

The discrete vortex and source method is developed for

supercavitating hydrofoils. The cavity length was iterated
to get a uniform cavitation number over the cavity planform.
The numerical results for an unsteady two-dimensional
hydrofoil with a finite cavity were compared with the
theoretical results at zero cavitation number. The
appreciable difference of phase angles between non-zero
and zero cavitation numbers was found. The lift and
moment calculations for supercavitating hydrofoils of
elliptic planform in steady flow was performed and compared
well with previous experiments. A more accurate prediction
of lift and moment coefficients was obtained by the present
numerical method than with existing asymptotic theories.
For long cavities the numerical results of three-dimensional
unsteady flow were compared with experiment. Amplitude
of oscillatory forces compared well between theory and
experiment. However, noticeable difference of phase
angles was found. Since the cavity pressure was considered
as a constant during unsteady motion, one should find the
importance of cavity pressure variation.

REFERENCES

Benjamin, T. B. 1964 Note on the interpretation of two-dimensional theories of growing cavaties. J. fluid Mech. 19, 137.

Geurst, J. A. 1960 Linearized theory for fully cavitated hydrofoils. Int. Shipbuilding Progress, vol 7, No. 65·

Geurst, J. A. 1961 Linearized theory of two-dimensional cavity flows. Doctoral Dissertation, Technical Univ., Delft, The Netherlands.

Golden, D. W. 1975 A numerical method for two-dimensional, cavitating, lifting flows. M. S. Thesis, MIT.

Hsieh, D. Y. 1965 Some analytical aspects of bubble dynamics. J. of Basic Engineering, ASME.

Hsu, C. C. 1975 Some remarks on the progress of cavity flow studies. J. of Fluids Engineering, ASME.

Isaacson, E. & Keller, H. B. 1966 Analysis of numerical methods. John Wiley & Sons.

James, R. M. 1972 On the remarkable accuracy on the vortex lattice method. Computer Methods in Applied Mechanics and Engineering, 1.

Klose, G. J. & Acosta, A. J. 1969 Unsteady force measurements on superventilated hydrofoils in heaving motion. J. Ship Research, vol. 13, No. 2.

Kristiansen, G.K. 1963 Zero of arbitary function, BIT, vol. 3.

Leehey, P. 1973 Supercavitating hydrofoils of finite span. Proceedings of the IUTAM Symposium in Leningrad, Nauka Publishing House, Moscow.

Leehey, P. & Stellinger, T. C. 1975 Force and moment measurement of supercavitating hydrofoils of finite span with comparison to theory. J. of Fluids Engineering, ASME.

Leone, P. C. 1968 Unsteady two-dimensional cavity flows. Ph.D disserentation, MIT.

Maixner, R. M. 1977 An experimental investigation of wall effects on supercavitating hydrofoils of finite span. MS thesis, MIT.

REFERENCES (CONTINUED)

Parkin, B. R.   1957 Fully cavitating hydrofoils in non-steady
     motion.   Engineering Division Report 85-2.

Reissner, E. & Stevens, J. E. 1967 Effect of finite span on
     the airload distributions for oscillating wings, II-
     methods of calculation and examples of application
     NACA TN-1195.

Riva, J. C. J. Design and calculation of a dynamometer for
     measurements of oscillatory forces on hydrofoils.
     MS thesis, MIT.

Smith, L. B., Keyes, F. G. & Gerry, H. T. 1934 Proc. American
     Acad. Arts and Science, vol. 69, No. 137.

Tsen, L. F. & Guilbaud, M.   1973 Heaving motion of ventilated
     trapezoidal hydrofoils.   Proc. of the Fourth Canadian
     Congress of Applied Mechanics, Monteal.

Unruh, J. F. & Bass, R. L. 1974 A general theory of unsteady
     load on cavitating hydrofoils. J. Hydraulics, vol.8,
     No. 4.

Wetzel, J. M. & Foerster, K. E. 1967 Unsteady force and cavity
     characteristics for ventilated hydrofoils.   Univ. of
     Minnesota, St. Anthony Falls Hydraulic Laboratory
     Project Report No. 85.

Widnall, S. E. 1966 Unsteady loads on supercavitating hydro-
     foils of finite span. J. Ship Research, vol. 10, No. 2.

Woods, L. C. 1957 Aerodynamic forces on an oscillating airfoil
     fitted with a spoiler. Proc. of the Royal Soc. Ser. A,
     vol. 239.

Table 4.1 Values of Vortex and Source Element

2-D Steady	No. of vortex element	No. of source element	
	25	40	

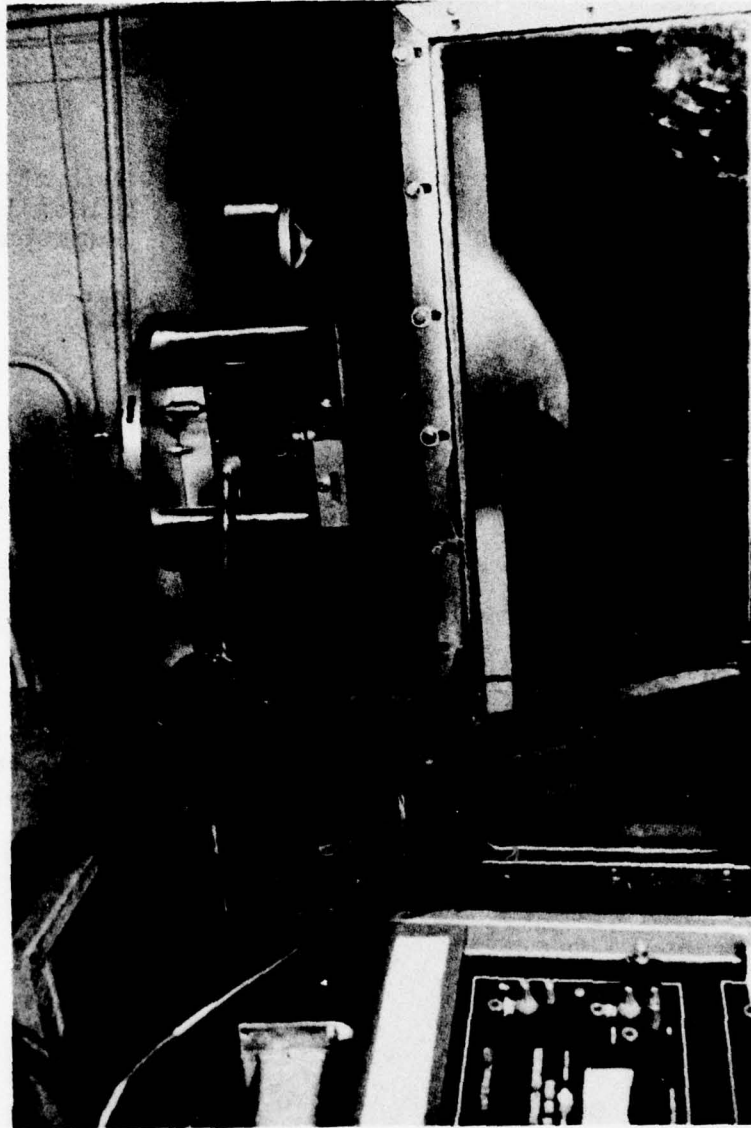| 3-D Steady	No. of element along the chord on the foil	No. of element in the cavity behind the foil	No. of element along the semispan
	12	8 to 14	6

2-D Unsteady	No. of vortex element	No. of source element	
	20	35 to 40	

3-D Unsteady	No of element along the chord on the foil	No. of element in the cavity behind the foil	No. of element along the semispan
	10	8 to 14	4

Figure 2.1 Tunnel Test Section and Driving System
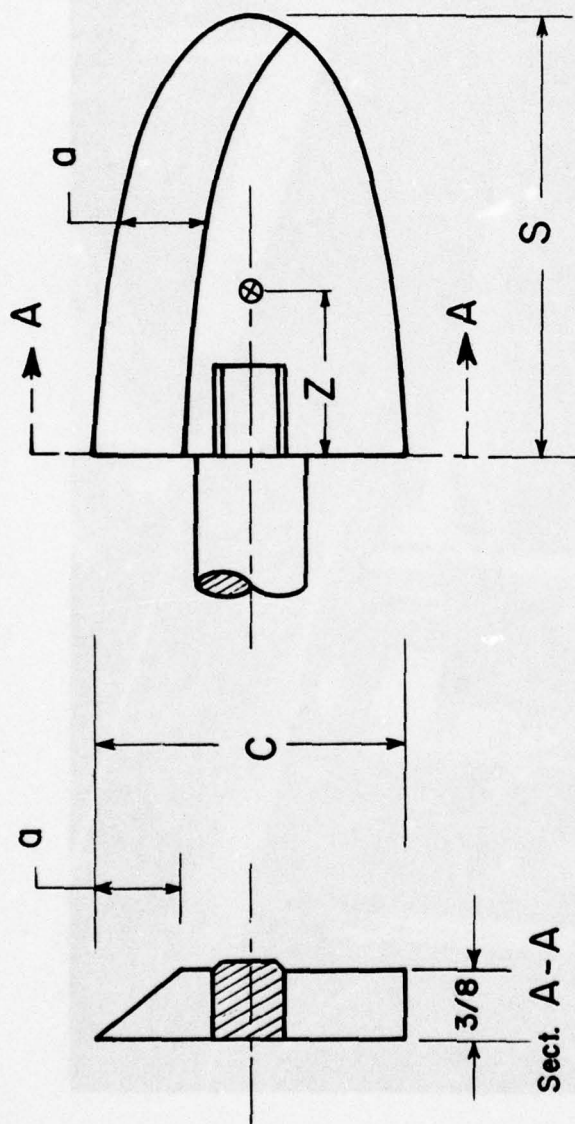
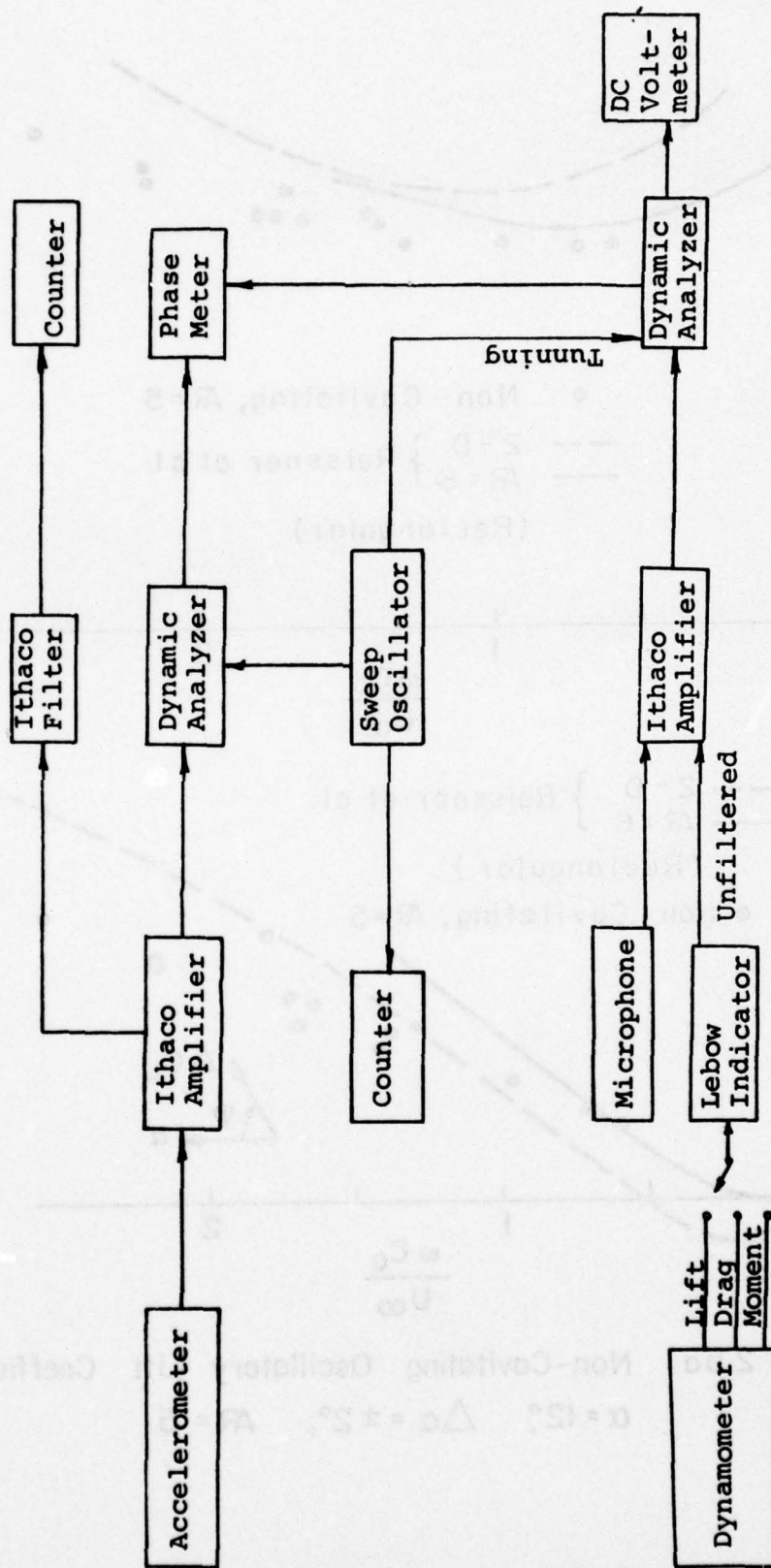| AR	C(in.)	S(in.)	a (in.)	Area (sq. in.)	Z (centroid pos.)
3	6.5	7.75	2.5	39.6	3.29
5	5.1	10.0	2.0	40.0	4.24

FIGURE 2.2 Hydrofoil Dimensions
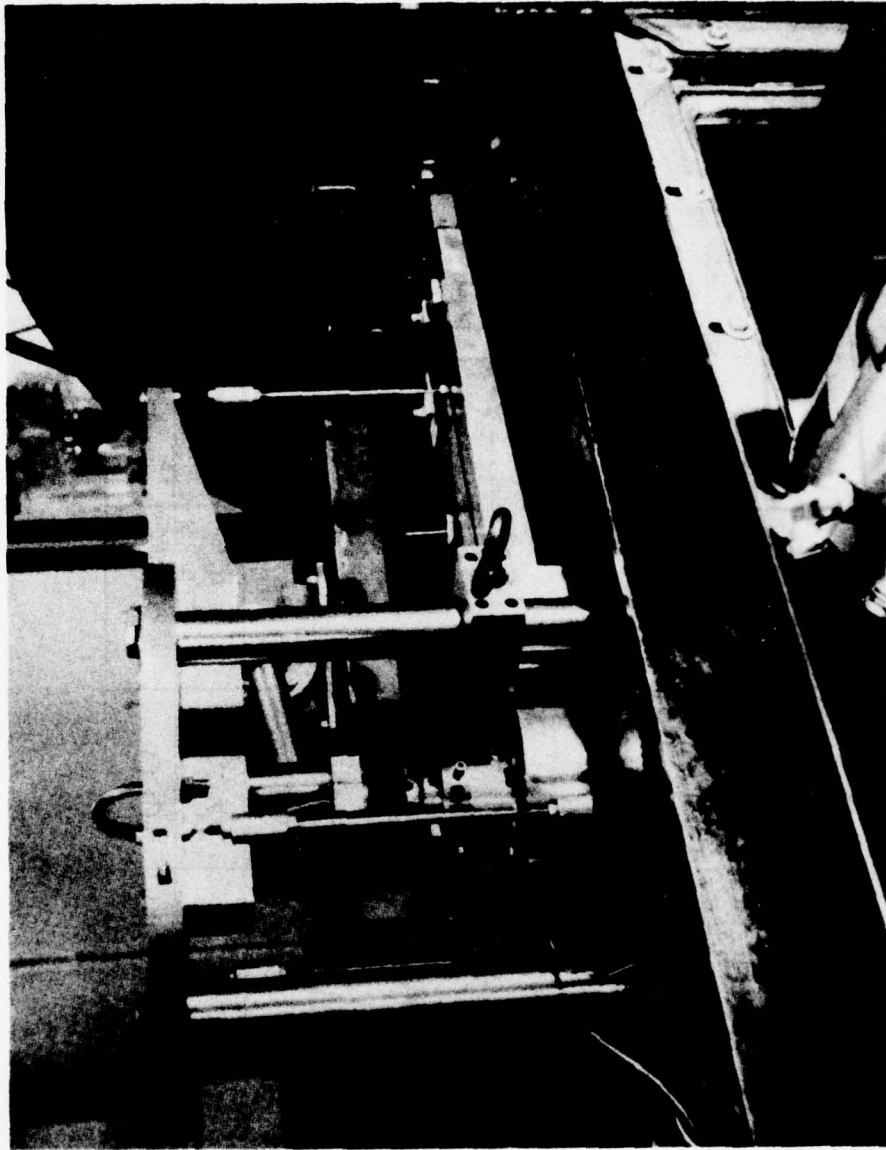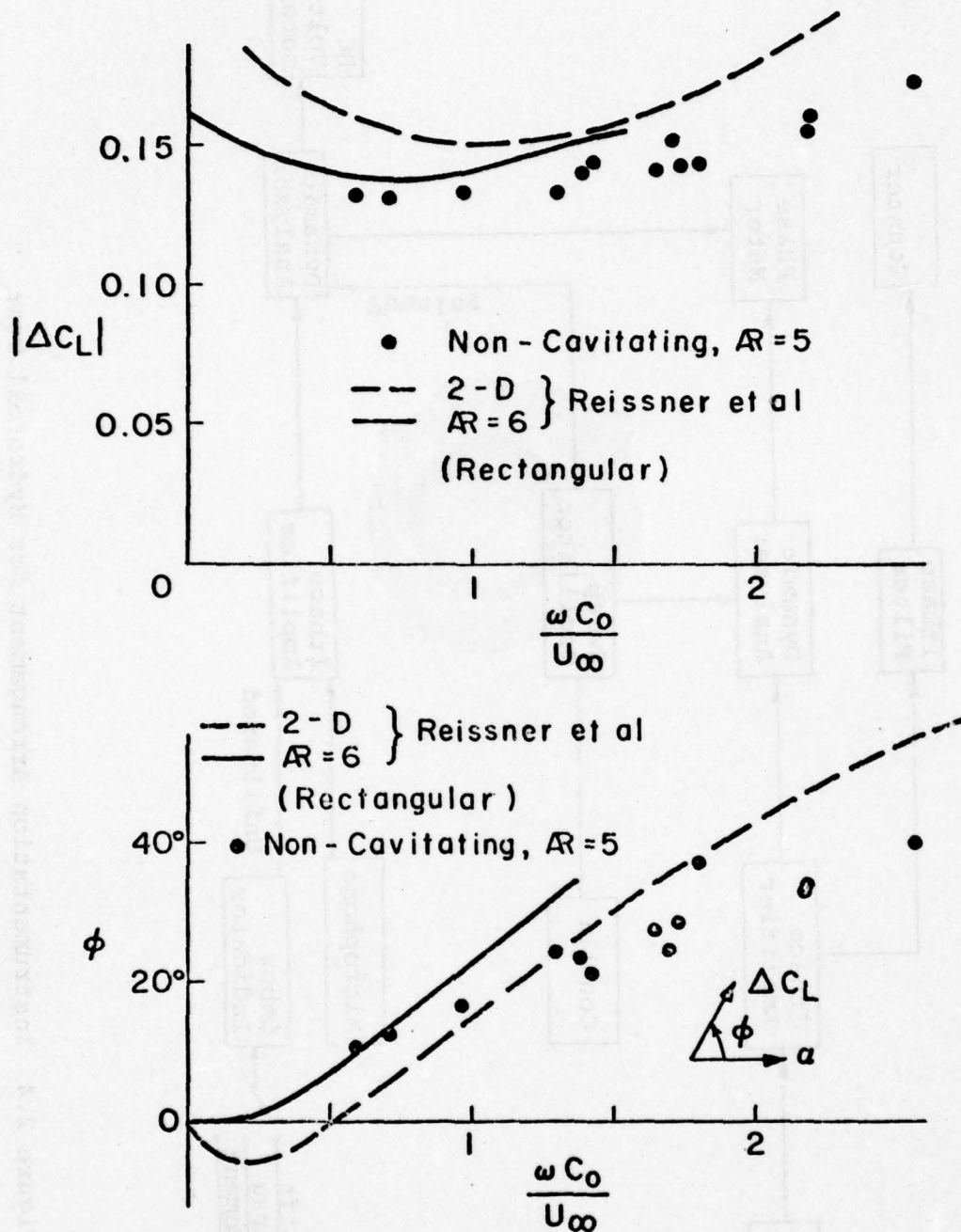
Figure 2.3 Dynamometer

Figure 2.4   Instrumentation Arrangement for Hydrofoil Test

FIGURE 2.5a   Non-Cavitating Oscillatory Lift Coefficient,
$\alpha = 12°$, $\triangle\alpha = \pm 2°$, $AR = 5$
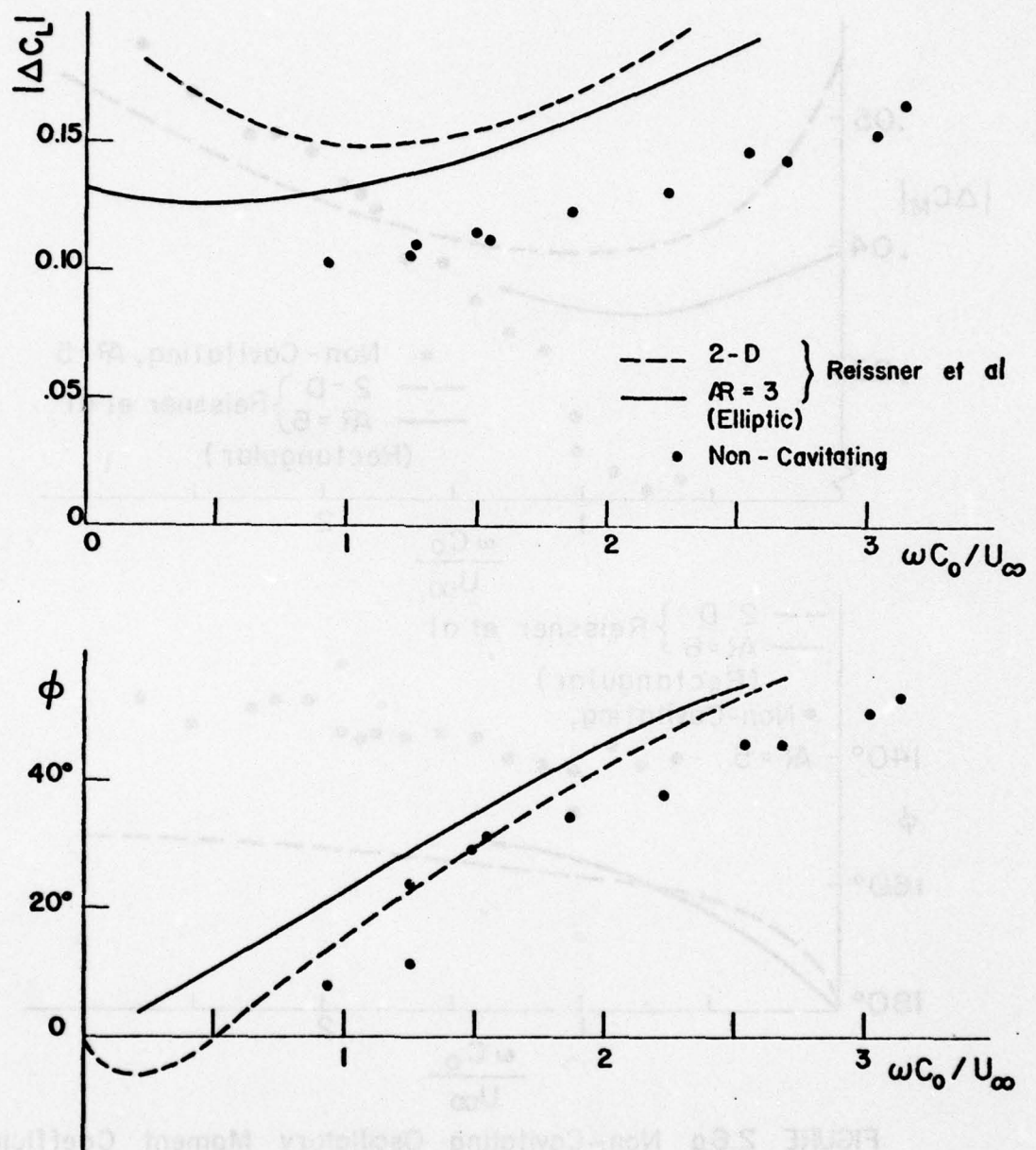
FIGURE 2.5b   Non-Cavitating Oscillatory Lift Coefficient,
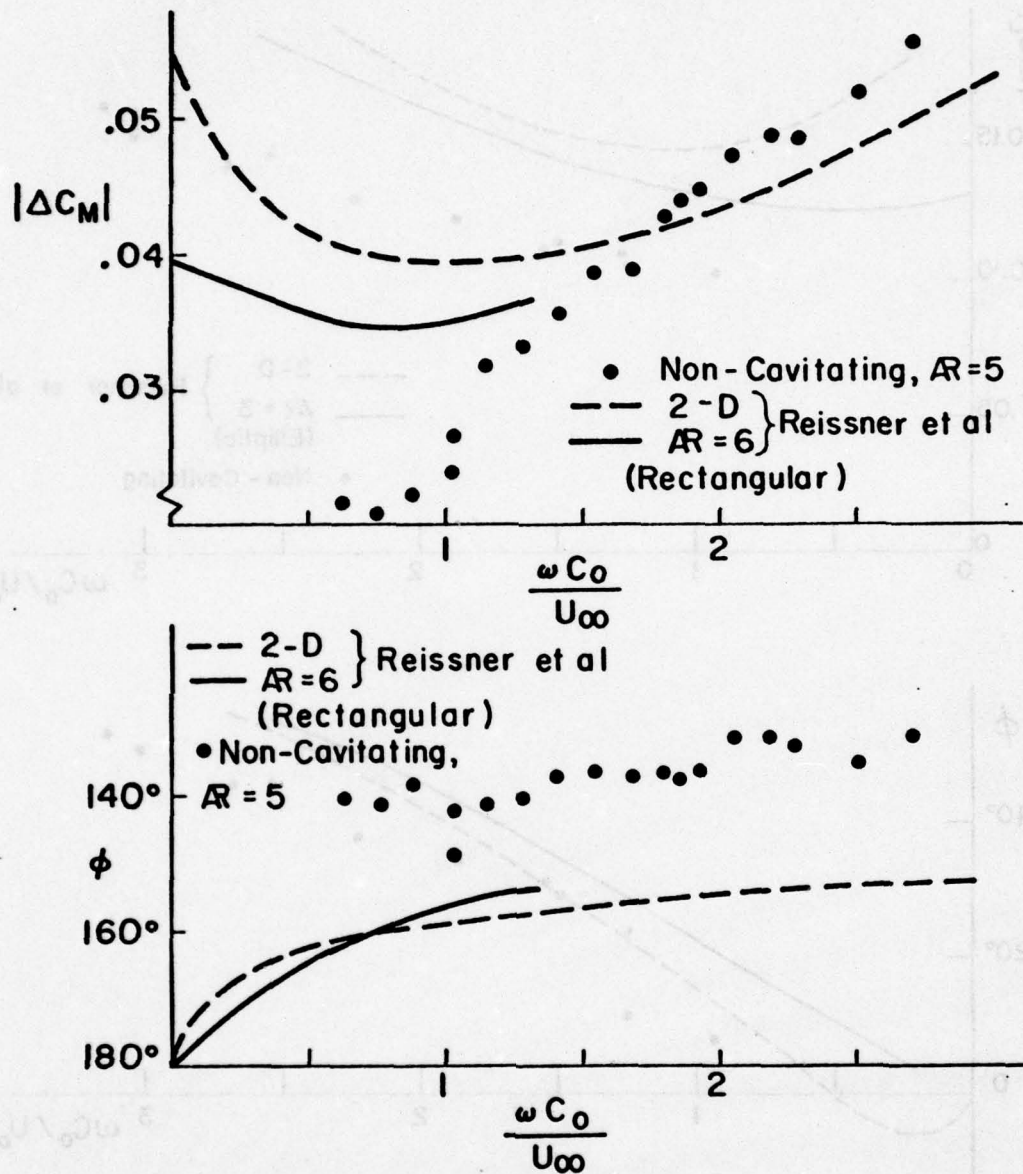
$\alpha = 12°$ $\Delta\alpha = \pm 2°$ $AR = 3$

FIGURE 2.6a Non-Cavitating Oscillatory Moment Coefficient
α = 12°, Δα = ±2°, AR = 5
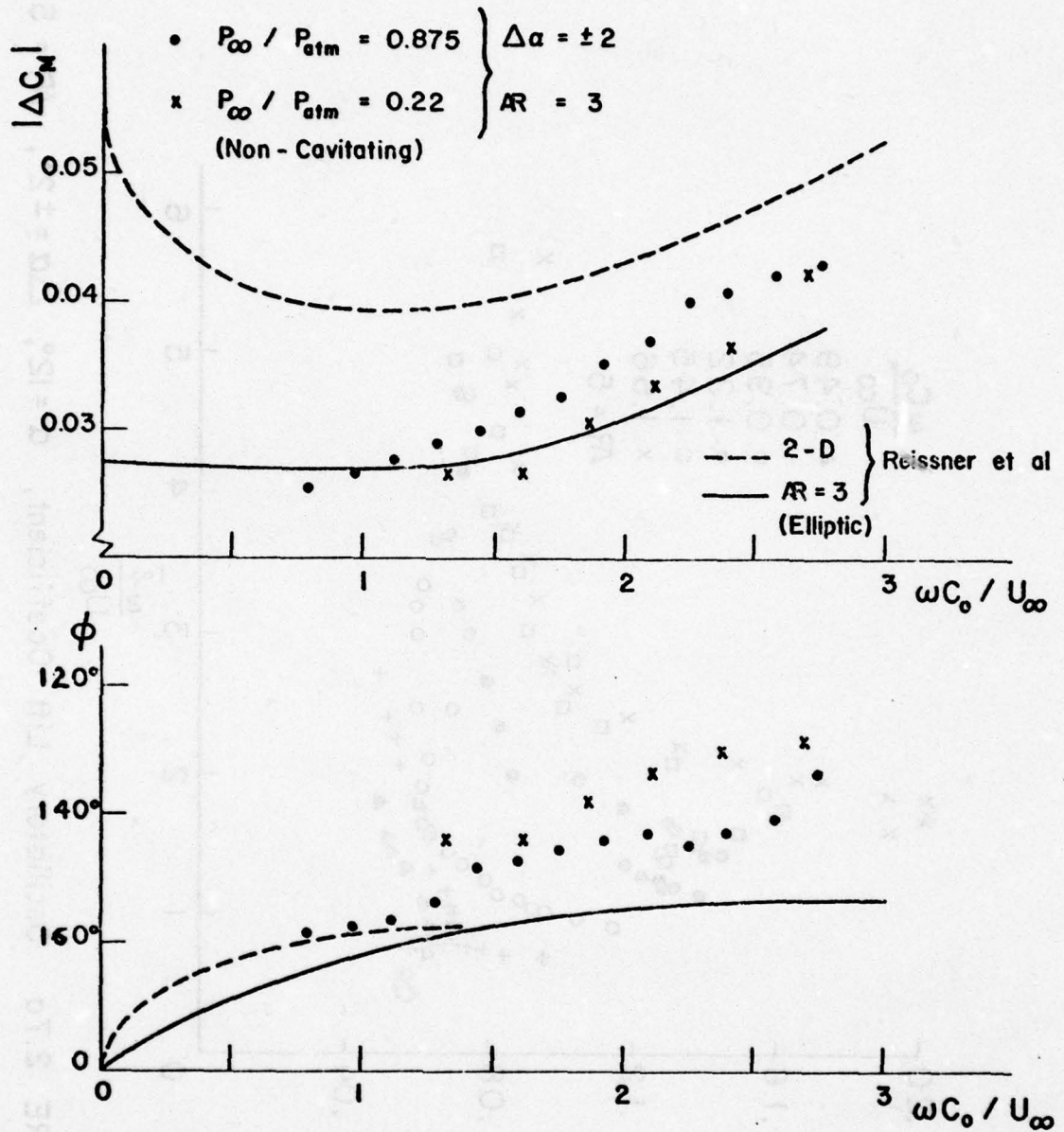
FIGURE 2.6b   Non-Cavitating Oscillatory Moment Coefficient
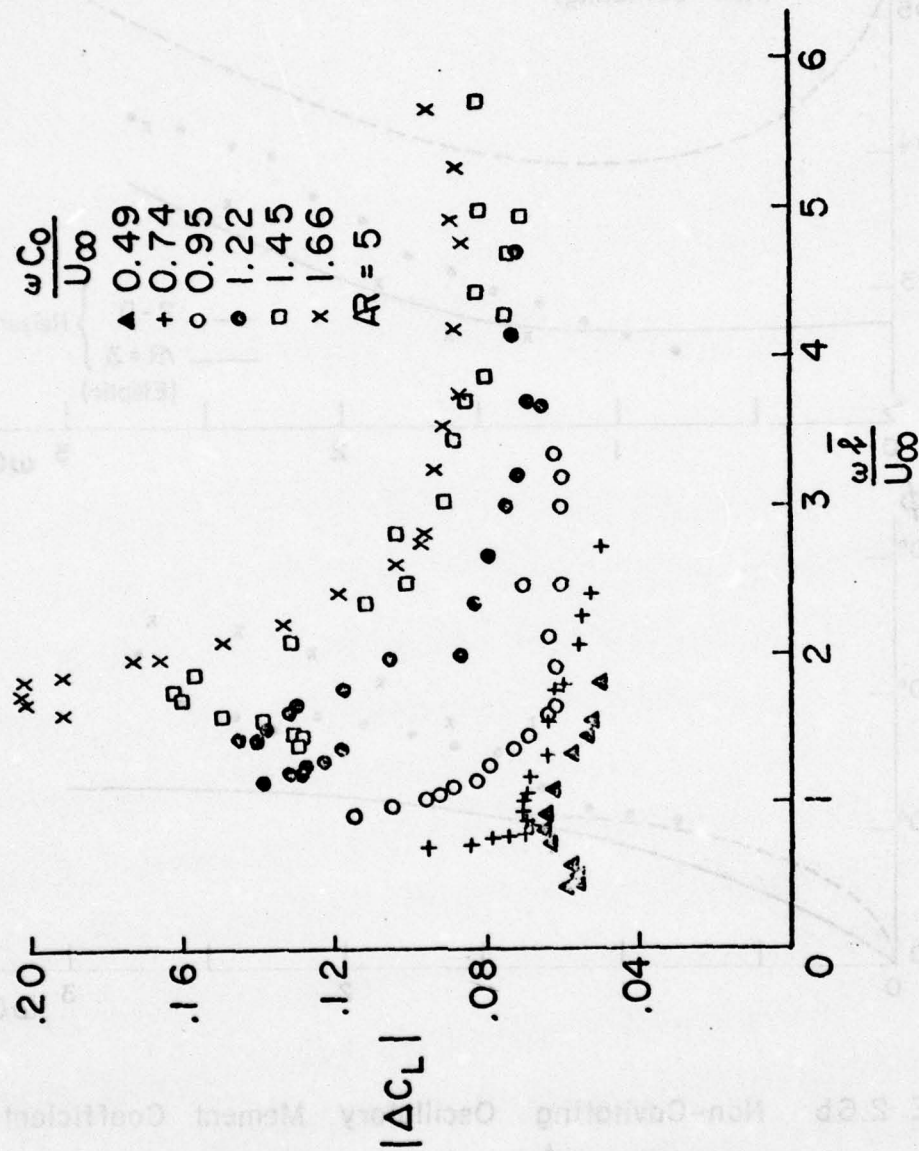
$\alpha = 12°$ $\Delta \alpha = \pm 2°$ $AR = 3$

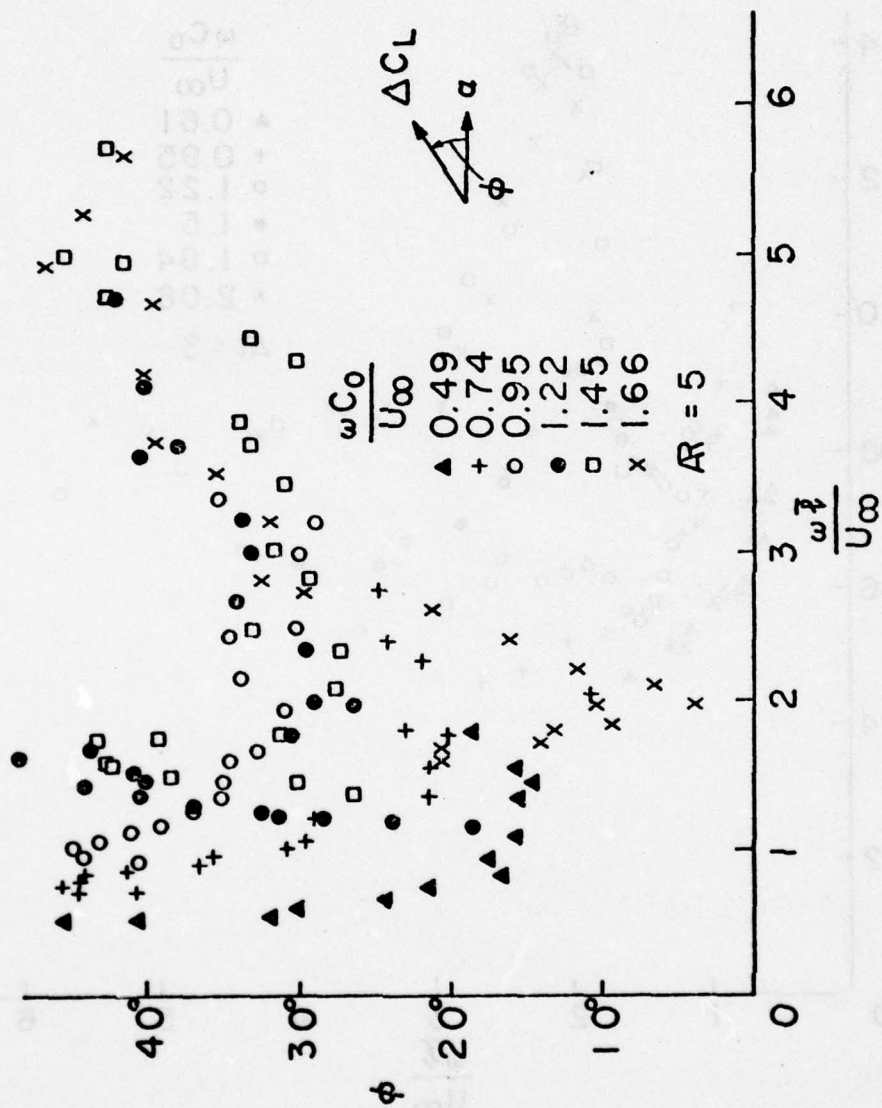FIGURE 2.7a Oscillatory Lift Coefficient, $\alpha = 12°$, $\Delta\alpha = \pm 2°$, $AR = 5$

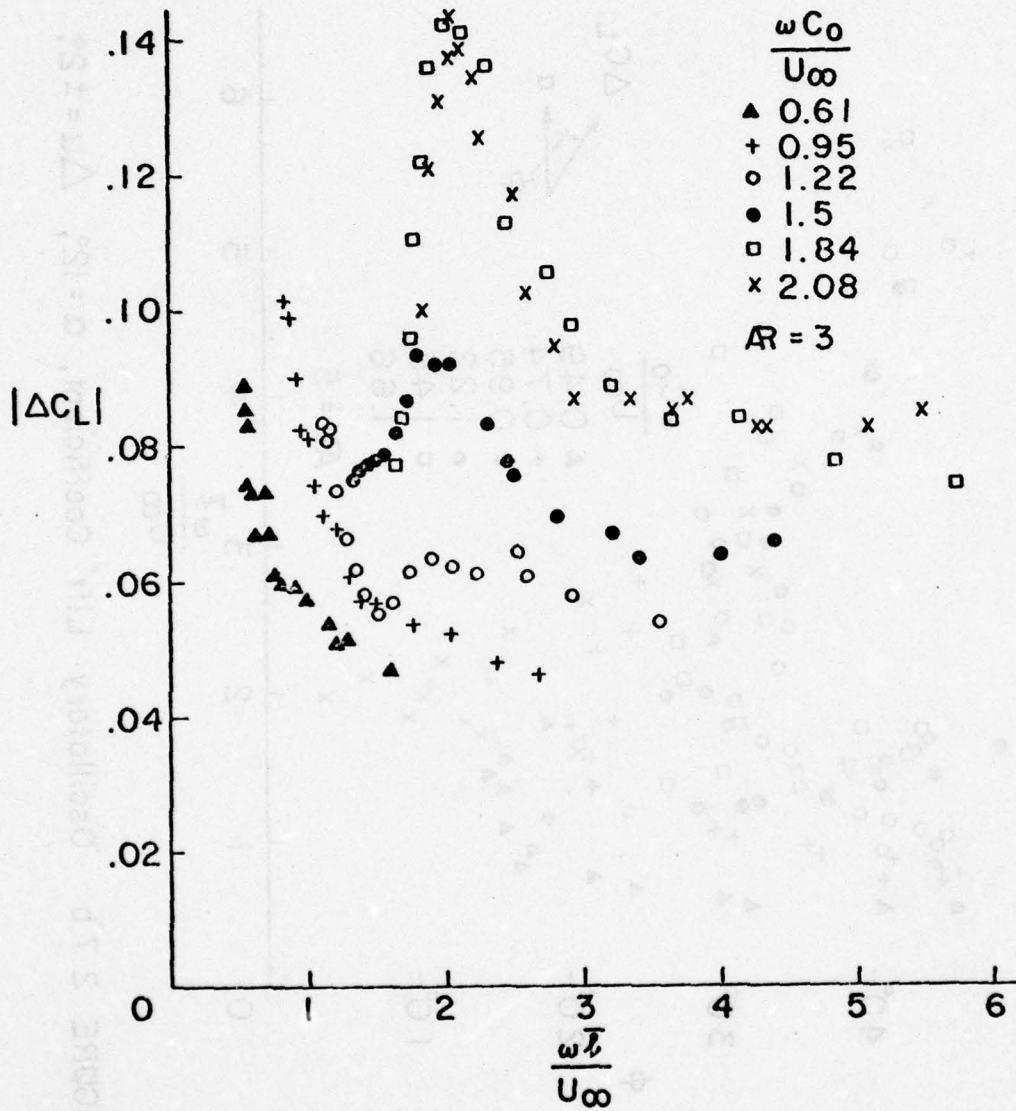FIGURE 2.7 b Oscillatory Lift Coefficient, $\alpha = 12°$, $\Delta\alpha = \pm 2°$, AR= 5

FIGURE 2.8 a   Oscillatory Lift Coefficient,
$\alpha = 12°$, $\triangle\alpha = \pm2°$, $AR = 3$
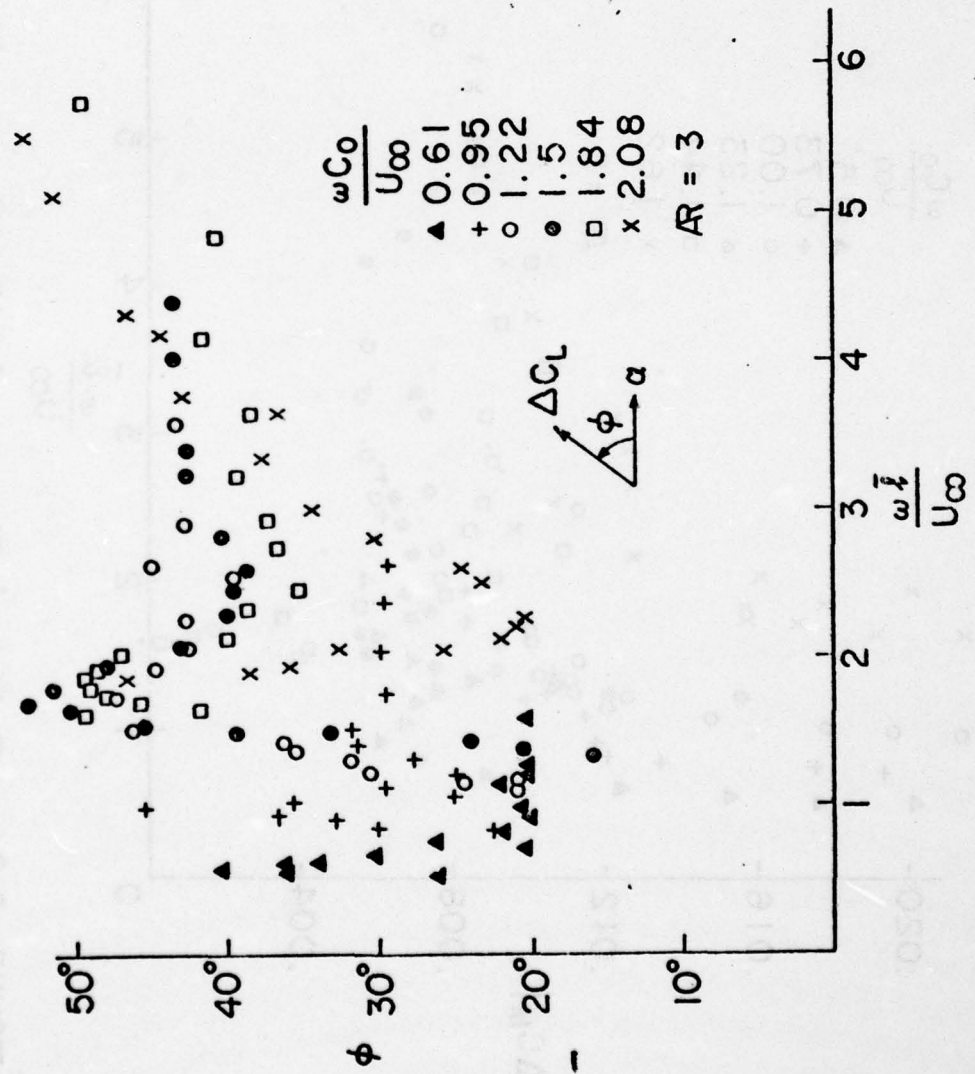
FIGURE 2.8b Oscillatory Lift Coefficient, $\alpha = 12°$, $\Delta\alpha = \pm 2°$, $AR = 3$

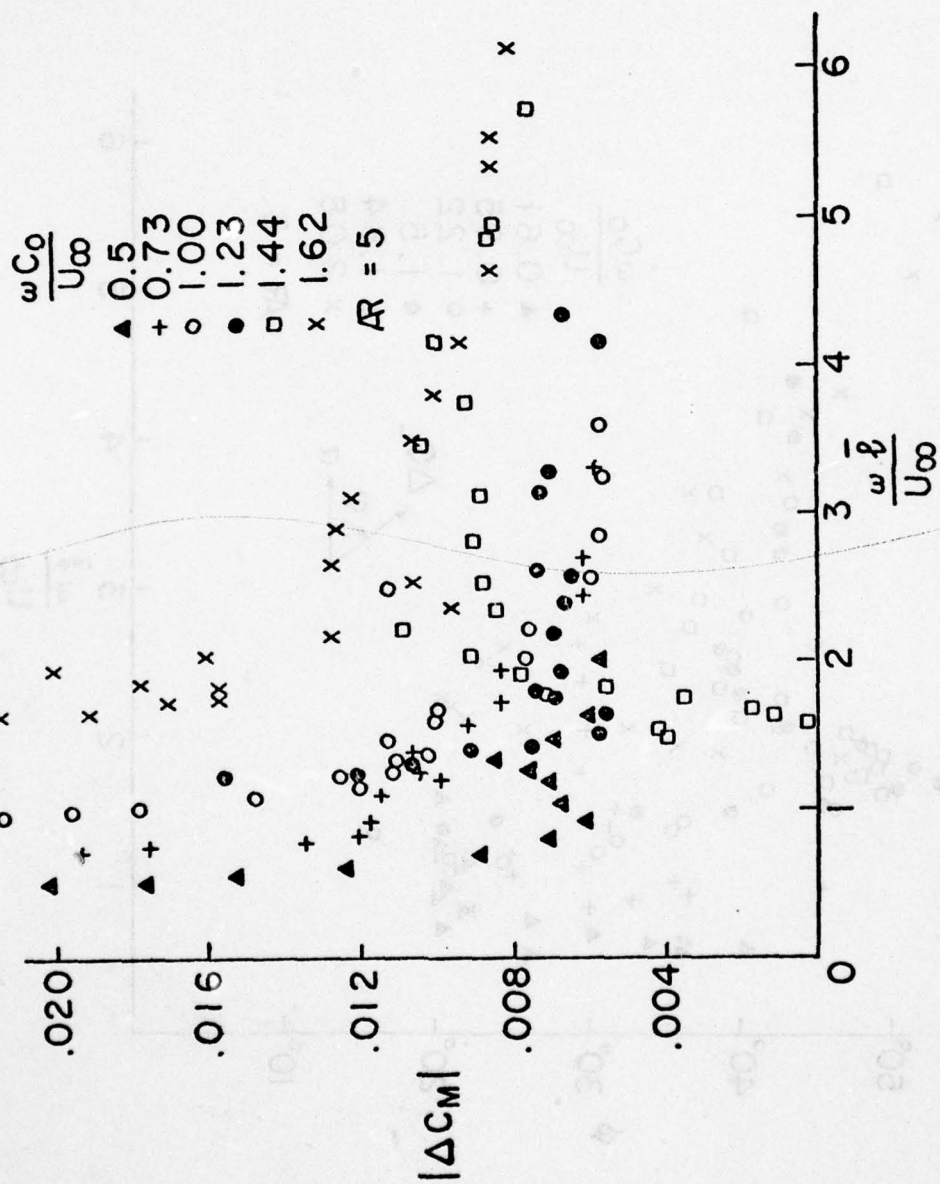FIGURE 2.9a   Oscillatory Moment Coefficient, $\alpha = 12°$, $\Delta\alpha = \pm 2°$, $AR = 5$

FIGURE 2.9b Oscillatory Moment Coefficient, $\alpha = 12°$, $\Delta\alpha = \pm 2°$, $AR = 5$

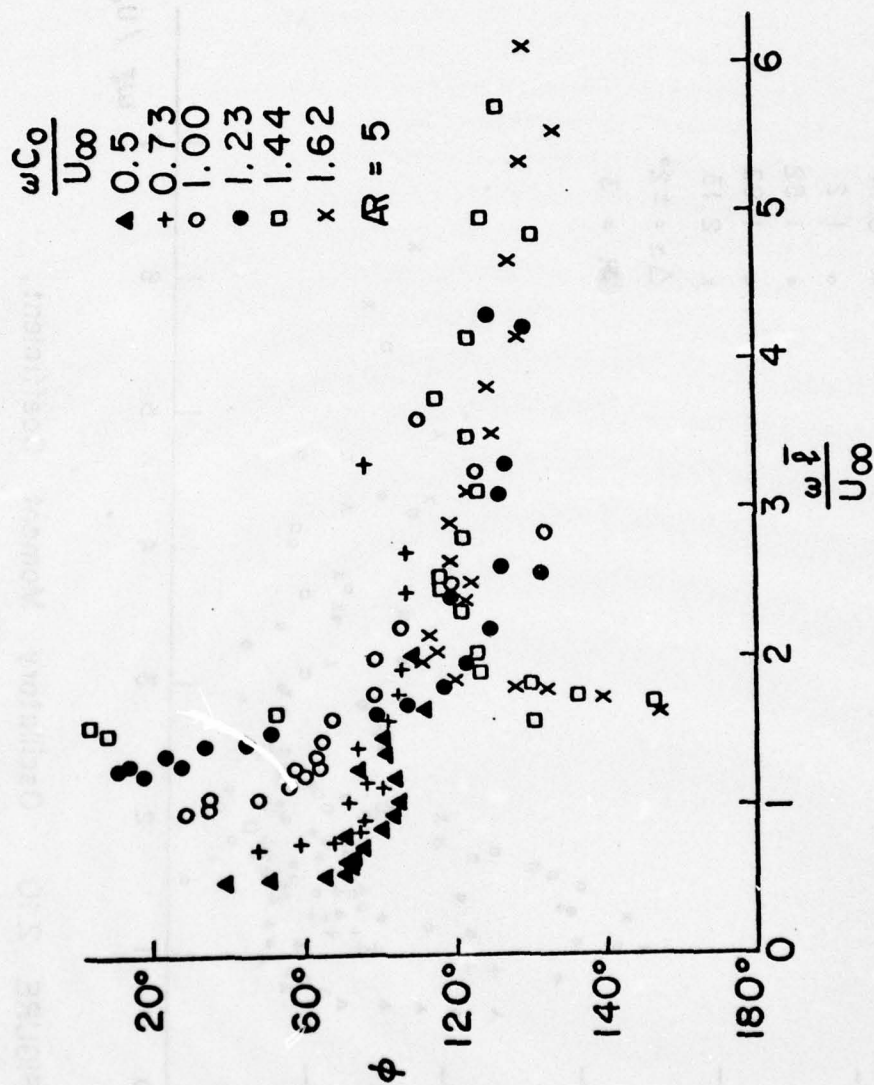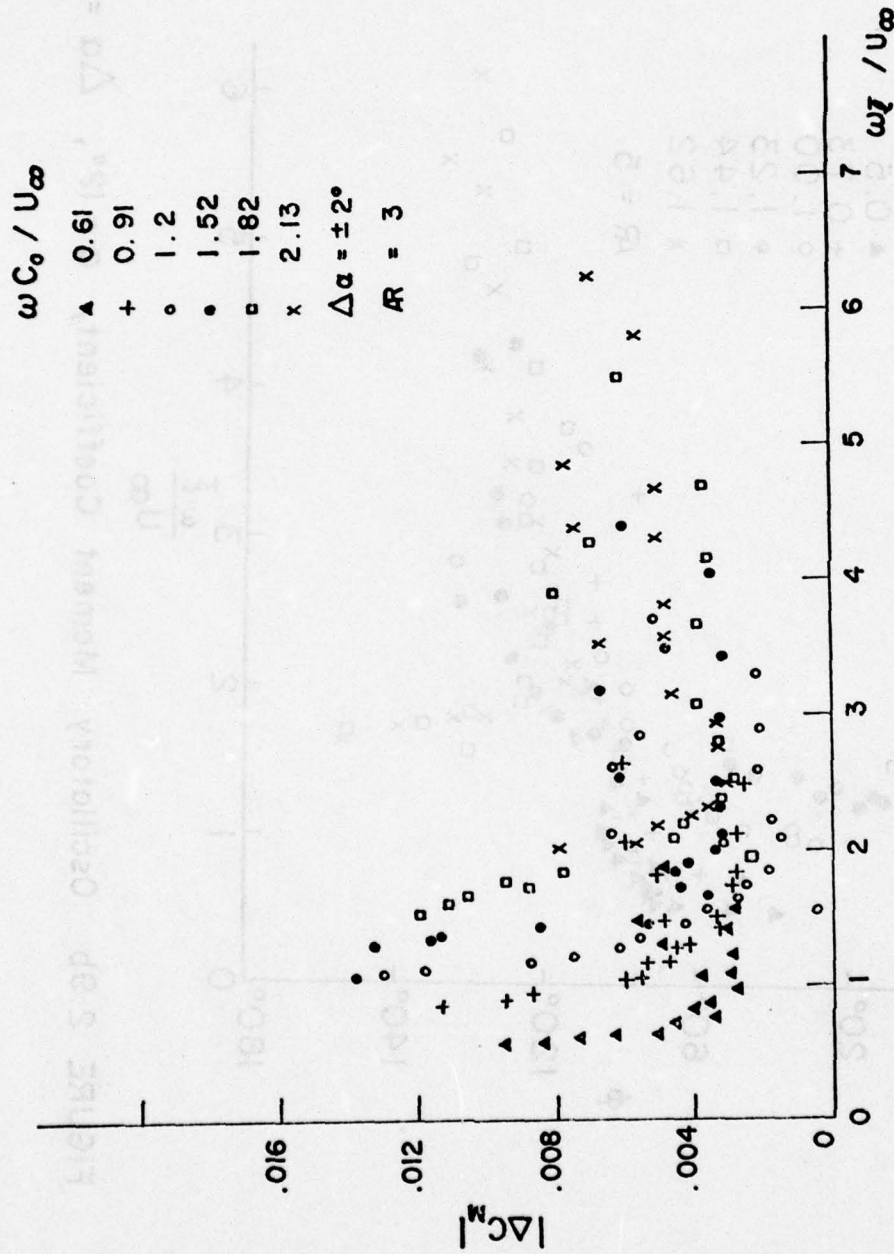FIGURE 2.10 Oscillatory Moment Coefficient,
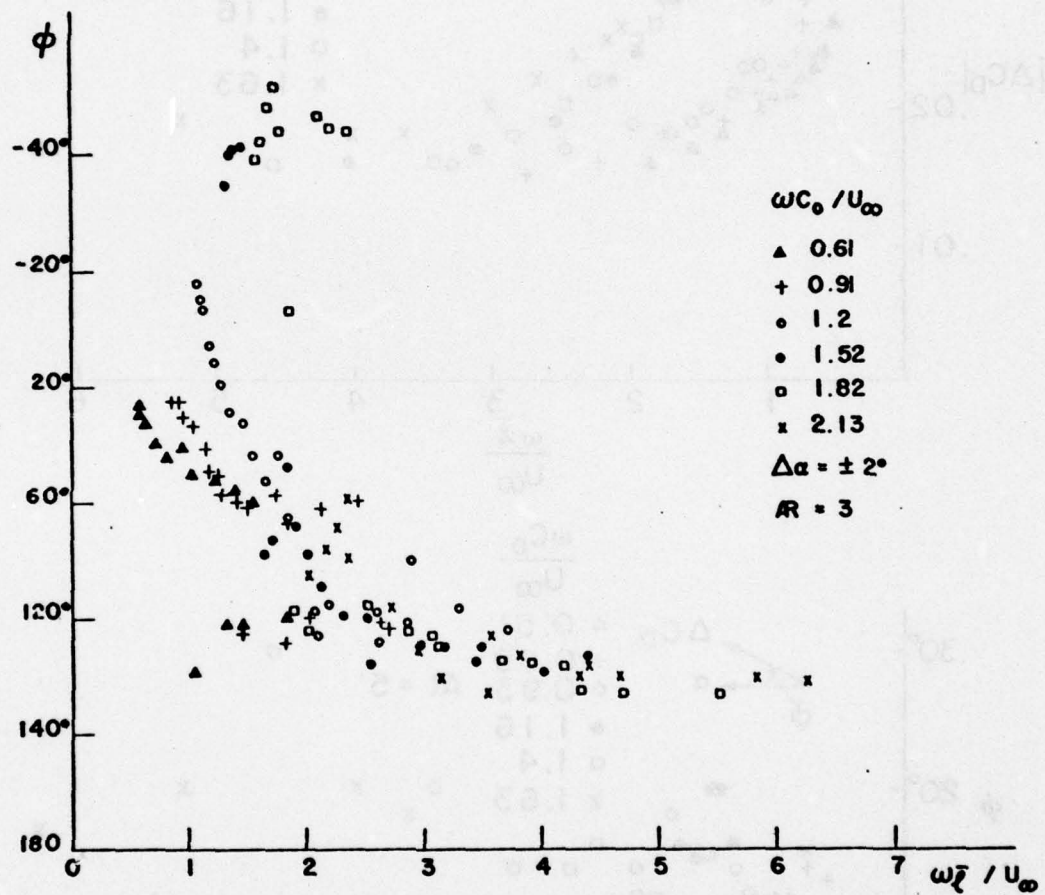
$\alpha = 12°$ $\Delta\alpha = \pm 2°$ $AR = 3$

FIGURE   2.10   Oscillatory Moment Coefficient,
$\alpha = 12°$ $\Delta\alpha = \pm 2°$ $R = 3$
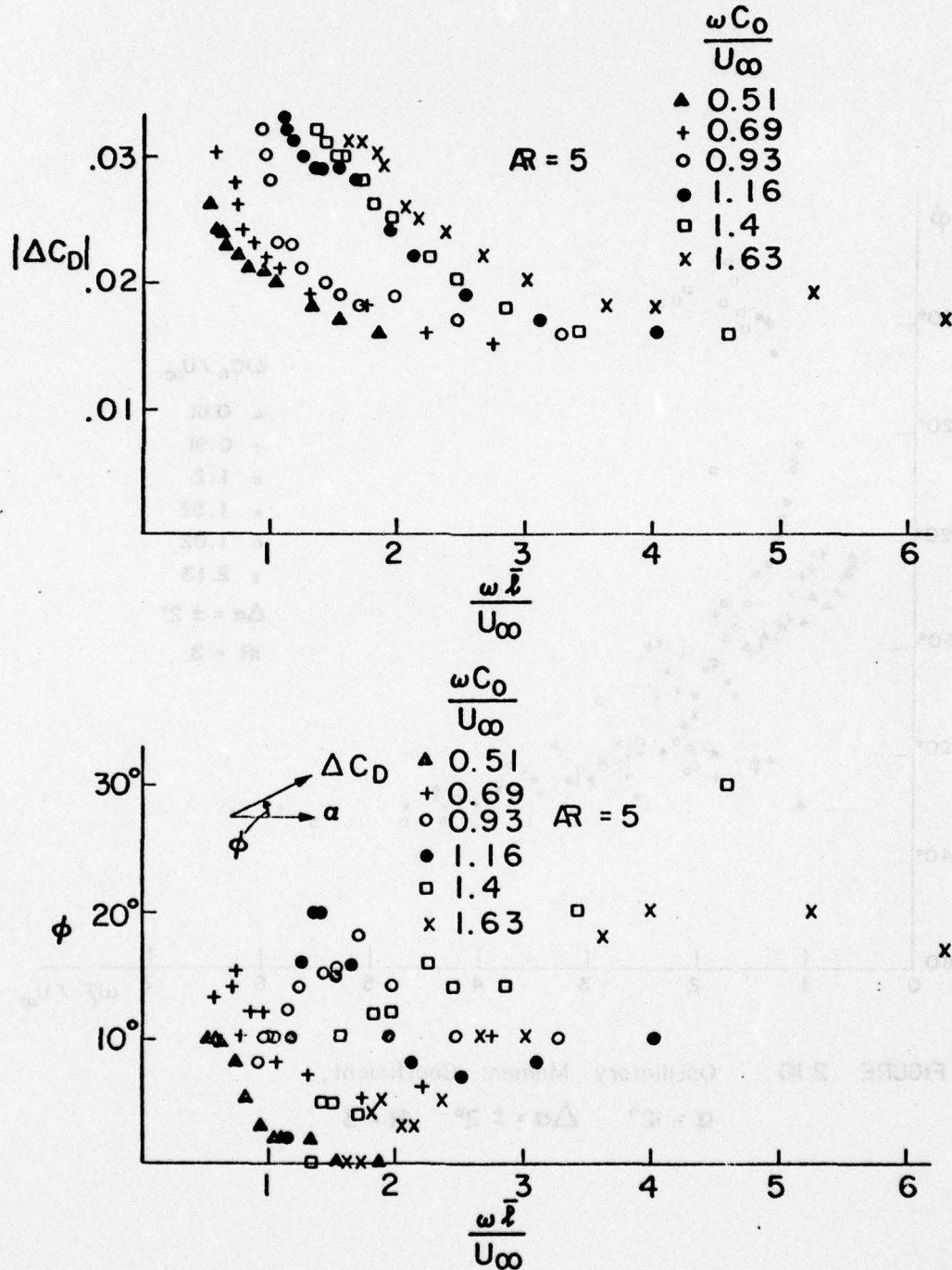
FIGURE 2.11 Oscillatory Drag Coefficient, $\alpha = 12°$, $\triangle \alpha = \pm 2°$, $\text{AR} = 5$
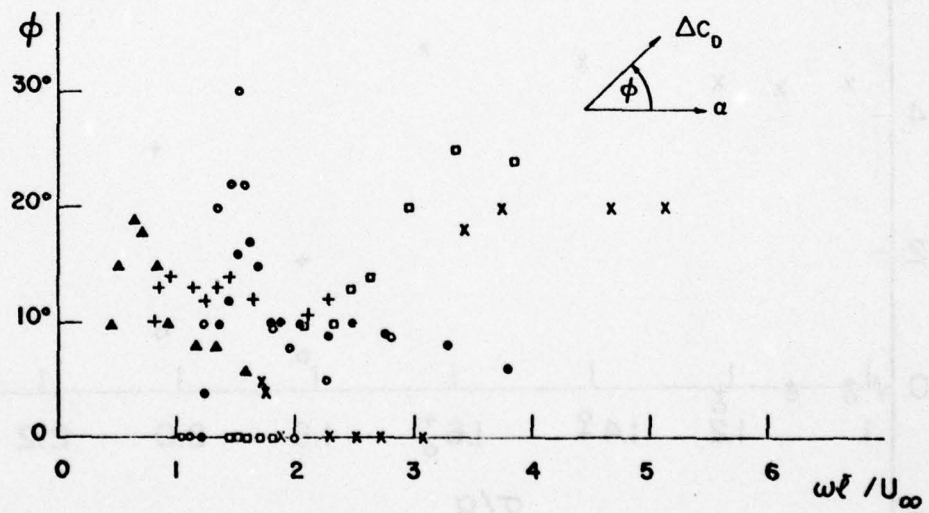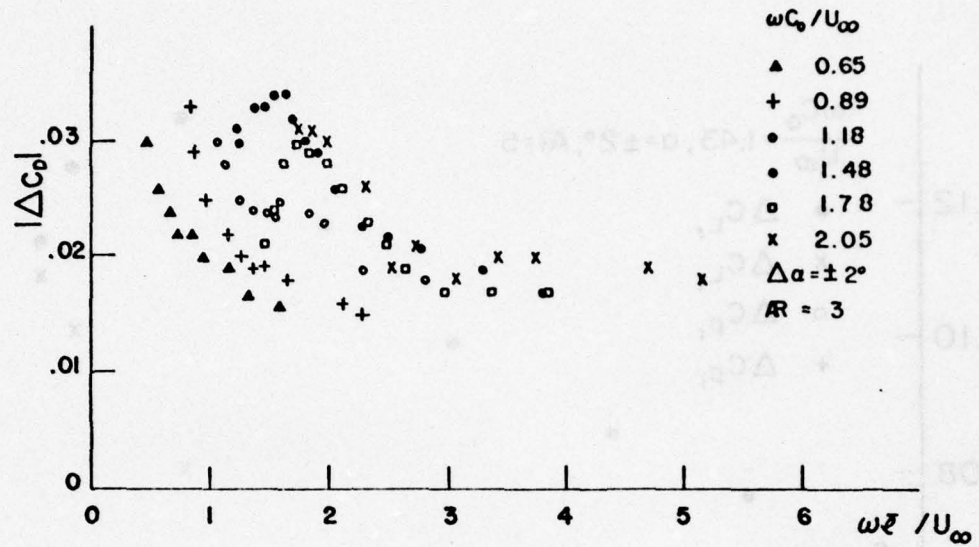
FIGURE 2.12 Oscillatory Drag Coefficient, $\alpha = 12°$, $\triangle \alpha = \pm 2°$, $AR = 3$

$$\frac{\omega C_0}{U_\infty} = 1.43, \ \alpha = \pm 2^\circ, \ \text{AR} = 5$$

● ΔC_{L_r}

✕ ΔC_{L_i}

○ ΔC_{p_r}

+ ΔC_{p_i}

.12

.10

.08

.06

.04

.02

0

-.02

1   1.2   1.4   1.6   1.8   2.0   2.2

σ/α
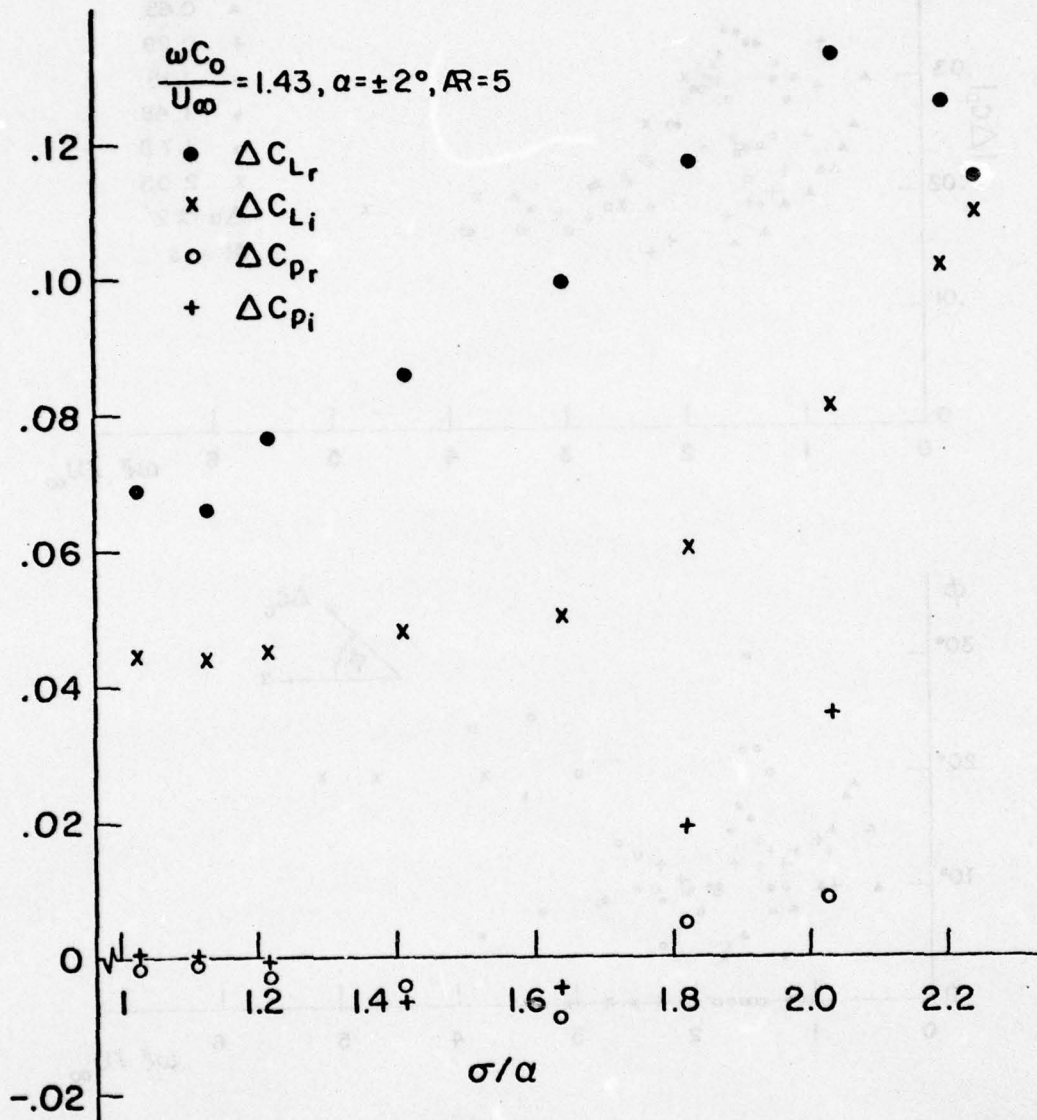
FIGURE 2.13 a   Oscillatory Lift and Cavity Pressure

Coefficients   at $\omega C_o/U_\infty = 1.43$, AR = 5
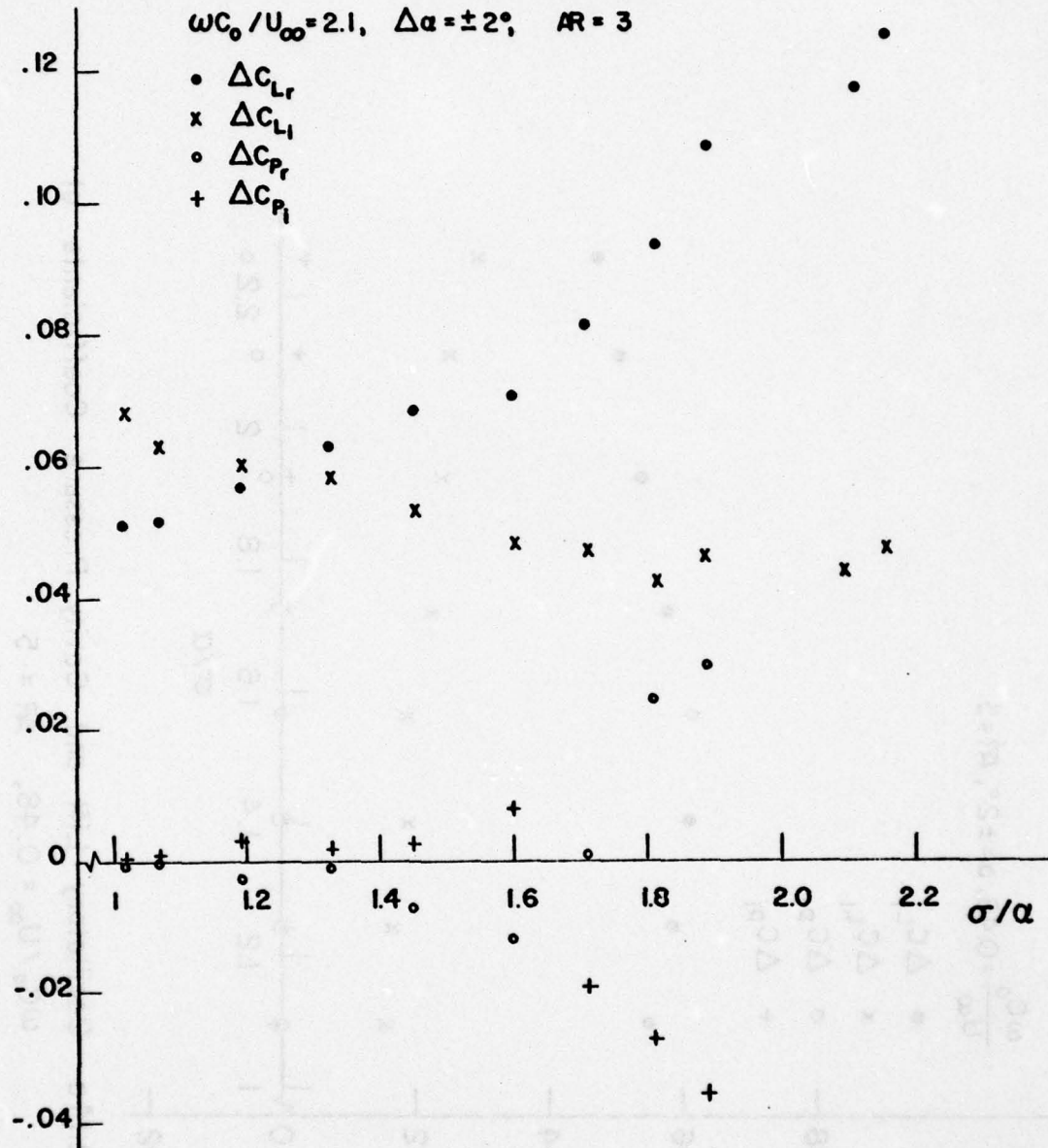
FIGURE 2.13 b   Oscillatory Lift and Cavity Pressure
Coefficients at $\omega C_0 / U_\infty = 2.1$, AR = 3
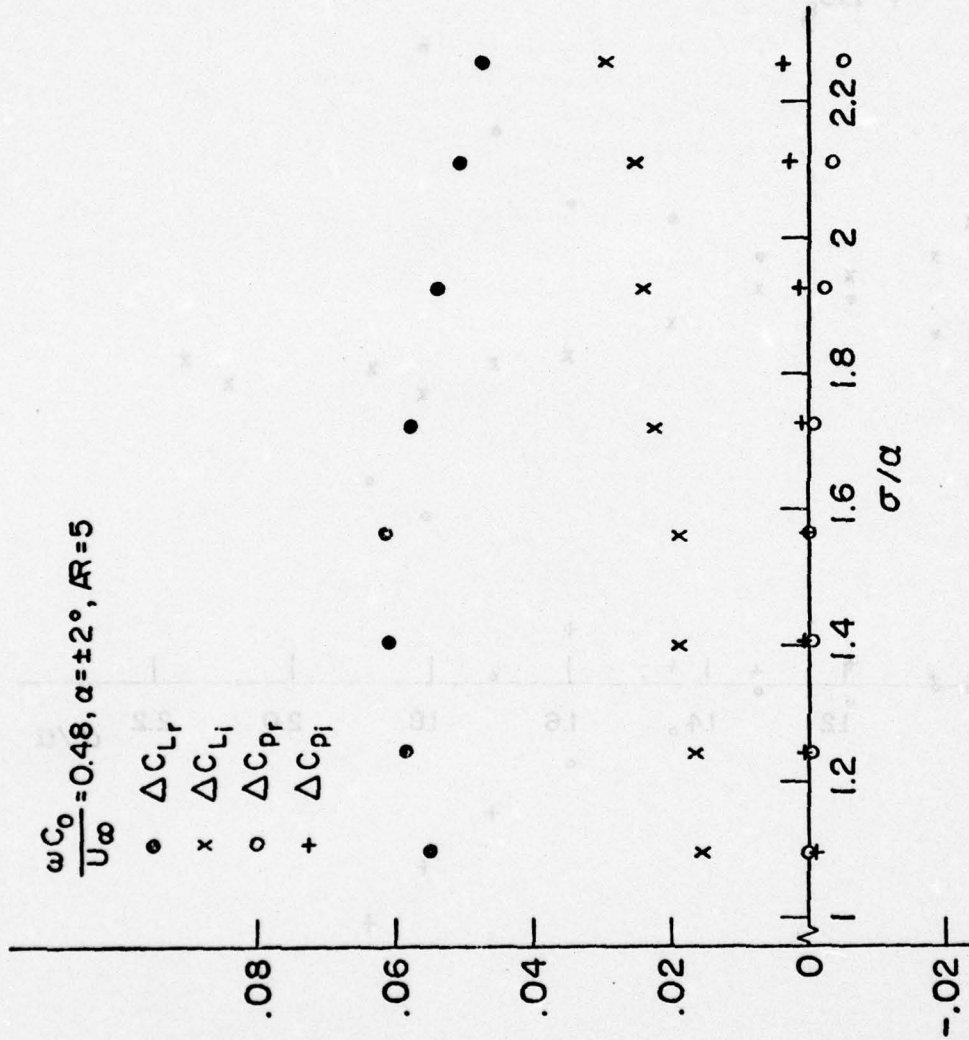
FIGURE 2.14a Oscillatory Lift and Cavity Pressure Coefficients at $\omega C_o / U_\infty = 0.48$, AR = 5
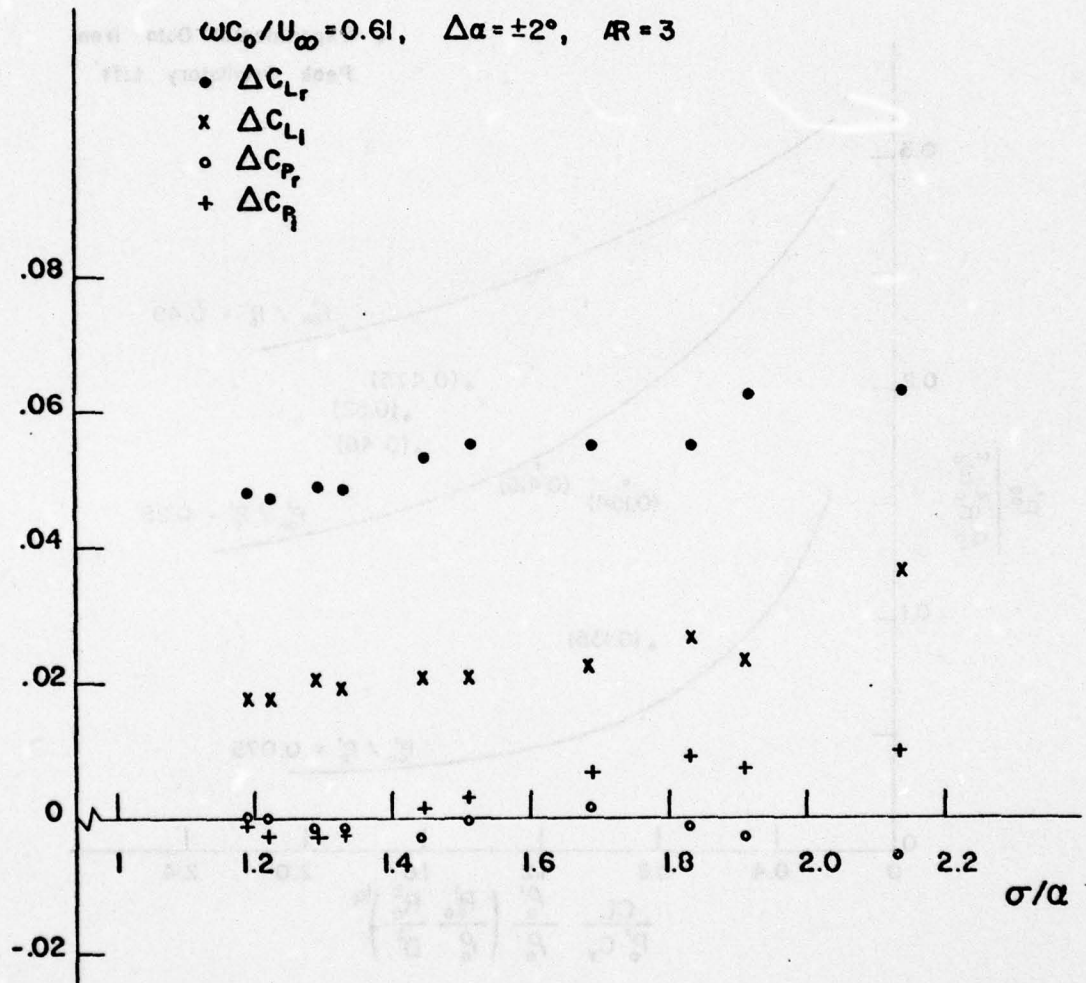
FIGURE 2.14b   Oscillatory Lift and Cavity Pressure
Coefficients at $\omega C_0/U_\infty = 0.61$, $AR = 3$
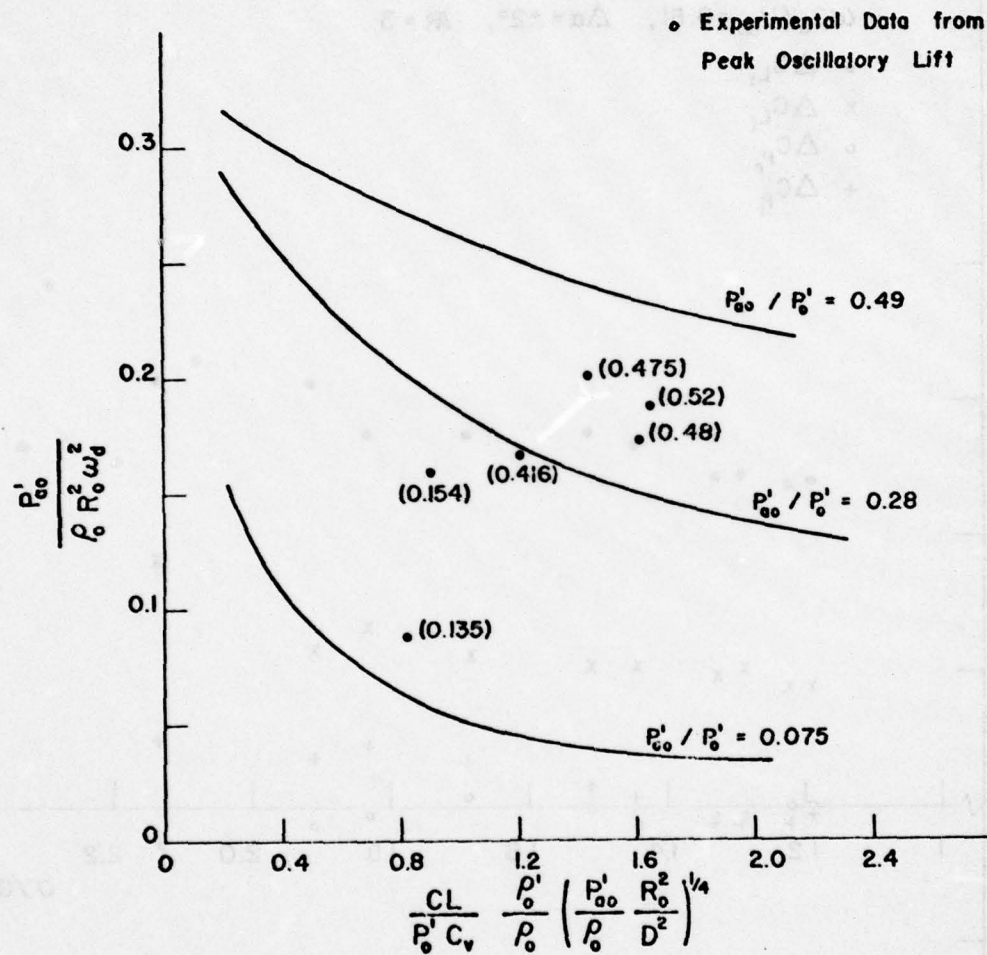
FIGURE 3.1 Natural Frequency of Air-Vapor Bubble
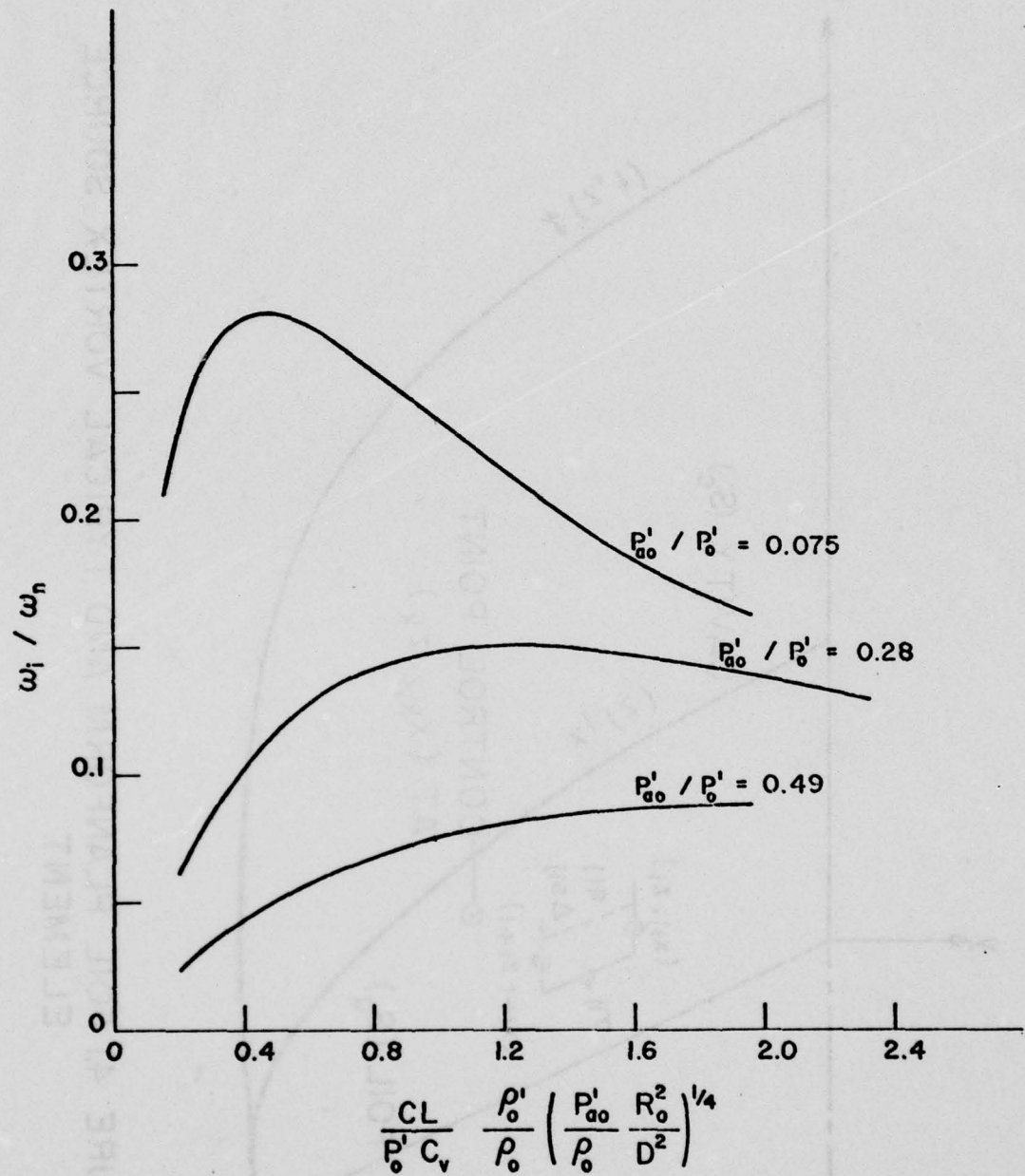
FIGURE 3.2 Damping Ratio of Air-Vapor Bubble
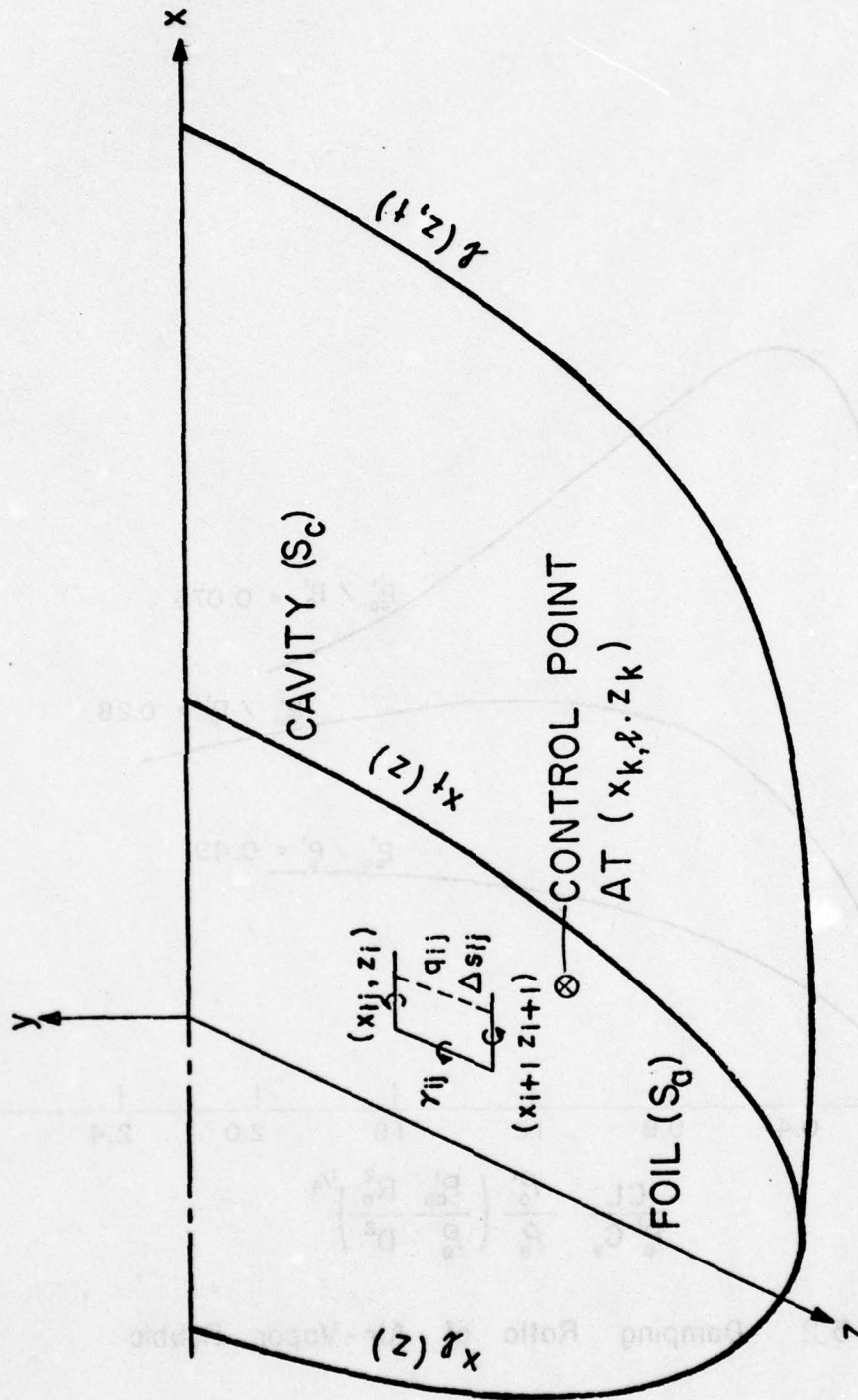
FIGURE 4.1 FOIL PLANFORM AND TYPICAL VORTEX SOURCE ELEMENT
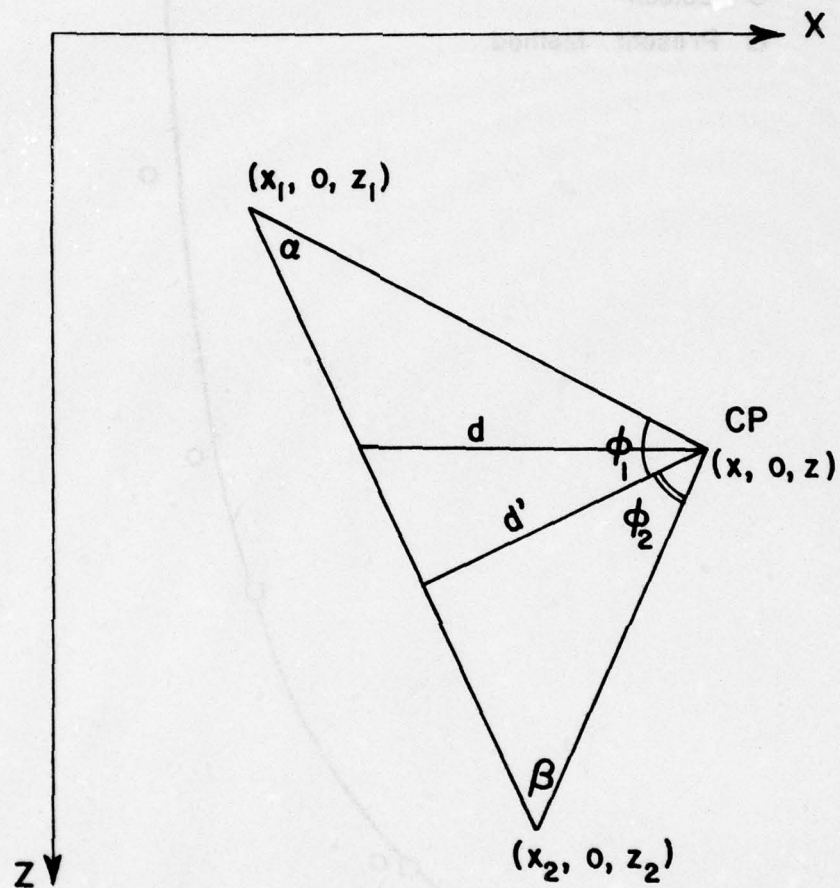
FIGURE 4.2 Coordinate Systems for Discrete Source Segment and Control Point
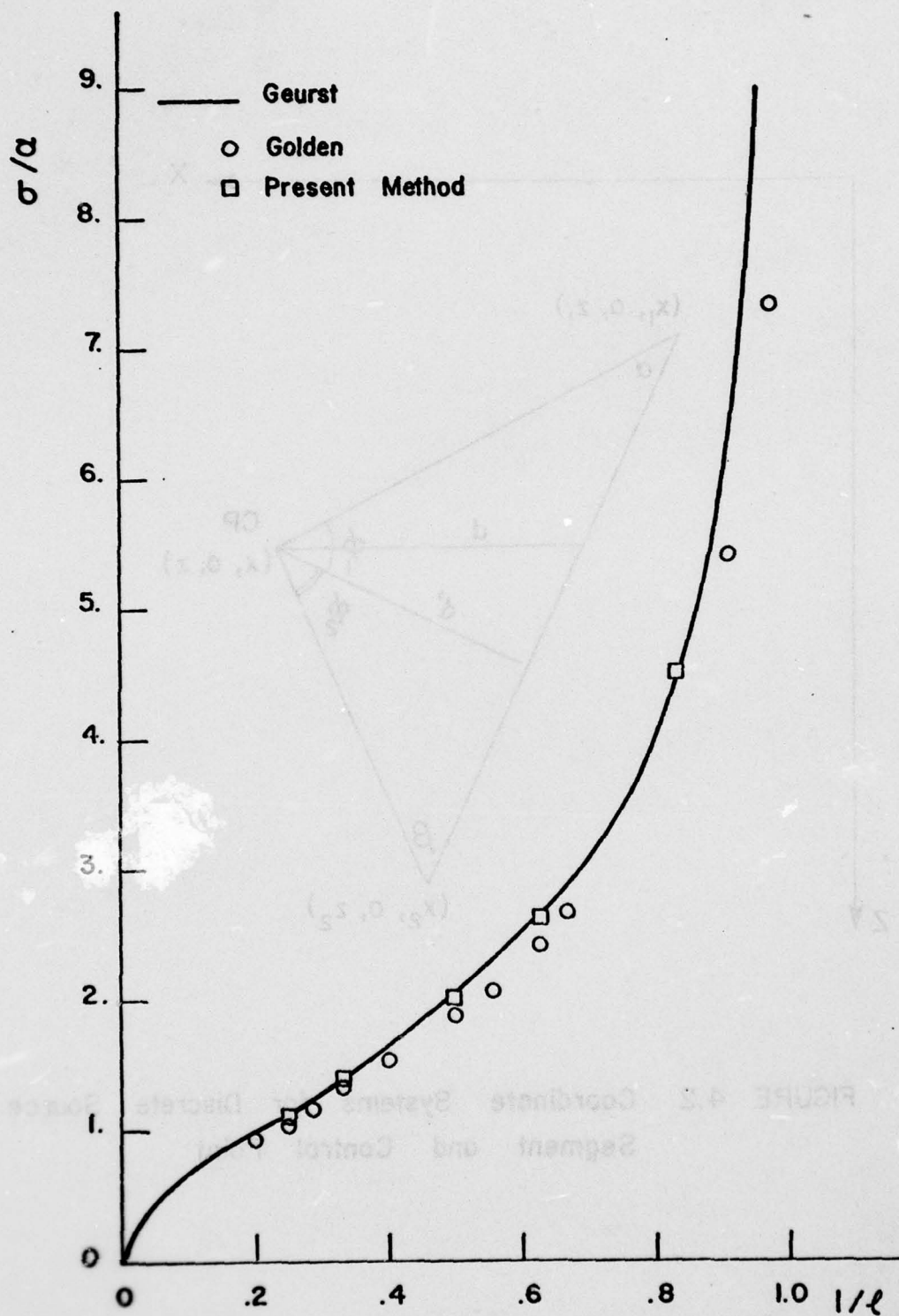
FIGURE 4.3   Cavity Length vs. σ/α.   Flat   Plate
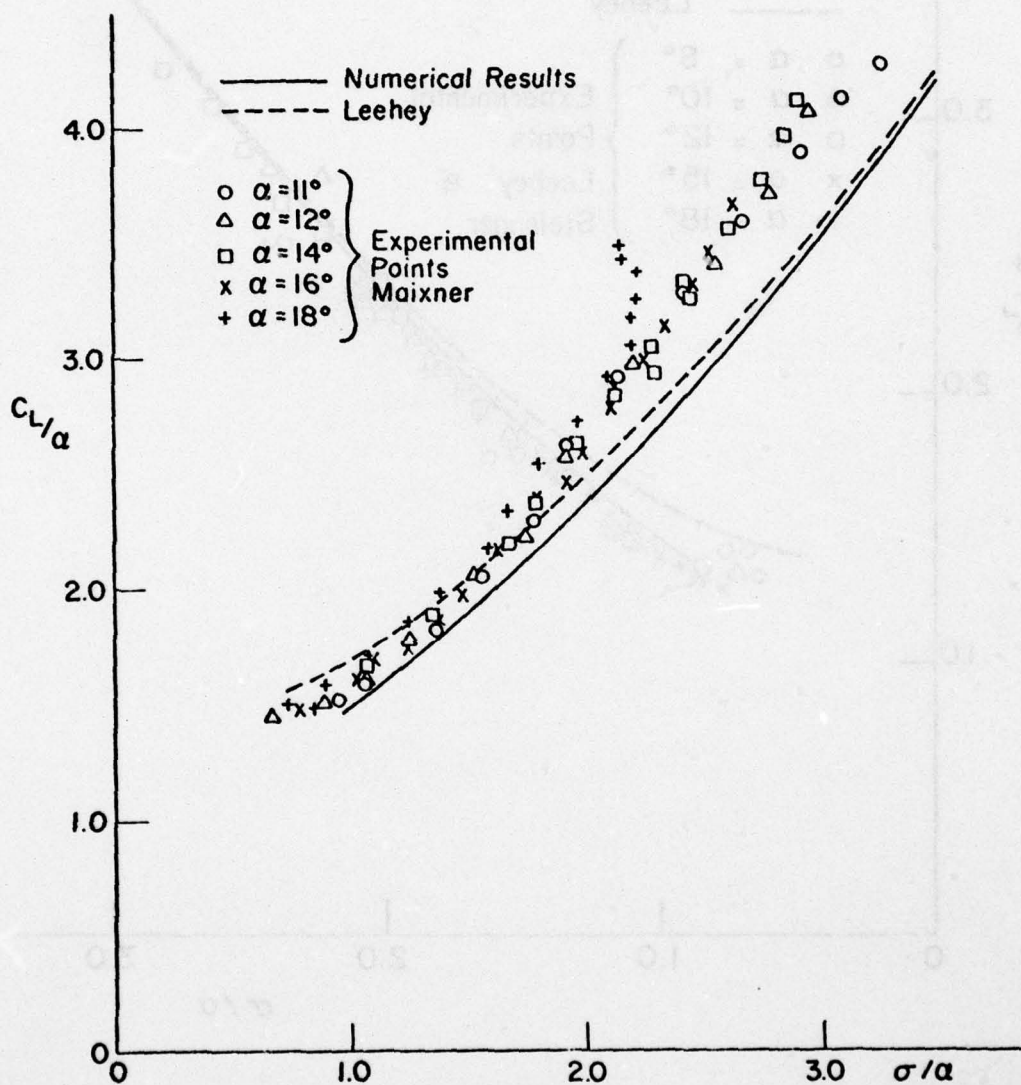
FIGURE 4.4 C_L/α vs. σ/α, $AR = 5$
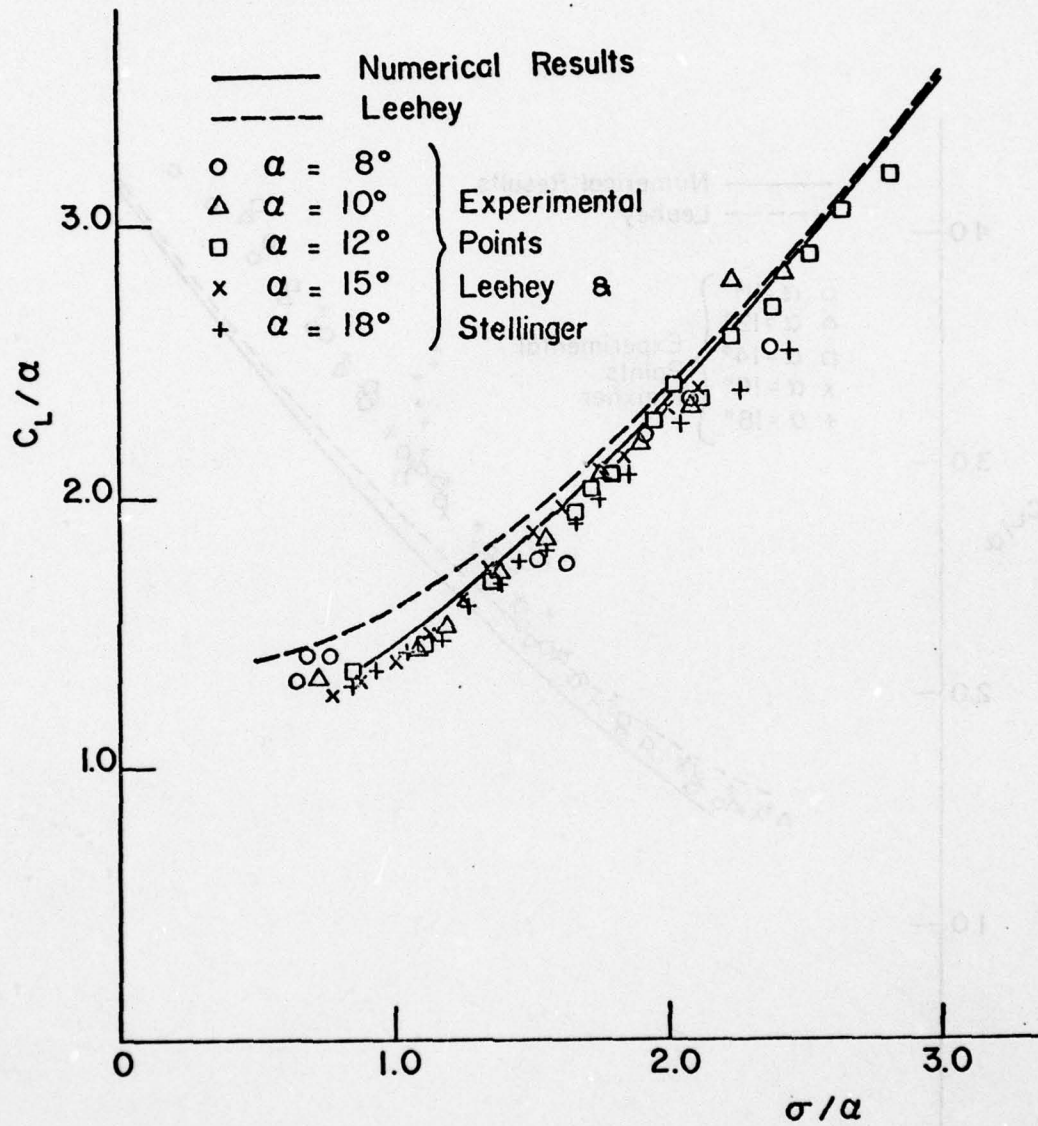
FIGURE 4.5 C_L/α vs. σ/α, AR = 3

FIGURE 4.6 C_M / α vs. σ / α, $AR = 5$

FIGURE 4.7 C_M/α vs. σ/α, $\text{Æ} = 3$
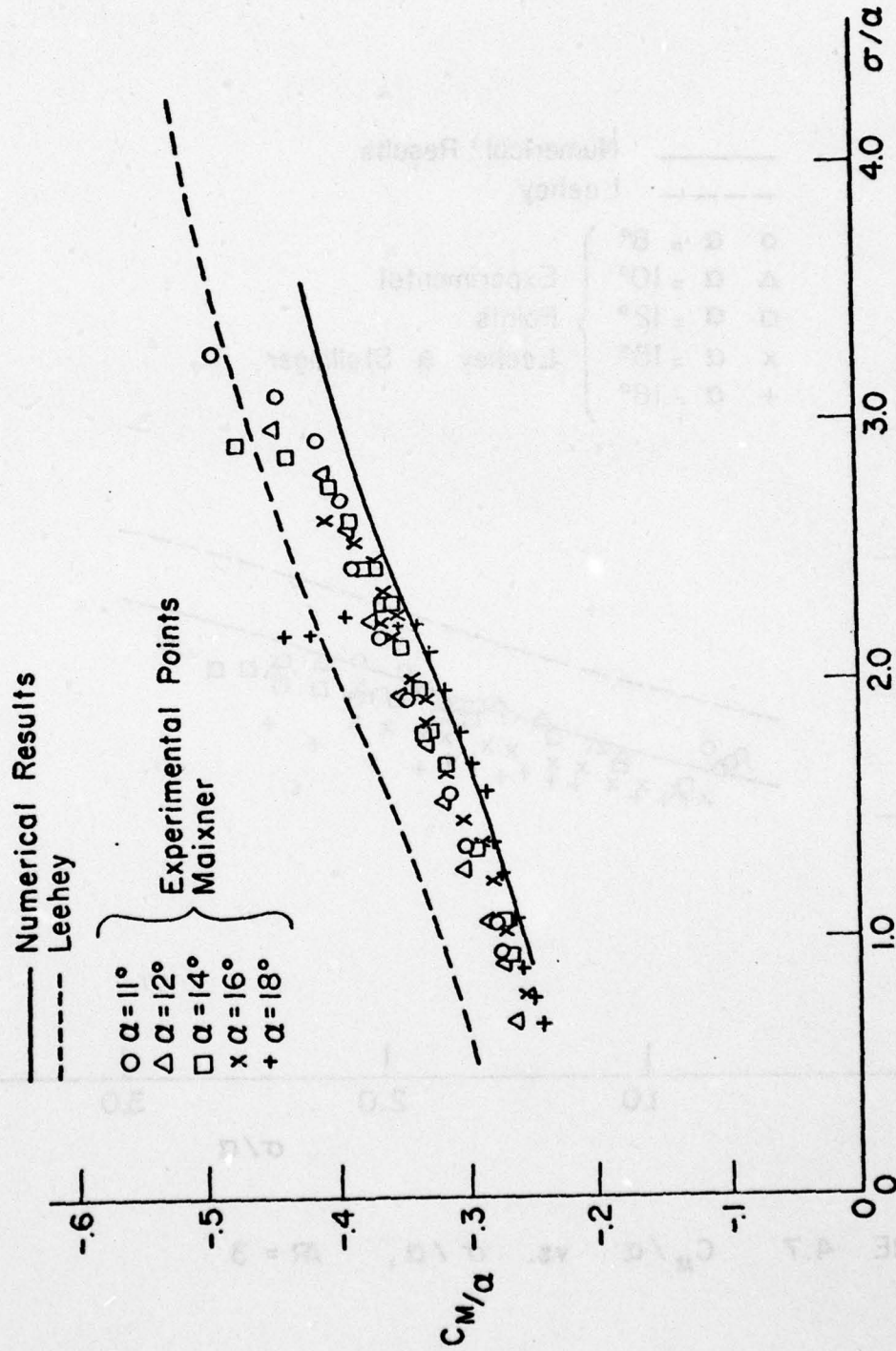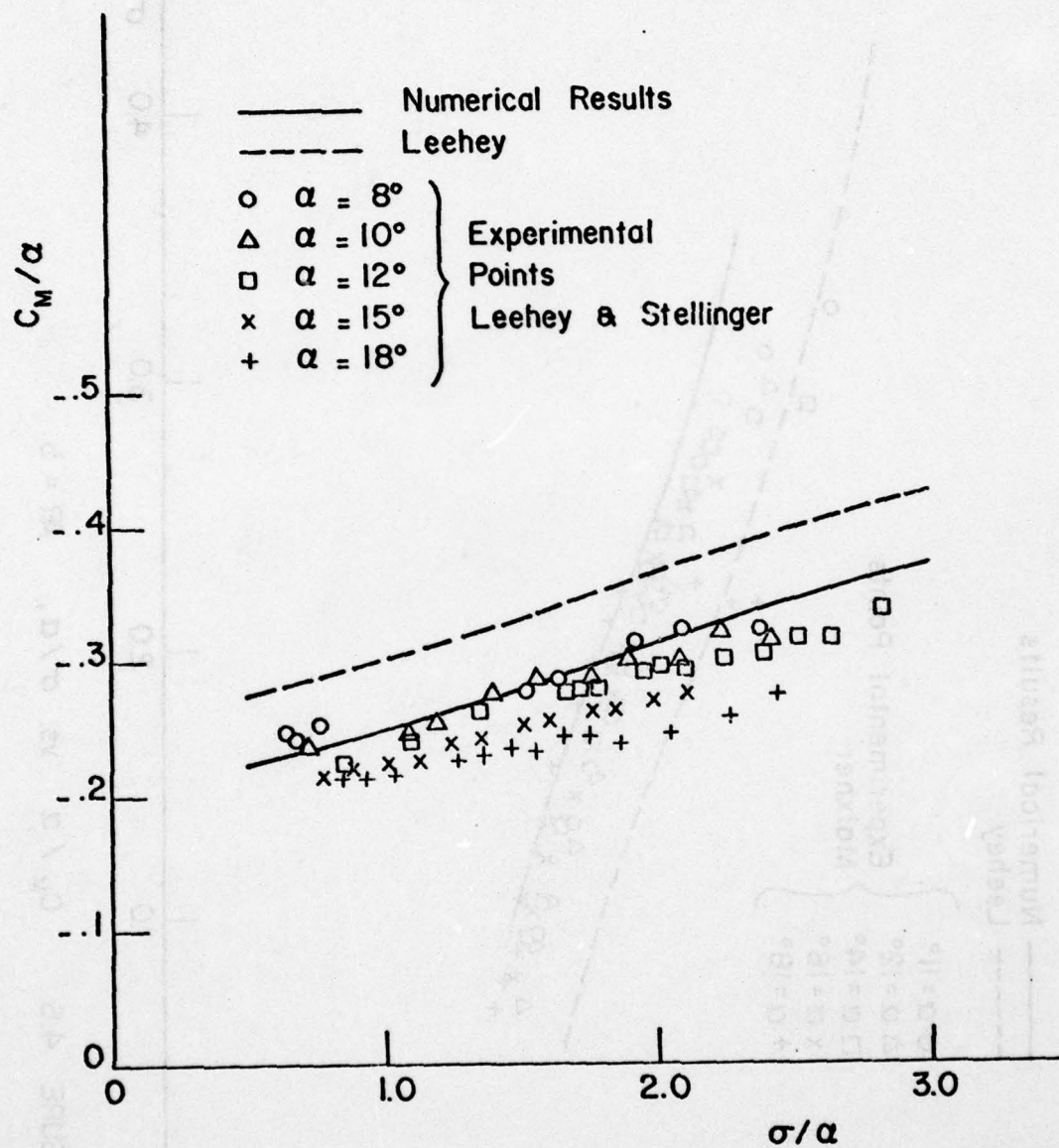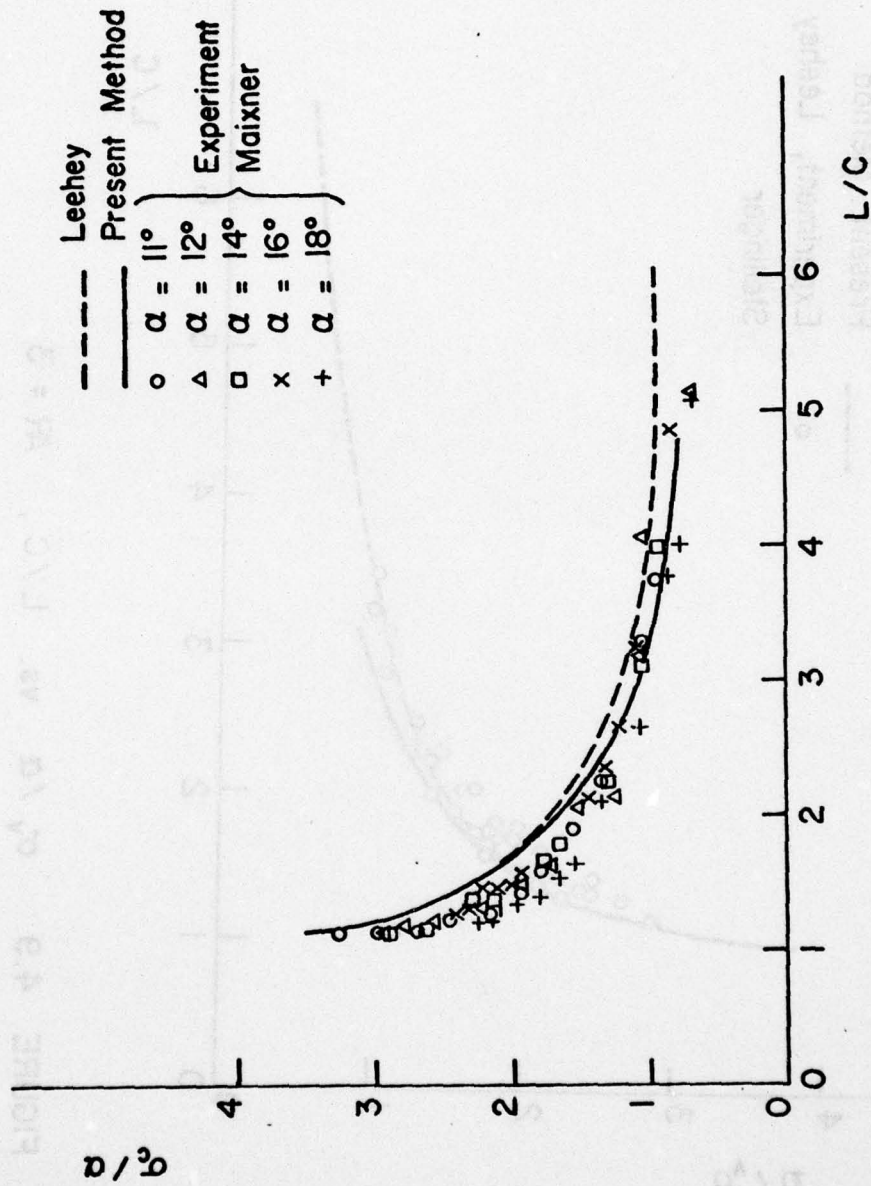
FIGURE 4.8 σ_c / α vs. L/C, AR = 5
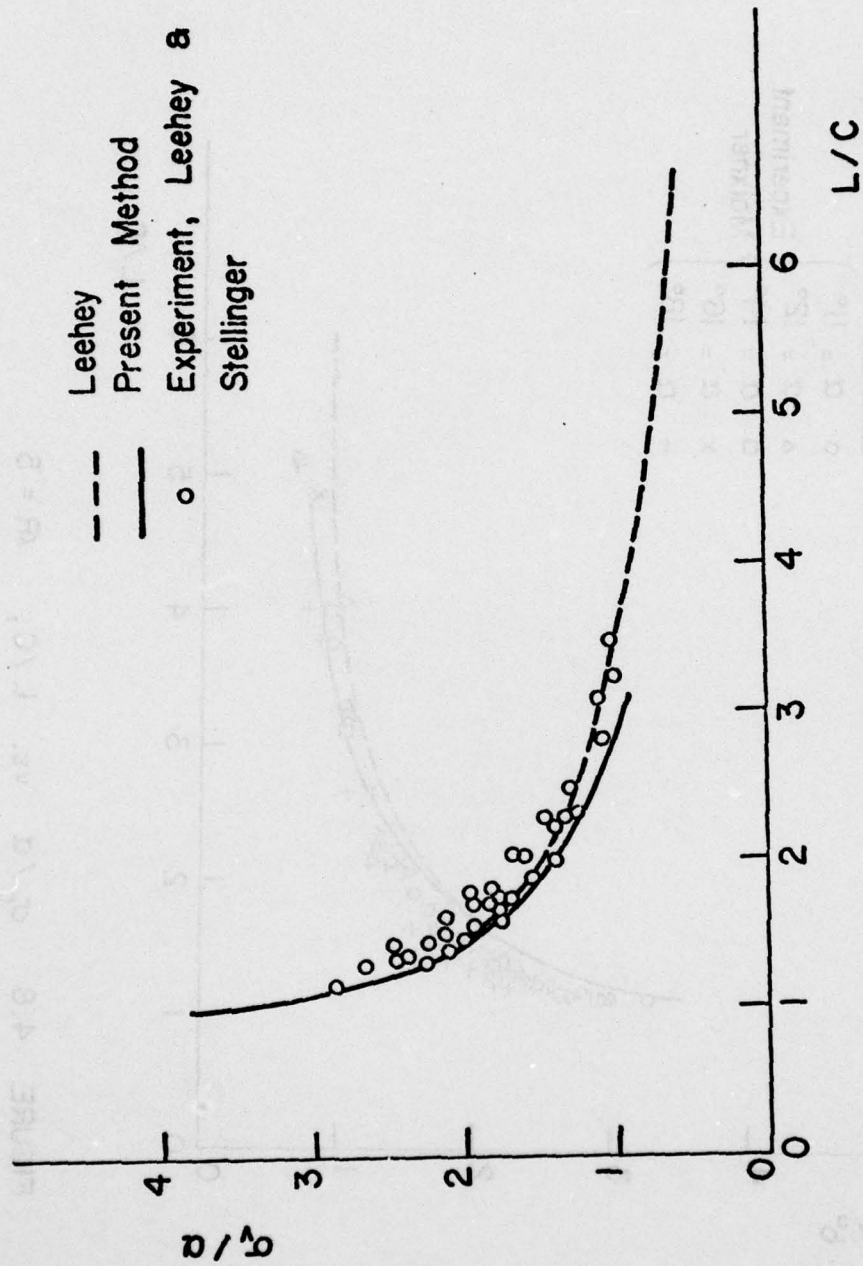
FIGURE 4.9 σ_v/α vs. L/C, AR = 3
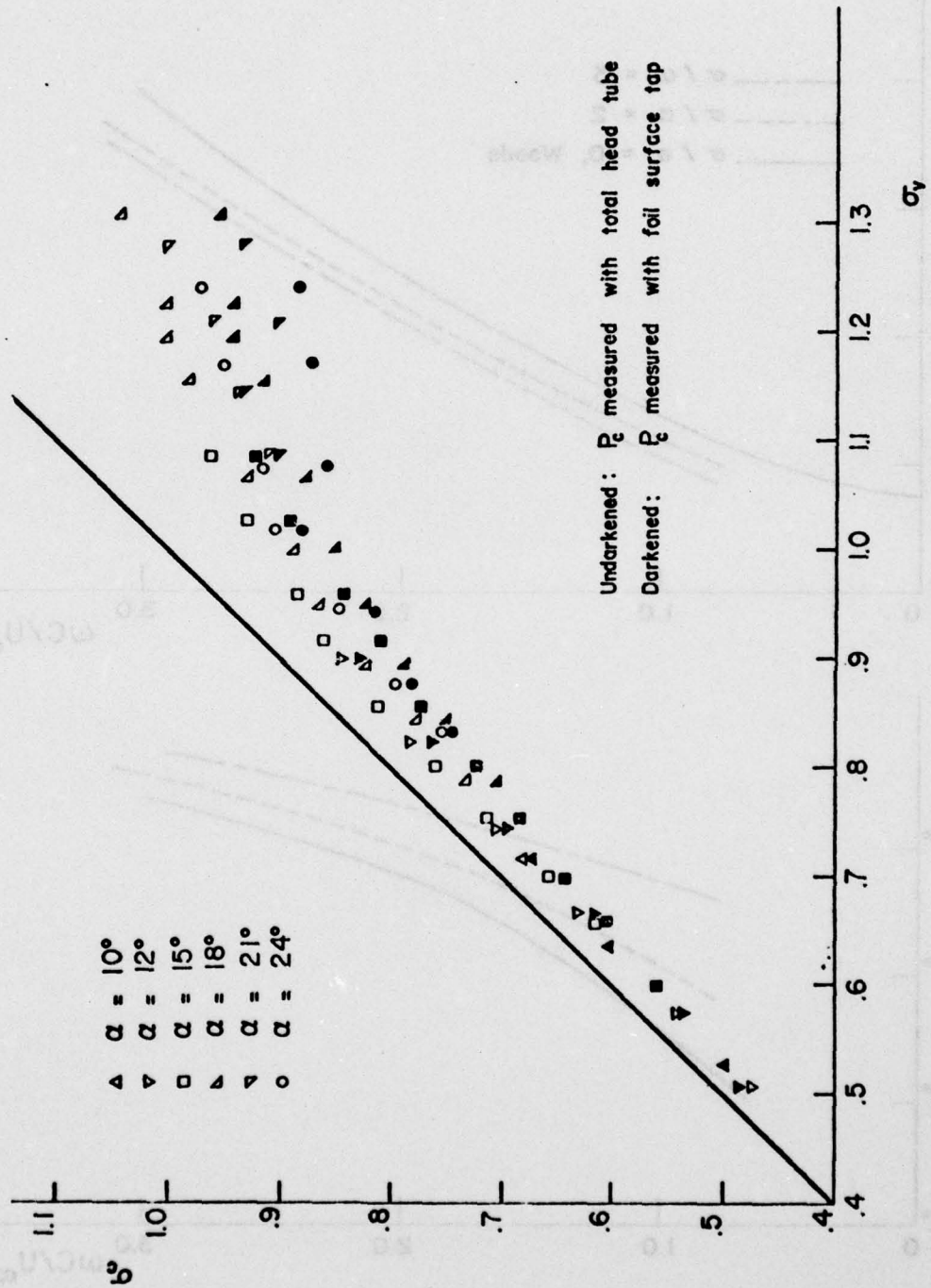
FIGURE 4.10 σ_c vs. σ_v
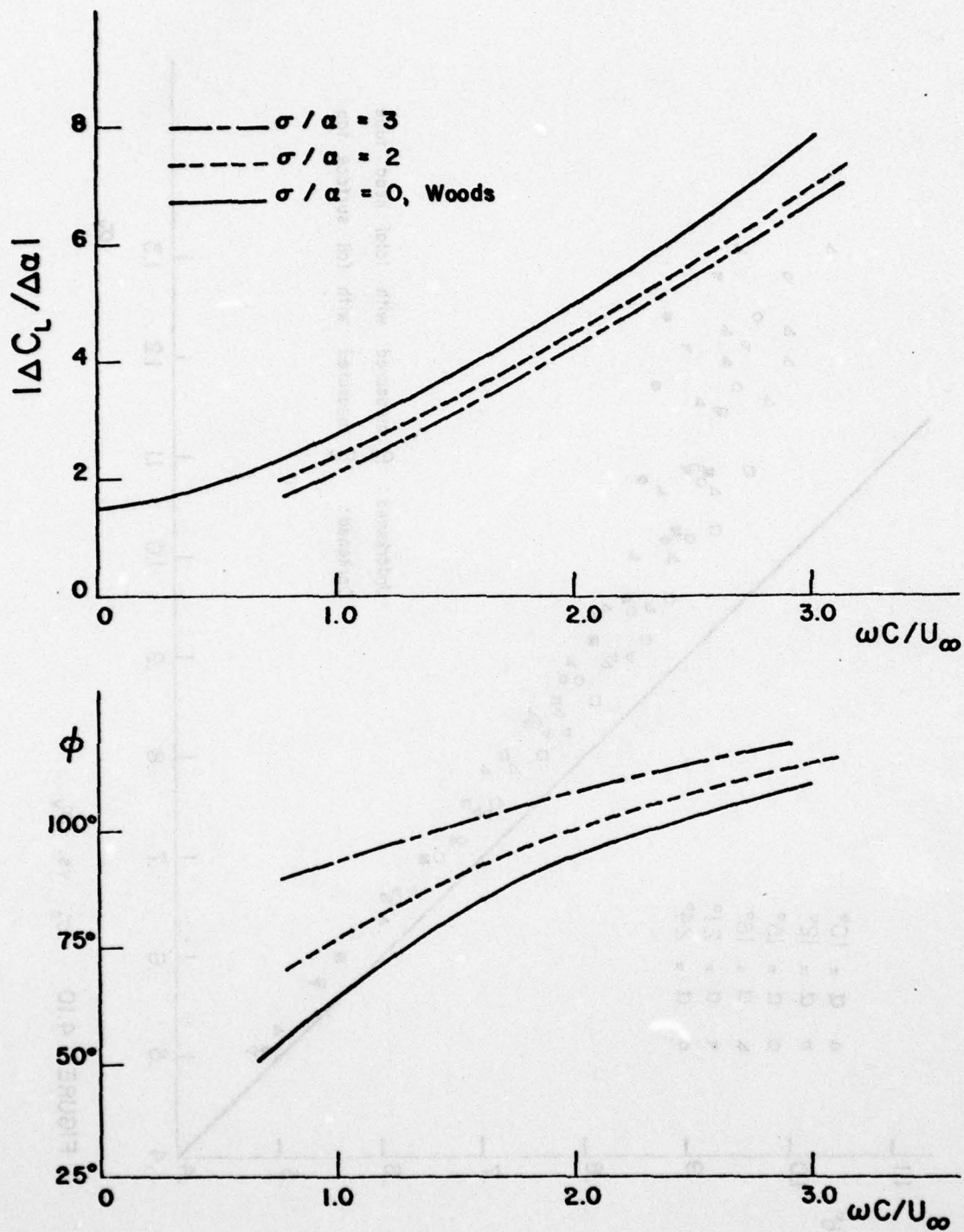
FIGURE 4.11 Lift Coefficient Due to Pitch for Two-dimensional Hydrofoil
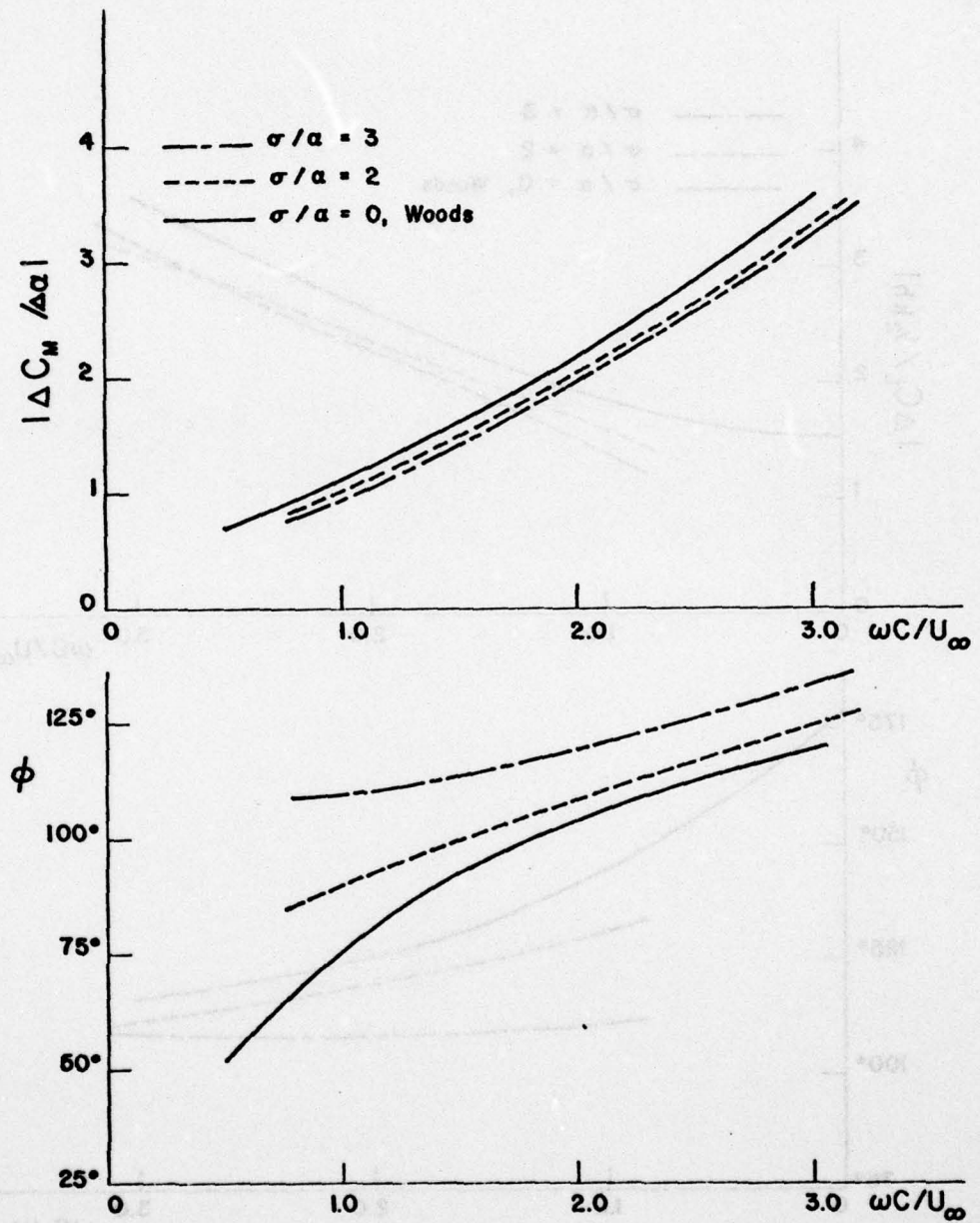
FIGURE 4.12   Moment Coefficient Due to Pitch for
Two-dimensional   Hydrofoil
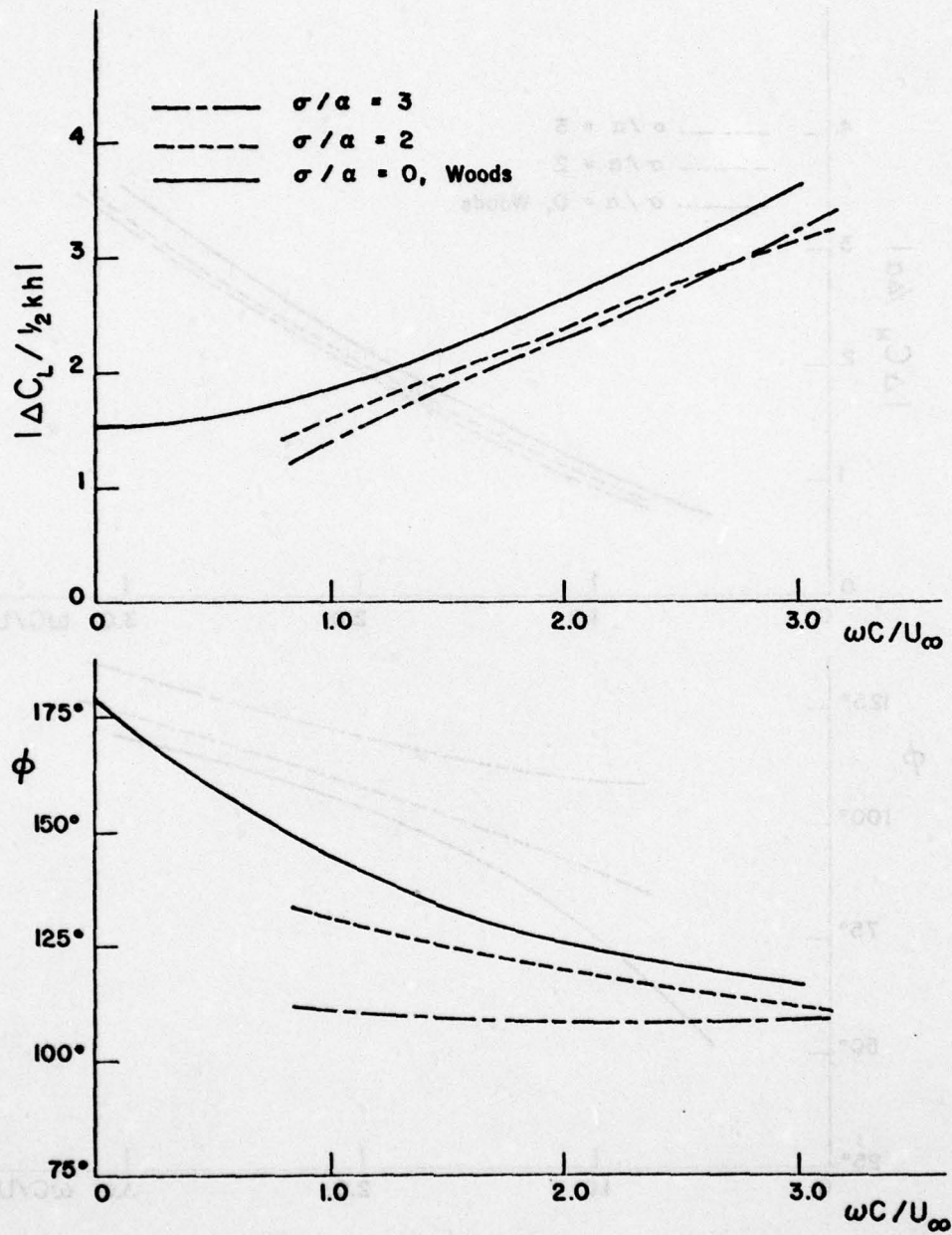
FIGURE 4.13 Lift Coefficient Due to Heave for Two-dimensional Hydrofoil
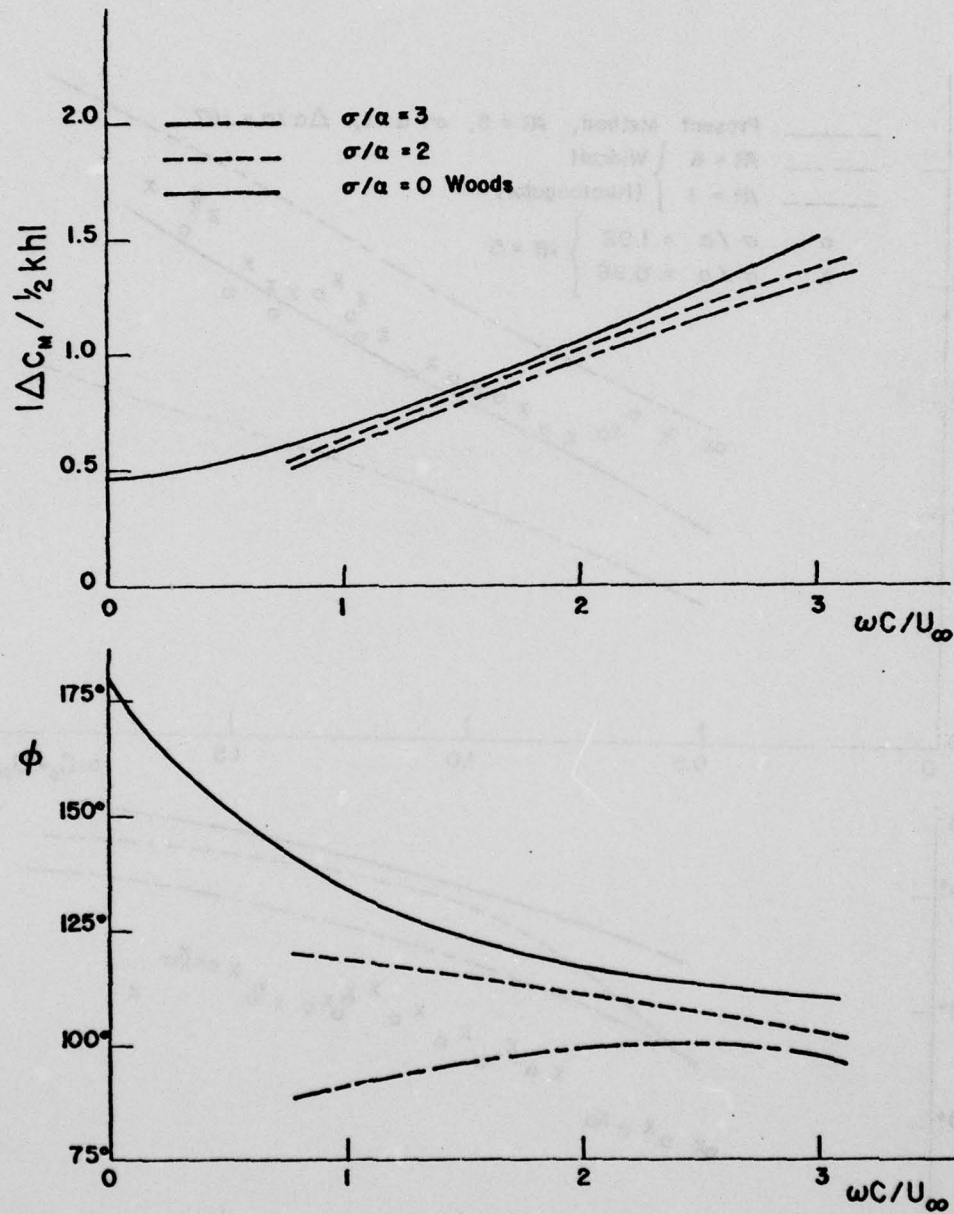
FIGURE 4.14   Moment Coefficient due to heave for two-dimensional
Hydrofoil
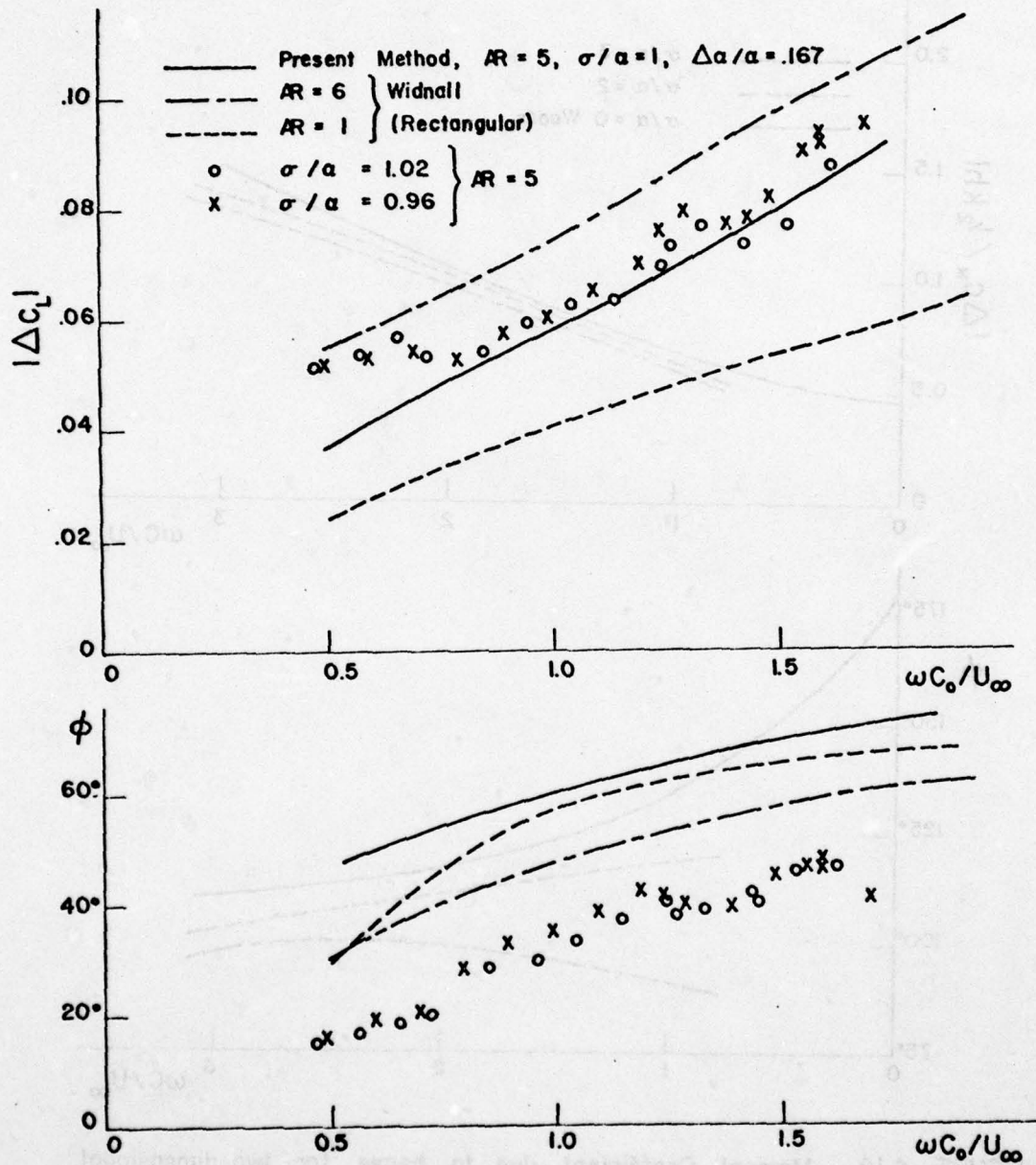
FIGURE 4.15   Oscillatory Lift Coefficient at long Cavities, $\Delta\alpha = \pm 2°$, AR = 5
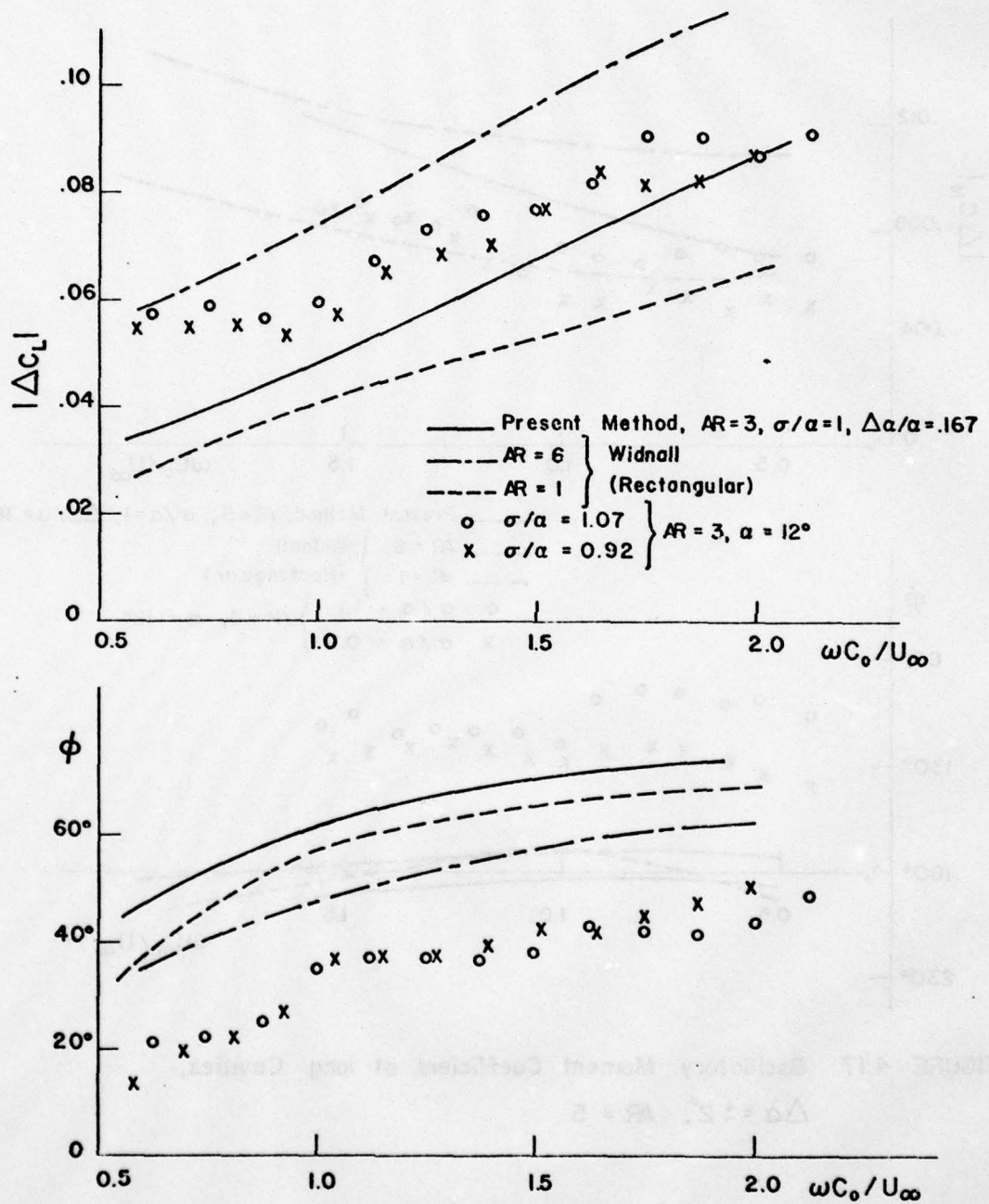
FIGURE 4.16   Oscillatory Lift Coefficient at long Cavities, $\triangle \alpha = \pm 2°$, $AR = 3$
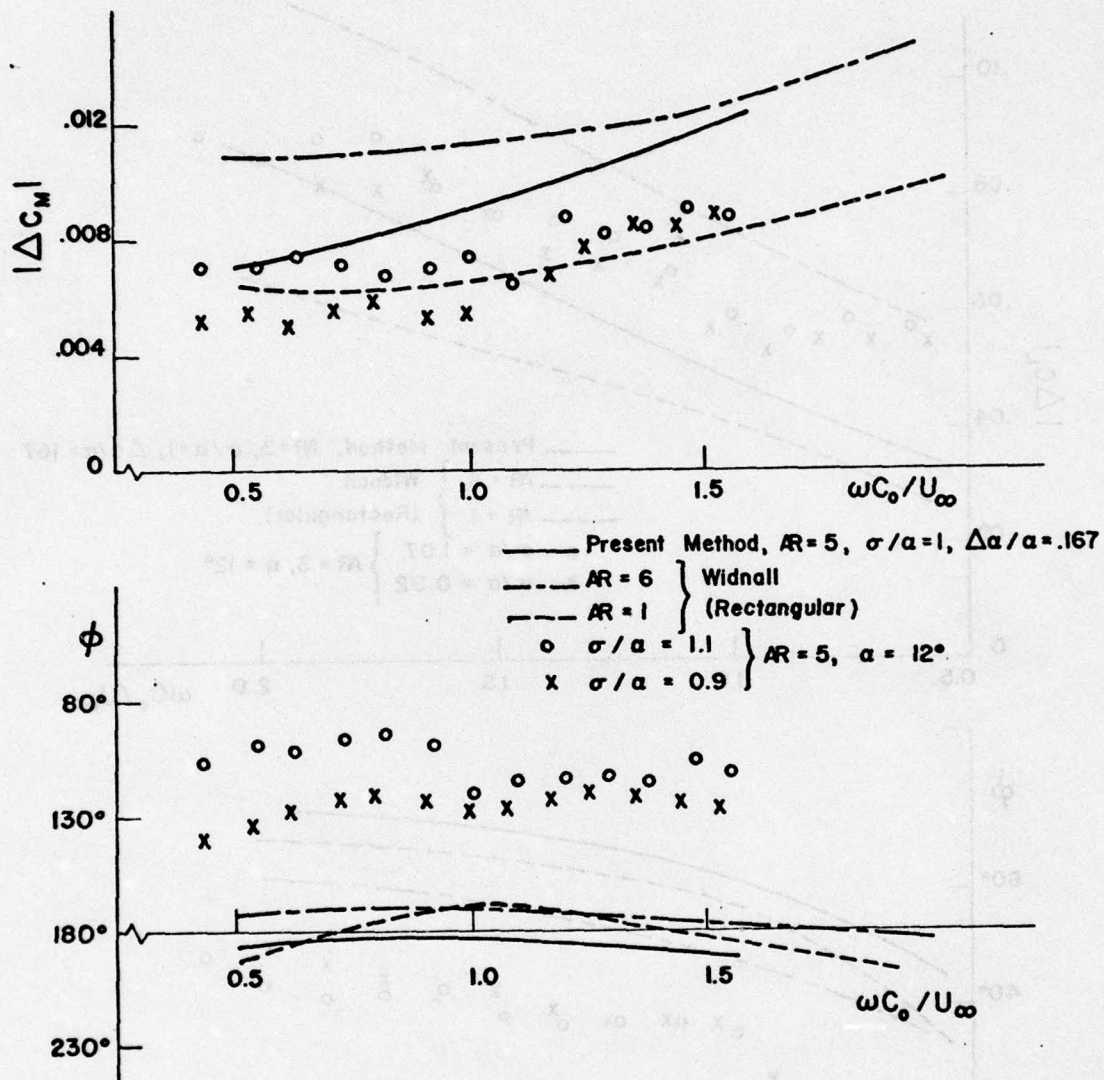
FIGURE 4.17   Oscillatory Moment Coefficient at long Cavities, $\Delta\alpha = \pm 2°$, AR = 5
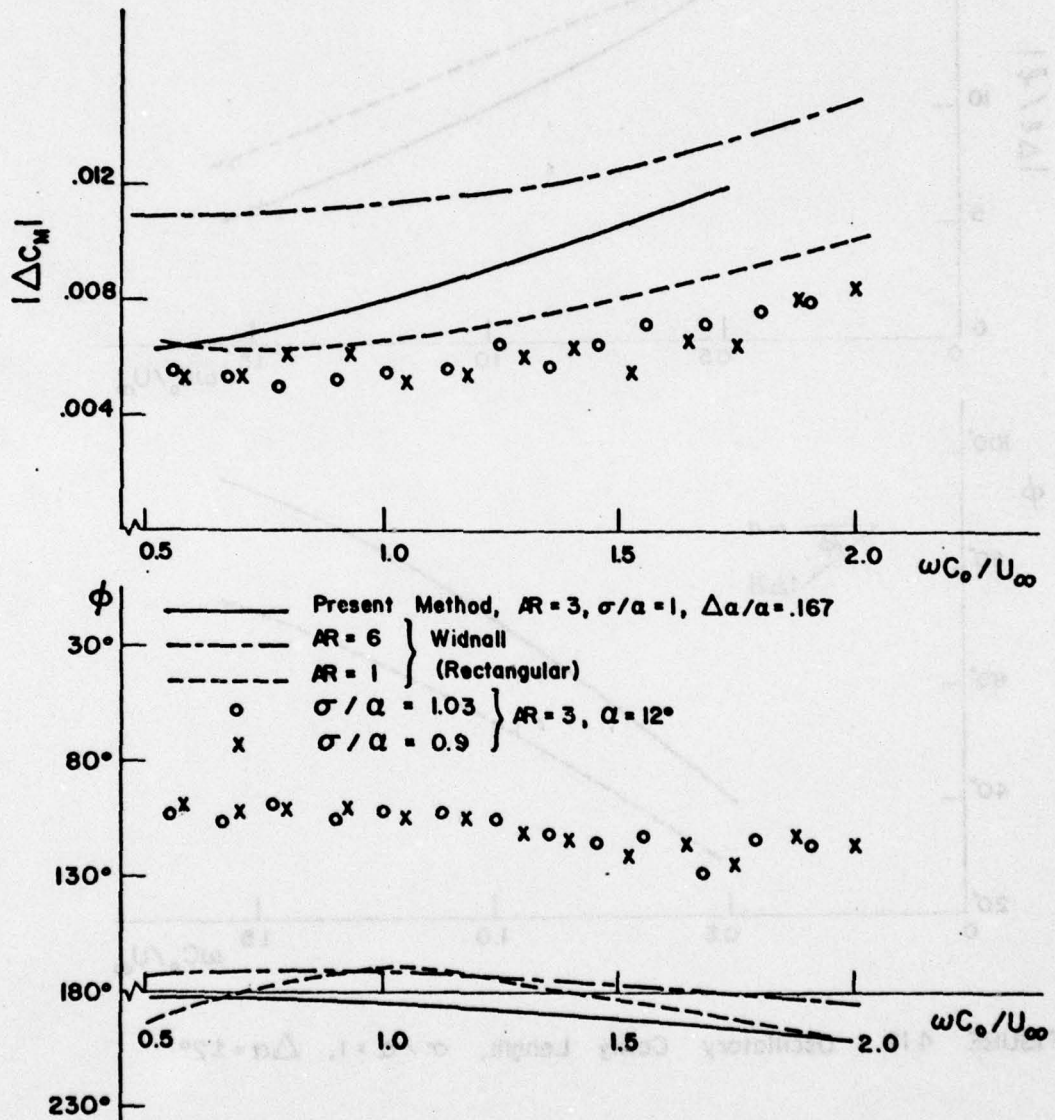
FIGURE 4.18   Oscillatory Moment at long Cavities, $\Delta\alpha = \pm 2°$;   AR = 3
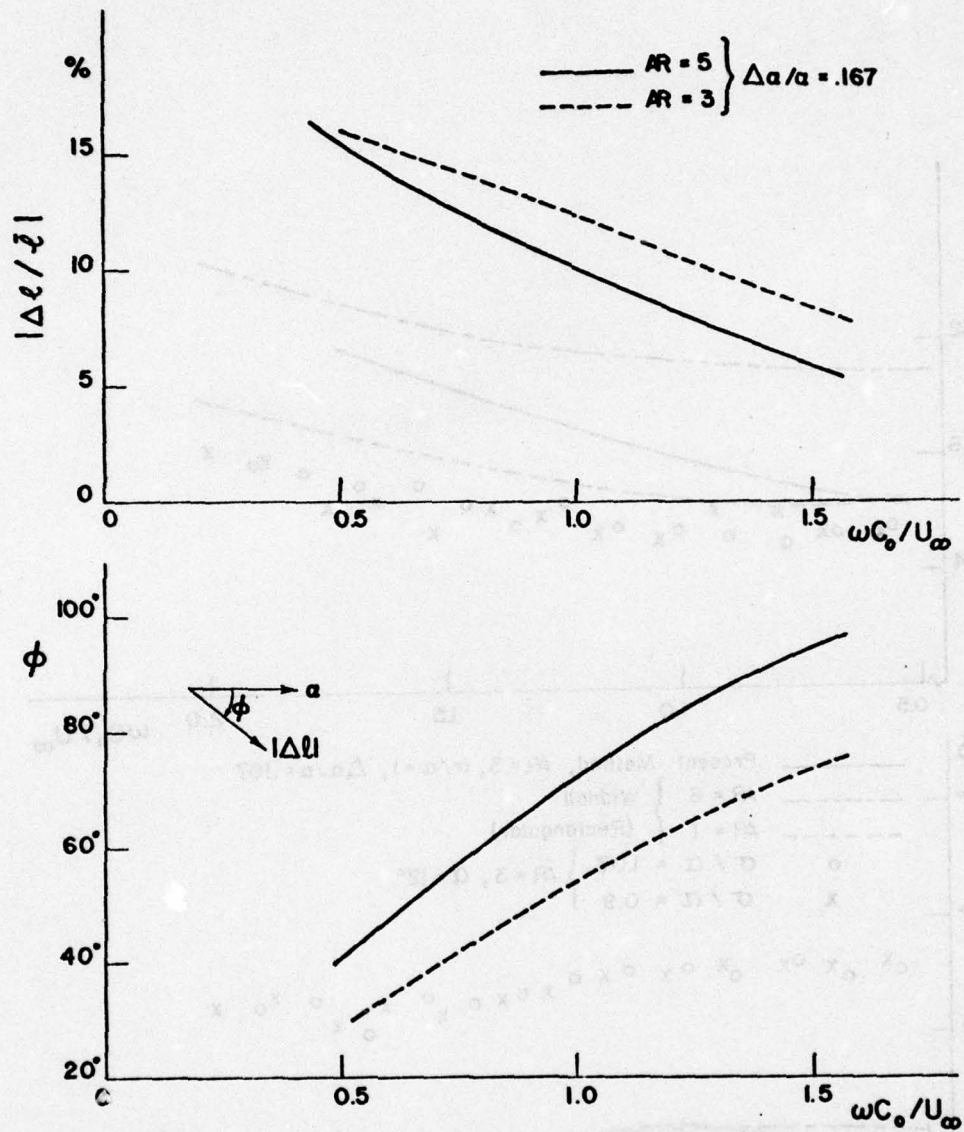
FIGURE 4.19 Oscillatory Cavity Length, $\sigma/\alpha = 1$, $\Delta\alpha = \pm 2°$
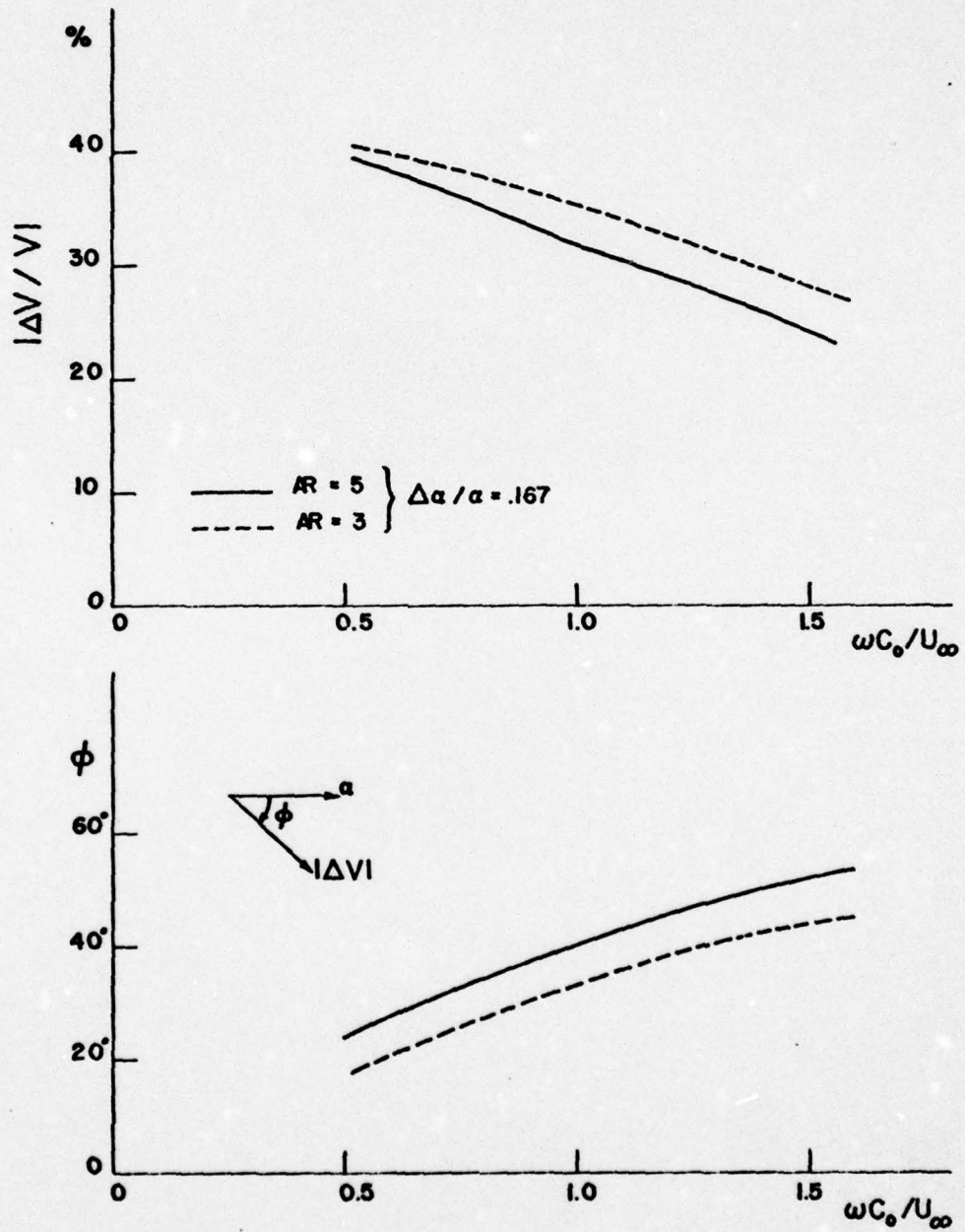
FIGURE 4.20 Oscillatory Cavity Volume, $\sigma/\alpha = 1$, $\Delta\alpha = \pm 2°$

APPENDIX A

DYNAMIC CALIBRATION OF DYNAMOMETER

Dynamic calibrations of the water tunnel force gages were carried out with the aspect ratio 5 foil. The following equipment was used to perform the calibration:

1) Vibration Exciter Body - Bruel & Kjaer Type 4801,

2) Vibration Exciter Head - Bruel & Kjaer Mode Study Head Type 4814,

3) Power Amplifier - Bruel & Kjaer Type 2707,

4) Impedance Head - Wilcoxon Z-602 #252,

5) Sweep Oscillator - Spectral Dynamics SD 104A-5,

6) Dynamic Analyzer - Spectral Dynamics SD 101-A,

7) Buffer Attenuator - Home Made,

8) Ithaco Preamplifier - Model 255-A,

9) Accelerometer - Bruel & Kjaer Type 4332 #159861,

10) Phase Meter - Spectral Dynamics SD 110,

11) Oscilloscope - Tektronix Type 561B,

12) RMS Voltmeter - Bruel & Kjaer Type 2416,

13) DC Voltmeter - HP Type 405 CR,

14) Transducer Digital Indicator - Lebow Model 7521.

The instrumentation arrangement is shown schematic-ally in Fig. A.1

The dynamometer, installed in the water tunnel, was

subjected to a sinusoidally oscillating force, generated
from B & K Exciter Head Type 4814. The exciter was mounted
on a heavy table and was also fixed to the side flange of
the tunnel. The stiffness in the connections between the
exciter and the flange of the tunnel was sufficiently high
that the resonance frequency was out of the range of interest.
A pushrod was used to transfer the force from exciter head
to the pressure center of the foil: an impedance head was
attached between them. Figure A.2 shows a picture of the
exciter arrangement. The exciter was driven by the
Oscillator and B & K Power Amplifier, which is a high power,
low distortion vibration exciter driver, giving a highly
linear output and a selectable output impedance.

The force signals from the load cells and the impedance
head were analyzed with the Spectral Dynamics Analyzer, in
which a 5 Hz filter was used. The signal being analyzed
was compared internally to a signal of the same frequency
as the exciting frequency from the oscillator and filtered
with the 5 Hz Band Pass filter around that frequency. The
measurement covered the range from 5 Hz up to 30 Hz. Due
to problems of stabilization of the shaker output, the tests
were carried out for discrete frequencies.

The phase angle between the force outputs of the load
cell and the impedance head was measured. Both of these
signals come through the Spectral Dynamics Analyzer and were
compared in the Phase Meter. The three load cells on the

steel rods that sustain the floating section of the
dynamometer were replaced by dummy load cells to increase
the stiffness.

The dynamic calibration of the torque transducer was
the most difficult calibration made. It was hard to calibrate
the moment gage under the same conditions that the unsteady
measurements were made. During the calibration, the top
part of the torque transducer was rigidly clamped to the base
of the dynamometer and the top window of the tunnel. The
moment input was obtained from the force on the impedance
head multiplied by the moment arm. The output of the torque
transducer was obtained from the Lebow Indicator. The
calibration showed that the moment from torque transducer
had a linear relation to the applied moment.

The dynamic system of the dynamometer in lift and drag
directions can be described by a model of three degrees of
freedom. The applicable equations of motion are

$$m_1 \ddot{x}_1 + k_1(x_1 - x_3) + k_2(x_1 - x_2) + C_1(\dot{x}_1 - \dot{x}_3) + C_2(x_1 - \dot{x}_2) = 0,$$

$$m_2 \ddot{x}_2 + k_2(x_2 - x_1) + C_2(\dot{x}_2 - \dot{x}_1) = F_0 e^{j\omega t},$$

$$m_3 \ddot{x}_3 + k_3 x_3 + k_1(x_3 - x_1) + C_3 \dot{x}_3 + C_1(\dot{x}_3 - \dot{x}_1) = 0,$$

$$(A-1)$$
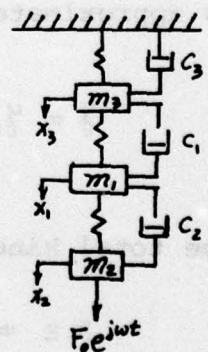
where

m_3 = mass of the base of the dynamometer
and top window of the tunnel,

m_1 = mass of the floating part of the dynamometer
and 23% of the shaft mass,

m_2 = mass of the foil and 77% of the shaft mass,

k_3, c_3 = spring constant and damping coefficient
in the tunnel's window, respectively,

k_1, c_1 = spring constant and damping coeffieient of
the load cell plus the linkage between the
load cell and the dynamometer, respectively,

k_2, c_2 = spring constant and damping coeffieient of
the shaft and foil combination, respectively,

The shaft mass was divided as described in Den Hartog (1956) and based on Rayleigh's method.

A contilever beam EI, of length ℓ and mass m carries a concentrated mass M at its end. The deformation of the beam is approximated by a quarter cosine

$$y = y_0 \left(1 - \cos \frac{\pi x}{2\ell}\right).$$
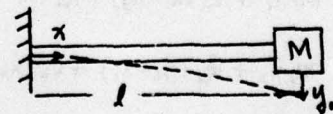
The total kinetic energy can be written as

$$K.E. = \frac{1}{2} \omega^2 y_0^2 (M + 0.23 m).$$

The potential energy will be

$$K.E. = \frac{1}{2} \omega^2 y_0^2 (M + 0.23m).$$

Equating the kinetic energy to the potential energy and solving for ω^2 , we find

$$\omega^2 = \frac{3.03\, EI}{l^3 (M + 0.23m)}.$$

Thus 23 percent of the mass of the beam is effectively added to the end mass.

Equations (A-1) can be solved by assuming harmonic motion for the displacements. The ratio of Lebow force to exciter force can be obtained after the spring constants and masses are known. The value of these constants are:

Mass of the base of dynamometer and top window of

the tunnel

$m_3 = 10$ slug,

Mass of the floating section of dynamometer =

$m_f = 1.2$ slug,

Mass of the shaft

$m_s = 1.37$ $lb_m = 0.043$ slug,

Mass of the floating part of the dynamometer and

a fraction of the shaft mass

$m_1 = m_f + 0.77\, m_s = 1.2 + 0.043 \times 0.76 =$

1.23 slug,

Mass of the hydrofoil

$$m_h = 0.157 \text{ slug},$$

Mass of the foil and a fraction of the shaft mass

$$m_2 = m_h + 0.23 \times m_s = 0.168 \text{ slug}.$$

The load cells are coupled between the floating part and the base of the dynamometer by screw rods and bolts. The spring constant of the load cells was obtained from the Lebow catalog. The spring constant of the rods are calculated from Hooke's law, neglecting the Poisson effect. The equaivalent spring constant of the lift load cell system (#125) is

$$k_1 = 66440 \text{ lb/in.}$$

The spring constant of the base dynamometer and top window combination, k_3, was obtained from the experimental force-displacement curve. This work was done by W. T. Tan as part of UROP project. This constant is

$$k_3 = 299,000 \text{ lb/in.}$$

Spring constant of the shaft and foil is (Riva (1974))

$$k_2 = 25,000 \text{ lb/in.}$$

Damping is small in this mechanical system. 1% of the individual critical damping of each spring-mass system is

$$c_1 = 1.65 \ lb_f\text{-sec/in},$$
$$c_2 = 0.375 \ lb_f \ \text{sec/in},$$
$$c_3 = 10 \ \ \ lb_f \ \text{sec/in}.$$

From the calibration, it is evident that the natural frequency of the dynamometer is above the test range. The results show that it is reasonable to represent the real system by the model with three degrees of freedom. It also shows that the damping is small in the system and the dynamometer can be modeled as a mass-spring only. The lowest natural frequency of the dynamometer with foil a attached was about 80 Hz. The maximum frequency of the pitching oscillation was about 20 Hz. The mass of the foil system and of portions of the dynamometer produced a force on the load cells when the apparatus was oscillated. The magnitude of the force was determined by oscillating the foil in air and measuring the resulting force. This force was subtracted from the response of the supercavitating foil, taking into consideration the phase relationship between the two forces.

The torsional system can be represented by a model with two degrees of freedom. Equations of motion are

$$J_1 \frac{d^2\psi_1}{dt^2} + c_4 \frac{d\psi_1}{dt} + k_5(\psi_1 - \psi_2) + k_4\psi_1 = M_1,$$

$$J_2 \frac{d^2\psi_2}{dt^2} + k_5(\psi_2 - \psi_1) = M_2,$$

$$(A-2)$$
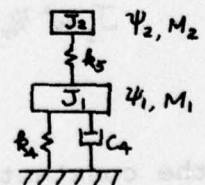
where J_1 and J_2 are the moment of inertia of the foil and shaft combination and crankarm respectively; M_1 and M_2 are the moment applied at the foil and crankarm, respectively; c_4 and k_4 are the damping coefficient and torsional spring constant due to the bearing and rubber sealing. The moment meausred from the torque trandsucer will be

$$M_t = k_5 (\psi_2 - \psi_1).$$

Substituting this into the last set of equations. Using the assumption of simple harmonic motion and $\ddot{\psi}_1 \simeq \ddot{\psi}_2$, these equations become

$$J_1 \omega^2 \psi_{10} e^{j\omega t} + c_4 \omega \psi_{10} e^{j(\omega t - \frac{\pi}{2})} - M_{t_0} e^{j(\omega t - \phi_1)}$$
$$+ k_4 \psi_{20} e^{j(\omega t - \pi)} = M_{10} e^{j(\omega t - \phi_2)},$$
$$J_2 \omega^2 \psi_{10} e^{j\omega t} + M_{t_0} e^{j(\omega t - \phi_1)} = M_{20} e^{j(\omega t - \phi_3)}, \qquad (A-3)$$

where the phase angles ϕ_1, ϕ_2, ϕ_3 , are relative to the acceleration. These equations can be simplified as

$$J_1 \omega^2 \psi_{10} + c_4 \omega \psi_{10} e^{-j\frac{\pi}{2}} - M_{t_0} e^{-j\phi_1} + k_4 \psi_{10} e^{-j\pi} = M_{10} e^{-j\phi_2},$$
$$J_2 \omega^2 \psi_{10} + M_{t_0} e^{-j\phi_1} = M_{20} e^{-j\phi_3}. \qquad (A-4)$$

If the constants J_1, c_4 and k_4 are known, then the moment applied at the foil M_1 can be calculated from the equation (A-4) after the torque transducer output M_t is measured.

When the foil was oscillating in the air, the moment applied to the foil, M_1 was zero. The equations of motion become

$$J_1 \frac{d^2 \psi_1}{dt^2} + C_4 \frac{d\psi_1}{dt} - M_t + k_4 \psi_1 = 0,$$

$$J_2 \frac{d^2 \psi_2}{dt^2} + M_t = M_2. \qquad (A-5)$$

The moment M_2 was measured by the force at the load cell in the drag direction multiplied by the length of the crankarm. M_t was measured by the torque transducer. The phase relationship was measured with respect to the acceleration. These equations can determine the characteristic constants of the system. The results of the calibration show the damping coefficient to be dependent on the frequency. For the aspect ratio 3 hydrofoil, these constants are

$$J_1 = 0.0024 \qquad \text{ft-lb-sec}^2,$$

$$J_2 = 0.0033 \qquad \text{ft-lb-sec}^2,$$

$$C_4 = 0.06365 + 9.92/f^2 - 28.6/f^3 \qquad \text{ft-lb-sec},$$

$$k_4 = 4.63 \quad \text{ft-lb}. \qquad (A-6)$$

From the results of the calibration, it is reasonable to represent the torsional system by a model with two degrees of freedom.

Lebow Indicator

Dynamometer — Lift, Drag, Moment

Ithaco Amplifier Unfiltered

Impedance Head

Buffer Amplifier

Exciter

Dynamic Analyzer

Dynamic Analyzer

Tuning

Tuning

Power Amplifier

Phase Meter

DC Voltmeter — DC Filtered

Frequency Counter
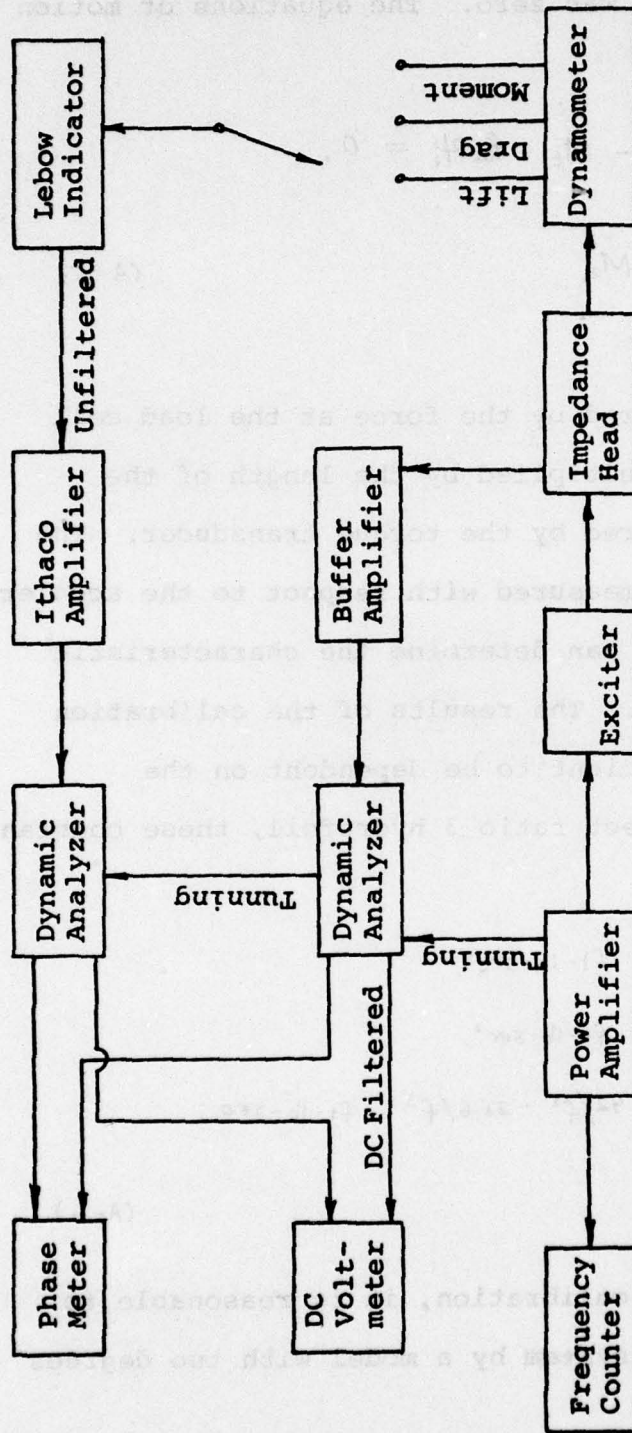
Figure A.1 Instrumation Arrangement for Calibration

APPENDIX B

FORMULATION OF PROBLEM

In the following, the isentropic inviscid flow of a incompressible, initially irrotational fluid is considered for linearized supercavitating hydrofoils. Under this hypothesis, the flow can be described by the velocity potential Φ . The linear equation of the velocity potential exterior to the foil plus the cavity plus the vortex sheet is

$$\nabla^2 \Phi = 0, \qquad\qquad (B-1)$$

where ∇^2 is the Laplacian operator. It is convenient to introduce the perturbation potential φ , such that

$$\Phi = U_\infty x + \varphi, \qquad\qquad (B-2)$$

where U_∞ is the undisturbed flow velocity in the direction of the positive x-axis. Combining equations (B-1) and (B-2) yeilds the equation for the perturbation potential

$$\nabla^2 \varphi = 0. \qquad\qquad (B-3)$$

The linearized Bernoulli equation for unsteady flow is

$$P - P_\infty = -\rho \left(\frac{\partial \varphi}{\partial t} + U_\infty \frac{\partial \varphi}{\partial x} \right), \qquad\qquad (B-4)$$

which yields, for the pressure coefficient

$$P \equiv \frac{P - P_\infty}{\frac{1}{2}\rho U_\infty^2} = -\frac{2}{U_\infty} \left(\frac{1}{U_\infty} \frac{\partial \varphi}{\partial t} + \frac{\partial \varphi}{\partial x} \right). \qquad (B-5)$$

The perturbation pressure, P , also satisfies the Laplace equation

$$\nabla^2 P = 0, \qquad\qquad (B-6)$$

exterior to the foil plus the cavity plus the vortex sheet.
Let the source distribution, $f(x,\zeta,t)$, represent the slope
difference between the upper and lower surface at point $(x,0,\zeta)$,
and the vortex distribution, $\gamma_a(x,\zeta,t)$ represent the
difference in the x-component of perturbation velocity between
the upper and lower surface at point $(x,0,\zeta)$.   As shown
in Fig. B-1, this leads to the results,

$$f(x,\zeta,t) \equiv \frac{v(x,+0,\zeta,t)}{U_\infty} - \frac{v(x,-0,\zeta,t)}{U_\infty} \equiv \left\langle \frac{v(x,\zeta,t)}{U_\infty} \right\rangle, \qquad (B-7)$$

$$\gamma_a(x,\zeta,t) \equiv \frac{u(x,-0,\zeta,t)}{U_\infty} - \frac{u(x,+0,\zeta,t)}{U_\infty} \equiv \left\langle \frac{u(x,\zeta,t)}{U_\infty} \right\rangle, \qquad (B-8)$$

where $\langle a \rangle$ denotes the jump in "a" across the surface $y=0$.

From the Bernoulli equation (B-5) and the distributions
of sources and vortices, one can see that

$$\left\langle \frac{\partial P}{\partial y} \right\rangle = -\frac{2}{U_\infty}\left(\frac{1}{U_\infty}\frac{\partial}{\partial t}\left\langle \frac{\partial \varphi}{\partial y}\right\rangle + \frac{\partial}{\partial x}\left\langle \frac{\partial \varphi}{\partial y}\right\rangle\right)$$

$$= -2\left(\frac{1}{U_\infty}\frac{\partial}{\partial t}\left\langle \frac{v}{U_\infty}\right\rangle + \frac{\partial}{\partial x}\left\langle \frac{v}{U_\infty}\right\rangle\right)$$

$$= -2\left(\frac{1}{U_\infty}\frac{\partial f}{\partial t} + \frac{\partial f}{\partial x}\right), \qquad (B-9)$$

$$\langle P \rangle = -\frac{2}{U_\infty}\left(\frac{1}{U_\infty}\frac{\partial}{\partial t}\langle \varphi\rangle + \left\langle \frac{\partial \varphi}{\partial x}\right\rangle\right)$$

$$= -2\left(\frac{1}{U_\infty}\frac{\partial}{\partial t}\int_{-\infty}^{x}\left\langle \frac{u}{U_\infty}\right\rangle d\xi + \left\langle \frac{u}{U_\infty}\right\rangle\right)$$

$$= \frac{2}{U_\infty}\frac{\partial}{\partial t}\int_{-\infty}^{x}\gamma_a\, d\xi + 2\gamma_a. \qquad (B-10)$$

For the application of Green's theorem to the super-cavitating hydrofoil of finite span, the pressure at the point (x, y, z) is (e.g. Newman (1977))

$$P(x,y,z,t) = \frac{1}{4\pi} \oint\!\!\!\oint \left(P(\xi,\eta,\zeta,t)\frac{\partial}{\partial n}\frac{1}{r} - \frac{\partial P(\xi,\eta,\zeta,t)}{\partial n}\frac{1}{r} \right) dS, \quad (B-11)$$

where r is the distance between (x, y, z) and dummy point (ξ, η, ζ), and S encompasses cavity, foil and wake.

The integral can be linearized for application to thin wings at small angles of attack and rewritten as open-surface integral

$$P(x,y,z,t) = \frac{1}{4\pi} \iint_{S_a+S_c} \left(\langle P \rangle \frac{\partial}{\partial \eta}\frac{1}{r} - \langle \frac{\partial P}{\partial \eta} \rangle \frac{1}{r} \right)_{\eta=0} dS, \quad (B-12)$$

where S_a is the projection of the foil surface on to the xz pland and S_c is the projection of cavity surface on to the same plane.

The partial derivative, $\frac{\partial}{\partial \eta}\frac{1}{r}$, is equal to zero everywhere on the plane $y=0$ except at the point $r=0$. If we assume the pressure distribution is continuous over the surface, then the limiting case for $r=0$ can be solved as in the following,

$$A(x,y,z,t) \equiv \iint \langle P \rangle \frac{\partial}{\partial \eta}\frac{1}{r}\Big|_{\eta=0} dS = \langle P(x,z,t) \rangle \iint \frac{\partial}{\partial \eta}\frac{1}{r}\Big|_{\eta=0} dS$$

$$= \langle P(x,z,t) \rangle \int_{z-\epsilon}^{z+\epsilon}\int_{x-\epsilon}^{x+\epsilon} \frac{y\, dS}{[(x-\xi)^2 + y^2 + (z-\zeta)^2]^{3/2}}. \quad (B-13)$$

If the point is on the surface $y = 0$, by introducing temporary integration variables $\xi' = (x-\xi)$, $\varsigma' = (\zeta-\varsigma)$, we find

$$A(x,0,\zeta,t) = \langle P(x,\zeta,t) \rangle \lim_{y \to 0} y \int_{-\epsilon}^{\epsilon}\int_{-\epsilon}^{\epsilon} \frac{d\xi' d\varsigma'}{(\xi'^2 + y^2 + \varsigma'^2)^{3/2}}$$

$$= \langle P(x,\zeta,t) \rangle \lim_{y \to 0} \left[2 \tan^{-1}\left(\frac{\epsilon^2}{y\sqrt{2\epsilon^2+y^2}} \right) \right.$$

$$\left. - 2 \tan^{-1}\left(\frac{-\epsilon^2}{y\sqrt{2\epsilon^2+y^2}} \right) \right]. \quad (B-14)$$

The limiting process involved here shows that we must let y and ϵ approach zero in such a way that the ratio ϵ/y becomes indifinitely large which leads to

$$A(x,0,\zeta,t) = 2\pi \langle P(x,\zeta,t) \rangle. \quad (B-15)$$

Substituting equations (B-9), (B-10) and (B-15) into Eq. (B-12), the pressure on the surface becomes

$$P(x,0,\zeta,t) = \frac{1}{2\pi} \iint_{S_a+S_c} \left(\frac{1}{U_\infty} \frac{\partial g(\xi,\varsigma,t)}{\partial t} + \frac{\partial g(\xi,\varsigma,t)}{\partial \xi} \right) \frac{1}{r} dS$$

$$+ \gamma_a(x,\zeta,t) + \frac{1}{U_\infty} \frac{\partial}{\partial t} \int_{-\infty}^{x} \gamma_a(\xi,\zeta,t) d\xi. \quad (B-16)$$

The second term in the first integral can be integrated by parts

$$\iint \frac{\partial g(\xi,\varsigma,t)}{\partial \xi} \frac{d\xi d\varsigma}{\left[(x-\xi)^2 + y^2 + (\zeta-\varsigma)^2 \right]^{1/2}} =$$

$$- \iint g(\xi,\varsigma,t) \frac{(x-\xi)}{\left[(x-\xi)^2 + y^2 + (\zeta-\varsigma)^2 \right]^{3/2}} d\xi d\varsigma, \quad (B-17)$$

where we use the condition that the source distribution
is zero outside the cavity.

When the boundary condition of constant pressure
in the cavity is applied on the cavity surface, the follow-
ing result is obtained

$$\sigma \equiv \frac{P_\infty - P_c}{\frac{1}{2} \rho U_\infty^2} = -P(x,0,\zeta), \qquad (B\text{-}18)$$

By combining Eqs. (B-16), (B-17) and (B-18), the integral
equation becomes

$$\sigma = -\gamma_a(x,\zeta,t) - \frac{1}{U_\infty} \frac{\partial}{\partial t} \int_{-\infty}^{x} \gamma_a(\xi,\zeta,t)d\xi$$

$$+ \frac{1}{2\pi} \iint_{S_a+S_c} \left[\frac{(x-\xi)\, g(\xi,\varsigma,t)}{r^3} - \frac{\partial g(\xi,\varsigma,t)}{U_\infty \partial t} \frac{1}{r} \right] dS. \qquad (B\text{-}19)$$

This integral equation can also be derived by using
the vortex potential, source potential and Bernoulli equation.

Applying the Green's theorem to the Laplace equation
$\nabla^2 \varphi = 0$, the velocity potential at an arbitary field
point (x,y,ζ) is

$$\varphi(x,y,\zeta,t) = \frac{1}{4\pi} \iint \left(\varphi \frac{\partial}{\partial n} \frac{1}{r} - \frac{\partial \varphi}{\partial n} \frac{1}{r} \right) dS. \qquad (B\text{-}20)$$

Again, the surface integral encompasses the cavity, foil
and wake. Since the operation of differentiation with
respect to x can be interchanged with ∇^2 in Eq. (B-3),
we may write

$$U(x,y,z,t) = \frac{1}{4\pi} \iint (U \frac{\partial}{\partial n} \frac{1}{r} - \frac{\partial u}{\partial n} \frac{1}{r}) dS. \qquad (B-21)$$

In regard to the second term in Eq. (B-21), the
condition of irrotationality reveals that

$$\frac{\partial u}{\partial n} = \frac{\partial u}{\partial y} = \frac{\partial v}{\partial x}, \qquad (B-22)$$

on top and

$$\frac{\partial u}{\partial n} = -\frac{\partial u}{\partial y} = -\frac{\partial v}{\partial x}, \qquad (B-23)$$

on the bottom surface. Eq. (B-20) can be rewritten as
open surface integral for linearized problem,

$$U(x,y,z,t) = \frac{1}{4\pi} \iint_{S_a+S_c} \left[\langle u \rangle \frac{\partial}{\partial n} \frac{1}{r} - \langle \frac{\partial u}{\partial n} \rangle \frac{1}{r} \right] dS$$

$$= \frac{1}{4\pi} \iint_{S_a+S_c} \left[-\gamma_a \frac{\partial}{\partial \eta} \frac{1}{r} - \langle \frac{\partial v}{\partial \xi} \rangle \frac{1}{r} \right] dS. \qquad (B-24)$$

From the relation $u = \partial \varphi / \partial x$ and $v = \partial \varphi / \partial y$

$$V(x,y,z,t) = \frac{\partial}{\partial y} \int_{-\infty}^{x} U(\xi,y,z,t) d\xi, \qquad (B-25)$$

where the assumption that $\mathcal{Y}(-\infty, y, \mathfrak{z}, t) = 0$ has been made without loss of generality. Inserting Eq. (B-25) into Eq. (B-24) and interchanging orders of differentiation and integration, we get

$$\mathcal{U}(x, y, \mathfrak{z}, t) = \frac{1}{4\pi} \iint \left[-\langle v \rangle \frac{\partial}{\partial y} \frac{1}{r} + \gamma_a(\xi, \mathsf{S}, t) \right.$$
$$\left. \times \frac{\partial^2}{\partial y^2} \int_{-\infty}^{x} \frac{d\xi'}{\left[(\xi' - \xi)^2 + y^2 + (\mathfrak{z} - \mathsf{S})^2 \right]^{1/2}} \right] d\xi d\mathsf{S}. \quad (B-26)$$

The integration of first term is zero everywhere on the plane $y = 0$ except at the point $r = 0$. The limiting value of this has been shown in Eq. (B-15). The result of the second term in the integral is the Mangler's principal value which is equal to (Ashley & Landall (1965))

$$\iint \frac{\gamma_a(\xi, \mathsf{S}, t)}{(\mathfrak{z} - \mathsf{S})^2} \left[1 + \frac{(x - \xi)}{((x - \xi)^2 + (\mathfrak{z} - \mathsf{S})^2)^{1/2}} \right] d\xi d\mathsf{S}. \quad (B-27)$$

By combining Eqs. (B-7), (B-15) and (B-27), the integral equation which satisfies the tangential velocity on the boundary becomes

$$\mathcal{U}(x, -0, \mathfrak{z}, t) = -\frac{1}{2} \mathfrak{z}(x, \mathfrak{z}, t) + \frac{1}{4\pi} \iint \frac{\gamma_a(\xi, \mathsf{S}, t)}{(\mathfrak{z} - \mathsf{S})^2}$$
$$\times \left[1 + \frac{(x - \xi)}{((x - \xi)^2 + (\mathfrak{z} - \mathsf{S})^2)^{1/2}} \right] d\xi d\mathsf{S}. \quad (B-28)$$

For the calculation of oscillatory forces and moments due to small amplitude oscillation about the steady state, the integral equations (B-19), (B-28) are solved for subject to the closure condition

$$\iint_{S_c} g(\xi, \varsigma, t) d\varsigma \, d\xi = 0. \qquad (B-29)$$

A Kutta condition is also required to make the problem well set.

The unknowns are the vortex strength, source strength and cavity surface.

As mentioned before, the cavitating lifting surface integral equations (B-19) and (B-28) can also be derived by using vortex and source potentials. A sheet of source spread continuously over the surface S_c, having strength $g(\xi, \varsigma, t)$ per unit area in the neighborhood of the point $(\xi, 0, \varsigma)$, possesses the perturbation potential

$$\varphi_s(x, y, \jmath) = -\frac{1}{4\pi} \iint_{S_c} \frac{g(\xi, \varsigma, t) d\xi d\varsigma}{[(x-\xi)^2 + y^2 + (\jmath-\varsigma)^2]^{\frac{1}{2}}}. \qquad (B-30)$$

The vertical velocity at point $(x, -0, \jmath)$ induced by the source sheet is

$$U(x,-0,\zeta,t) = \frac{\partial \varphi_s(x,-0,\zeta,t)}{\partial y}$$

$$= -\frac{1}{4\pi} \lim_{y \to -0} \frac{\partial}{\partial y} \iint_{S_c} \frac{g(\xi,\zeta,t)\,d\xi\,d\zeta}{[(x-\xi)^2 + y^2 + (\zeta-\zeta)^2]^{1/2}}$$

$$= \frac{1}{4\pi} \lim_{y \to -0} y \int_{\zeta-\epsilon}^{\zeta+\epsilon} \int_{x-\epsilon}^{x+\epsilon} \frac{g(\xi,\zeta,t)\,d\xi\,d\zeta}{[(x-\xi)^2 + y^2 + (\zeta-\zeta)^2]^{3/2}}$$

$$= -\frac{1}{2}\, g(x,\zeta,t). \qquad (B\text{-}31)$$

The pressure at point $(x,+0,\zeta)$ induced by the source sheet can be calculated from Bernoulli equation

$$P_s \equiv \frac{P_s - P_\infty}{\frac{1}{2}\rho U_\infty^2}$$

$$= -\frac{2}{U_\infty}\left(\frac{1}{U_\infty}\frac{\partial \varphi_s}{\partial t} + \frac{\partial \varphi_s}{\partial x} \right)$$

$$= -2\left\{ \frac{1}{U_\infty}\left[-\frac{1}{4\pi}\frac{\partial}{\partial t}\iint_{S_c} \frac{g(\xi,\zeta,t)\,d\xi\,d\zeta}{[(x-\xi)^2 + y^2 + (\zeta-\zeta)^2]^{1/2}} \right] \right.$$

$$\left. + \left[-\frac{1}{4\pi}\frac{\partial}{\partial x}\iint_{S_c} \frac{g(\xi,\zeta,t)\,d\xi\,d\zeta}{[(x-\xi)^2 + y^2 + (\zeta-\zeta)^2]^{1/2}} \right] \right\}$$

$$= \frac{1}{2\pi}\iint_{S_c}\left\{ \frac{1}{U_\infty}\frac{\partial g(\xi,\zeta,t)}{\partial t}\frac{1}{[(x-\xi)^2 + y^2 + (\zeta-\zeta)^2]^{1/2}} \right.$$

$$\left. - \frac{(x-\xi)\,g(\xi,\zeta,t)}{[(x-\xi)^2 + y^2 + (\zeta-\zeta)^2]^{3/2}} \right\}\,d\xi\,d\zeta. \qquad (B\text{-}32)$$

Instead of solving the velocity potential directly, we may distribute the vortices over the foil S_a, and the wake, S_w, to form the integral equation. The vertical velocities induced by a vortex sheet are determined by using the Biot-Savart law, (Bisplinghoff, et al (1957))

$$v(x,y,z,t) = \frac{1}{4\pi} \iint\limits_{S_a} \frac{\gamma_a(\xi,s,t)[x-\xi] + \delta_a(\xi,s,t)[z-s]}{[(x-\xi)^2 + y^2 + (z-s)^2]^{3/2}} \, d\xi \, ds$$

$$+ \frac{1}{4\pi} \iint\limits_{S_w} \frac{\gamma_w(\xi,s,t)[x-\xi] + \delta_w(\xi,s,t)[z-s]}{[(x-\xi)^2 + y^2 + (z-s)^2]^{3/2}} \, d\xi \, ds,$$

$$(B-33)$$

where γ and δ are bound vortex strength and trailing vortex strength, respectively. The Kirchhoff's law and Kelvin's theorem must be satisfied for the vortex distribution. The pressure due to the vortex distribution is

$$P_v \equiv \frac{P_v - P_\infty}{\frac{1}{2}\rho U_\infty^2} = -\frac{2}{U_\infty}\left(\frac{1}{U_\infty}\frac{\partial \varphi_v}{\partial t} + \frac{\partial \varphi_v}{\partial x}\right), \qquad (B-34)$$

where $\partial \varphi_v / \partial x$ is the x - component velocity induced by the vortex distribution

$$\frac{\partial \varphi_v(x,+0,z,t)}{\partial x} = \frac{1}{4\pi} \lim_{y \to 0} y \iint \frac{\gamma_a(\xi,s,t)}{[(x-\xi)^2 + y^2 + (z-s)^2]^{3/2}} \, d\xi \, ds$$

$$= -\frac{1}{2} \gamma_a(x,z,t) \qquad (B-35)$$

The term, $\partial\varphi_v/\partial t$, can be derived from the definition of
the velocity potential

$$\varphi_v(x,0,\gamma,t) = \int_{-\infty}^{x} u(\xi,0,\gamma,t)\, \frac{\xi}{b}(t)\, d\xi$$

$$= -\frac{1}{2}\int_{-\infty}^{x} \gamma_a(\xi,\gamma,t)\, \frac{\xi}{b}(t)\, d\xi, \qquad (B\text{-}36)$$

then

$$\frac{\partial\varphi_v}{\partial t} = -\frac{1}{2}\frac{\partial}{\partial t}\int_{-\infty}^{x} \gamma_a(\xi,\gamma,t)\, d\xi. \qquad (B\text{-}37)$$

Sugstituting Eqs. (B-35) and B-37) into Eq. (B-34)

$$P_v(x,0,\gamma,t) = \gamma_a(x,\gamma,t) + \frac{1}{U_\infty}\frac{\partial}{\partial t}\int_{-\infty}^{x} \gamma_a(\xi,\gamma,t)\, d\xi. \qquad (B\text{-}38)$$

A linear superposition has been used to satisfy the
boundary conditions. By combining Eqs. (B-31) and (B-33),
we get the normal velocity on the foil

$$\upsilon(x,-0,\gamma,t) = -\frac{1}{2}\, g(x,\gamma,t)$$

$$+\frac{1}{4\pi}\iint\limits_{S_a} \frac{\gamma_a(\xi,\varsigma,t)[x-\xi] + \delta_a(\xi,\varsigma,t)[\gamma-\varsigma]}{\left[(x-\xi)^2 + y^2 + (\gamma-\varsigma)^2\right]^{3/2}}\, d\xi\, d\varsigma$$

$$+\frac{1}{4\pi}\iint\limits_{S_w} \frac{\gamma_w(\xi,\varsigma,t)[x-\xi] + \delta_w(\xi,\varsigma,t)[\gamma-\varsigma]}{\left[(x-\xi)^2 + y^2 + (\gamma-\varsigma)^2\right]^{3/2}}\, d\xi\, d\varsigma.$$

$$(B\text{-}39)$$

This is equivalent to Eq. (B-28). The same expression will be obtained if we apply the Kirchhoff's law and Kelvin's Theorem over the surface and evaluate the integration. The constant cavity pressure condition, Eq (B-18), is the result of uniting Eqs. (B-32) and (B-38), which is the same as Eq. (B-19)

$$
0 = -\gamma_a(x, \mathcal{z}, t) - \frac{1}{U_\infty} \frac{\partial}{\partial t} \int_{-\infty}^{x} \gamma_a(\xi, \mathcal{z}, t) d\xi
$$
$$
+ \frac{1}{2\pi} \iint_{S_c} \left[-\frac{1}{U_\infty} \frac{\partial \phi(\xi, \varsigma, t)}{\partial t} \frac{1}{[(x-\xi)^2 + y^2 + (\mathcal{z}-\varsigma)^2]^{1/2}} \right.
$$
$$
\left. + \frac{(x-\xi) \, \phi(\xi, \varsigma, t)}{[(x-\xi)^2 + y^2 + (\mathcal{z}-\varsigma)^2]^{3/2}} \right] d\xi d\varsigma. \qquad (B-19)
$$

Note that the cavity region, S_c , is also time dependent.

APPENDIX C

VELOCITY INDUCED BY A DISCRETE VORTEX SEGMENT

Consider the vortex segment $(x_1, \delta_1) - (x_2, \delta_2)$ with strength γ per unit length. Defining (ξ, ς) as the coordinates of a general point on the vortex, and (x, δ) as the coordinates of a control point. The law of Biot-Savart is applied to obtain the induced velocity at point

$$\frac{4\pi \, \upsilon(x, \delta)}{\gamma_a} = \int_{(x_1, \delta_1)}^{(x_2, \delta_2)} \frac{(x-\xi)\,d\varsigma - (\delta-\varsigma)\,d\xi}{\left[(x-\xi)^2 + (\delta-\varsigma)^2\right]^{3/2}} . \tag{C-1}$$

Along the vortex, we have

$$t \equiv \frac{d\xi}{d\varsigma} = \frac{x_2 - x_1}{\delta_2 - \delta_1} = Constant,$$

and the geometrical relationships

$$a \equiv 1 + t^2 ,$$
$$d \equiv e - t\delta ,$$
$$e \equiv x - x_1 + t\delta_1 ,$$
$$(x-\xi)\,d\varsigma - (\delta-\varsigma)\,d\xi = (x-x_1+t\delta_1-t\varsigma)\,d\varsigma - (\delta-\varsigma)\,t\,d\varsigma$$
$$= (e - t\delta)\,d\varsigma$$
$$= d \cdot d\varsigma ,$$
$$\left[(x-\xi)^2+(\delta-\varsigma)^2\right]^{1/2} = |d|/a^{1/2} \; sec\phi ,$$

$$d\varsigma = |d|/a \; sec^2\phi \, d\phi . \tag{C-2}$$

Then the equation (C-1) becomes

$$\frac{4\pi V(x,\zeta)}{\gamma_a} = d \cdot \int_{\zeta_1}^{\zeta_2} \frac{dS}{\left[(x-\zeta)^2 + (\zeta-S)^2\right]^{3/2}}$$

$$= \frac{a^{1/2}}{d}(\cos\beta + \cos\alpha), \qquad (C-3)$$

where α and β are the angles shown in Fig. (C.1)

Equation (C-3) is not suitable for numerical computation if d becomes small (Kerwin & Oppenheim (1974)). There are three special cases which require numerical approximations for small d,

(1) for $\zeta_1 \leqslant \zeta \leqslant \zeta_2$

$$\alpha \simeq \left|\frac{2d}{2a\zeta_1+b}\right|, \qquad \beta \simeq \left|\frac{2d}{2a\zeta_2+b}\right|,$$

$$\cos\alpha \simeq 1 - \frac{\alpha^2}{2} = 1 - \frac{2d^2}{(2a\zeta_1+b)^2},$$

$$\cos\beta \simeq 1 - \frac{\beta^2}{2} = 1 - \frac{2d^2}{(2a\zeta_2+b)^2},$$

$$\frac{4\pi V}{\gamma_a} = 2a^{1/2}\left[\frac{1}{d} - \frac{d}{(2a\zeta_1+b)^2} - \frac{d}{(2a\zeta_2+b)^2}\right]. \qquad (C-4)$$

(2) for $\zeta < \zeta_1$

$$\beta \simeq \left|\frac{2d}{2a\zeta_2+b}\right|, \qquad \theta = \pi - \alpha \simeq \left|\frac{2d}{2a\zeta_1+b}\right|,$$

$$\cos\beta \simeq 1 - \frac{2d^2}{(2a\zeta_2+b)^2},$$

$$\cos\alpha = -\cos\theta \simeq -1 + \frac{2d^2}{(2a\gamma_1+b)^2} \ ,$$

$$\frac{4\pi\upsilon}{\gamma_a} = 2a^{1/2}\left[\frac{d}{(2a\gamma_1+b)^2} - \frac{d}{(2a\gamma_2+b)^2}\right], \qquad (C-5)$$

(3) for $\gamma > \gamma_2$

$$\alpha \simeq |2d/(2a\gamma_1+b)|, \quad \theta \equiv \pi-\beta = |2d/(2a\gamma_2+b)|,$$

$$\cos\alpha \simeq 1 - 2d^2/(2a\gamma_1+b)^2,$$

$$\cos\beta = -\cos\theta = -1 + 2d^2/(2a\gamma_2+b)^2,$$

$$\frac{4\pi\upsilon}{\gamma_a} = 2a^{1/2}\left[\frac{d}{(2a\gamma_2+b)^2} - \frac{d}{(2a\gamma_1+b)^2}\right]. \qquad (C-6)$$

The induced velocity to the trailing vortex $(x_1, 0, \gamma_1) -$
$- (x_3, 0, \gamma_3)$ with strength δ_a is

$$\frac{4\pi\upsilon}{\delta_a} = -\int_{(x_1,\gamma_1)}^{(x_3,\gamma_3)} \frac{(\gamma-\zeta)d\zeta}{\left[(x-\zeta)^2+(\gamma-\zeta)^2\right]^{3/2}}$$

$$= \frac{x-\zeta}{\gamma-\gamma_1} \left. \frac{1}{\left[(x-\zeta)^2+(\gamma-\gamma_1)^2\right]^{1/2}} \right|_{\zeta=x_1}^{\zeta=x_3}$$

The total velocity induced by a vortex distribution
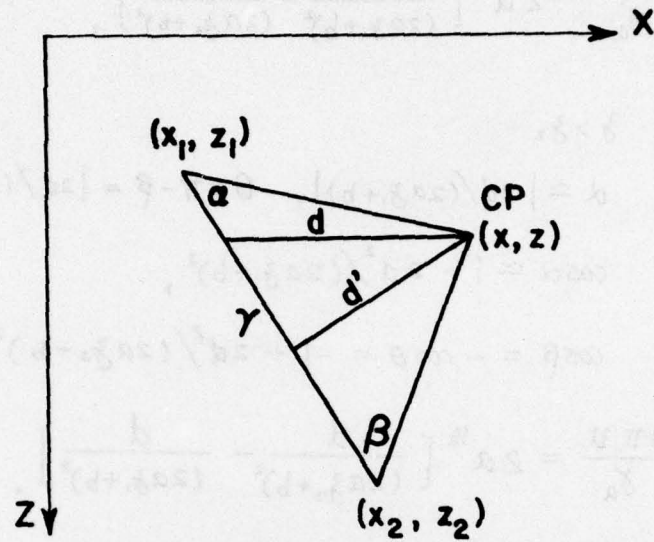is the sum of all the spanwise and chordwise vortices.

FIGURE C.1 Coordinate Systems for Discrete
Vortex Segment and Control Point

APPENDIX D

PRESSURE INDUCED BY A DISCRETE SOURCE SEGMENT

For unsteady supercavity flow, the pressure induced by source component consists of two terms: the space derivative $\partial \varphi_s / \partial x$ and time derivative $\partial \varphi_s / \partial t$. Rewrite the Bernoulli equation

$$P_s \equiv \frac{P_s - P_\infty}{\frac{1}{2}\rho U_\infty^2} = -\frac{2}{U_\infty}\left(\frac{\partial \varphi_s}{\partial x} + \frac{1}{U_\infty}\frac{\partial \varphi_s}{\partial t} \right).$$

The velocity in the x-direction at (x,ζ) due to the line source, $\varphi(t)$, along $(x_1, \zeta_1) - (x_2, \zeta_2)$ is (Fig. D.1)

$$\frac{4\pi U_s}{\varphi} = \partial \varphi_s / \partial x$$

$$= \int_{(x_1,\zeta_1)}^{(x_2,\zeta_2)} \frac{(x-\xi)\,d\lambda}{\left[(x-\xi)^2 + (\zeta-\varsigma)^2\right]^{3/2}}$$

$$= a^{1/2} \int_{\zeta_1}^{\zeta_2} \frac{e-t\varsigma}{(a\varsigma^2 + b\varsigma + c)^{3/2}}\,d\varsigma$$

$$= \frac{a^{1/2}}{2d^2(a\varsigma^2+b\varsigma+c)^{1/2}}\left(2ae\varsigma + be + 2tc + bt\varsigma\right)\Big|_{\zeta_1}^{\zeta_2}$$

$$= \frac{a^{1/2}}{d}\frac{\varsigma-\varsigma}{(a\varsigma^2+b\varsigma+c)^{1/2}}\Big|_{\zeta_1}^{\zeta_2}, \qquad (D-1)$$

where

$$e = x - x_1 + t\zeta_1,$$

$$c = e^2 + \zeta^2, \qquad (D-2)$$

and a, b, d are defined the same as Eq. (C-2)

Again, there are three special cases which require numerical approximation for small d. Equation (D-1) can be represented by the geometric angles (Fig. D.2)

$$\frac{4\pi U_s}{g} = \frac{a^{1/2}}{d}\left[\cos\psi(\cos\beta+\cos\alpha)\pm\sin\psi(\sin\beta-\sin\alpha)\right] \quad (D-3)$$

$$+ \text{ for } d > 0.$$
$$- \text{ for } d < 0.$$

Then for small d,

(1) for $z_1 < z < z_2$

$$\alpha \simeq \left|\frac{2d}{2az_1+b}\right|, \qquad \beta \simeq \left|\frac{2d}{2az_2+b}\right|,$$

$$\cos\alpha \simeq 1 - \alpha^2/2 = 1 - 2d^2/(2az_1+b)^2,$$

$$\sin\alpha \simeq \alpha \simeq 1 - 2d^2/(2az_2+b)^2,$$

$$\sin\beta \simeq \beta \simeq \left|\frac{2d}{2az_2+b}\right|,$$

$$\frac{4\pi U_s}{g} \simeq 2\left(\frac{1}{d} - \frac{d}{(2az_1+b)^2} - \frac{d}{(2az_2+b)^2}\right)$$

$$+ 2t\left(\left|\frac{1}{2az_2+b}\right| - \left|\frac{1}{2az_1+b}\right|\right). \quad (D-4)$$

(2) for $z < z_1$

$$\beta \simeq \left|\frac{2d}{2az_2+b}\right|, \qquad \theta = \pi-\alpha \simeq \left|\frac{2d}{2az_1+b}\right|,$$

$$\cos\beta \simeq 1 - 2d^2/(2az_2+b)^2,$$

$$\cos\alpha \simeq -\cos\theta = -1 + 2d^2/(2az_1+b)^2,$$

$$\sin\alpha \simeq |2d/(2az_1+b)|, \quad \sin\beta \simeq |2d/(2az_2+b)|,$$

$$\frac{4\pi U_s}{g} \simeq 2d\left(1/(2az_1+b)^2 - 1/(2az_2+b)^2\right)$$

$$+ 2t\left(\left|1/(2az_2+b)\right| - \left|1/(2az_1+b)\right|\right). \quad (D-5)$$

(3) for $\tilde{g} > \tilde{g}_2$

$$\alpha \simeq |2d/(2a\tilde{g}_1+b)| , \quad \theta \equiv \pi - \beta \simeq |2d/(2a\tilde{g}_2+b)|,$$

$$\cos\alpha \simeq 1 - 2d^2/(2a\tilde{g}_1+b)^2 , \quad \sin\alpha \simeq |2d/(2a\tilde{g}_1+b)|,$$

$$\cos\beta = -\cos\theta \simeq -1 + 2d^2/(2a\tilde{g}_2+b)^2 ,$$

$$\sin\beta \simeq |2d/(2a\tilde{g}_2+b)|,$$

$$\frac{4\pi u_s}{\tilde{g}} = 2d\left(\frac{1}{(2a\tilde{g}_2+b)^2} - \frac{1}{(2a\tilde{g}_1+b)^2}\right)$$

$$+ 2t\left(\left|\frac{1}{(2a\tilde{g}_2+b)}\right| - \left|\frac{1}{(2a\tilde{g}_1+b)}\right|\right). \qquad (D-6)$$

The induced pressure due to time variation of the source segment, $\tilde{g}_t$, is

$$\frac{4\pi}{\tilde{g}_t}\frac{\partial \varphi_s}{\partial t} = -\int_{(x_1,\tilde{g}_1)}^{(x_2,\tilde{g}_2)} \frac{d\lambda}{\left[(x-\xi)^2 + (\tilde{g}-\zeta)^2\right]^{1/2}} . \qquad (D-7)$$

By using the definition of Eq. (C-2), we obtain

$$\frac{4\pi}{\tilde{g}_t}\frac{\partial \varphi_s}{\partial t} = -\int_{\phi_1}^{\phi_2} \sec\phi \, d\phi$$

$$= -\log \frac{\tan\left(\frac{\pi}{4} + \phi_2\right)}{\tan\left(\frac{\pi}{4} + \phi_1\right)} . \qquad (D-8)$$

Once more, three special formulas are considered for small d,

(1) for $\mathfrak{z}_1 \leq \mathfrak{z} \leq \mathfrak{z}_2$

$$\phi_1 = -\left(\frac{\pi}{2} - \alpha\right), \quad \phi_2 = \frac{\pi}{2} - \beta,$$

$$\frac{\alpha}{2} \simeq \left| \frac{d}{2a\mathfrak{z}_1 + b} \right|, \quad \frac{\beta}{2} \simeq \left| \frac{d}{2a\mathfrak{z}_2 + b} \right|,$$

$$\frac{4\pi}{q_t} \frac{\partial \varphi_s}{\partial t} = -\log\left(\cot \frac{\beta}{2} \cot \frac{\alpha}{2}\right)$$

$$\simeq -\log \left| \frac{(2a\mathfrak{z}_1 + b)(2a\mathfrak{z}_2 + b)}{d^2} \right|. \tag{D-9}$$

(2) for $\mathfrak{z} < \mathfrak{z}_1$

$$\phi_1 = \frac{\pi}{2} - (\pi - \alpha) = \frac{\pi}{2} - \theta,$$

$$\phi_2 = \frac{\pi}{2} - \beta,$$

$$\frac{4\pi}{q_t} \frac{\partial \varphi_s}{\partial t} = -\log\left(\cot \frac{\beta}{2} \tan \frac{\theta}{2}\right)$$

$$= -\log \left| \frac{2a\mathfrak{z}_2 + b}{2a\mathfrak{z}_1 + b} \right|. \tag{D-10}$$

(3) for $\zeta > \zeta_2$

$$\phi_1 = -\left(\frac{\pi}{2} - \alpha\right),$$

$$\phi_2 = -\left(\frac{\pi}{2} - (\pi - \beta)\right) \equiv -\left(\frac{\pi}{2} - \theta\right),$$

$$\frac{4\pi}{\zeta_t} \frac{\partial \psi_3}{\partial t} = -\log \left(\cot \frac{\alpha}{2} \tan \frac{\theta}{2}\right)$$

$$= -\log \left| \frac{2a\zeta_1 + b}{2a\zeta_2 + b} \right|. \qquad (D-11)$$

Then the induced pressure due to source distribution can be calculated by using these equations and Bernoulli's equation.
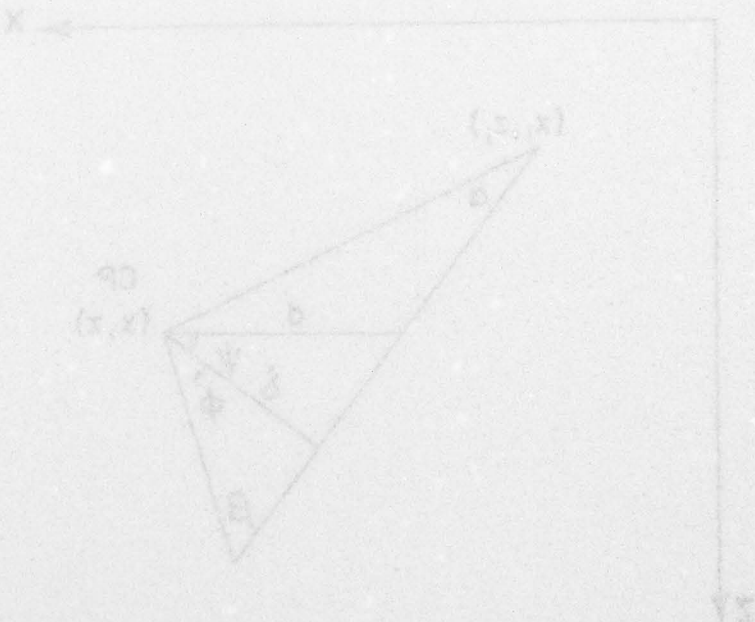
FIGURE D.1   Discrete   Source   Segment

FIGURE   D.2   Coordinate   Systems   for   Discrete   Source
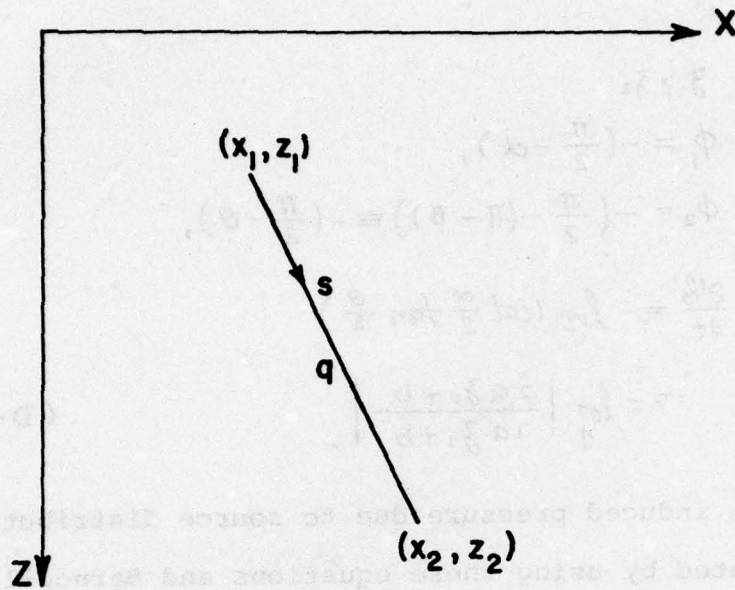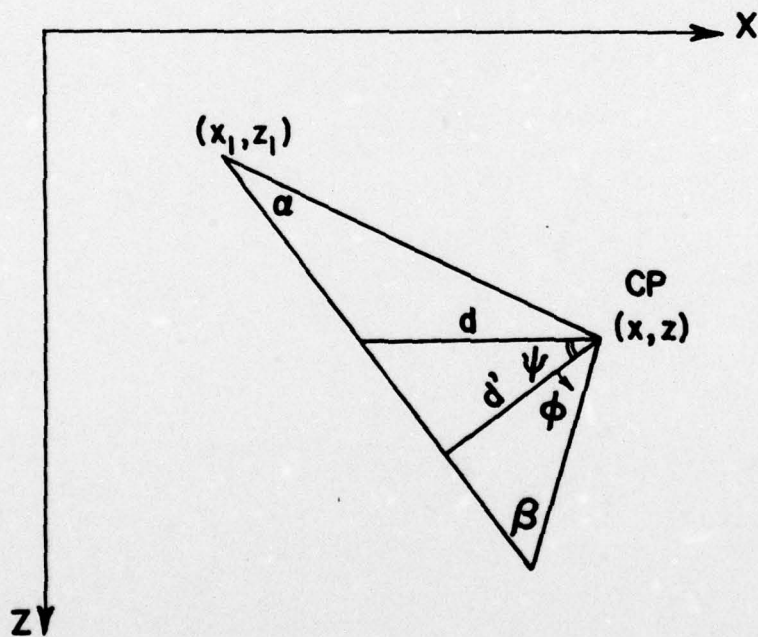Segment   and   Control   Point

APPENDIX E

NUMERICAL RESULTS OF RECTANGULAR HYDROFOIL

The present numerical method was used to calculate the unsteady forces on an aspect ratio 6, rectangular hydrofoil. A comparison was made on heaving motion at $\sigma/\alpha = 2.0$ and $\omega C_0/U_\infty = 3.1416$. Eight elements were used along the chord of the foil, six elements were used in the cavity behind the foil and two elements were used along the semispan in the calculation. The lift amplitude and phase angle were calculated after one cycle of oscillation and were found to be 2.71 and 108.6°, respectively. The lift amplitude and phase angle of Widnall's results at $\omega C_0/U_\infty = 3.1416$ are 3.4 and 115°.

REFERENCES OF APPENDICES

Ashley, H. & Landahl, M. 1965 Aerodynamics of wings and bodies, Addison-Wesley.

Bisplinghoff, R. L., Ashley, H. & Halfman, R. L. 1957 Aero-elastiicity. Addison Wesley.

Den Hartog, J. P. 1956 Mechanical vibration. McGraw-Hill.

Kerwin, J. E. & Oppenheim, B. W. 1974 A lifting-surface program for trapezoidal control surfaces with flaps. Rep. No. 74-15, MIT

Newman, J. N. 1977 Marine hydrodynamics. MIT Press.